Ultrafast 4*f* multiplet excitation in rare-earth metals studied with X-rays

Dissertation
zur Erlangung des Grades eines
Doktors der Naturwissenschaften

am Fachbereich Physik
der Freien Universität Berlin

vorgelegt von
Tim Amrhein

Berlin 2025

Erstgutachter: Prof. Dr. Martin Weinelt
Zweitgutachter: Prof. Dr. Wolfgang Kuch
Tag der Disputation: 06.08.2025

Abstract

Optically driven fundamental processes initiating ultrafast magnetization dynamics in 4*f* rare-earth metals have been studied for many years. Attempts were made to explain the various demagnetization timescales observed for different 4*f* metals, considering *e.g.* magnon generation [1, 2] or electron-phonon driven spin-flip scattering [3, 4]. Excitations within the 4*f* electronic system, though, were not involved in the discussion, since they are not directly accessible by optical stimuli.

This thesis reports on time-resolved experiments performed at the free-electron laser facilities EuXFEL and FLASH which identified an up to now disregarded mechanism provoking 4*f* electronic excitations on ultrafast timescales indirectly via interaction with the laser-excited 5*d*6*s* valence electrons in 4*f* metals.

By analyzing ultrafast spectral changes in X-ray absorption (XAS) and resonant inelastic X-ray scattering (RIXS) signals from terbium metal with the help of atomistic simulations, inelastic 5*d*-4*f* electron-electron scattering is found to transfer energy and angular momentum between the 4*f* and 5*d* systems. As a consequence, 4*f* electrons are excited from the ground state $^7F_6$ into energetically higher ^7F_J multiplets.

Based on these findings, a three-temperature model has been developed, separating temperatures for the 4*f* electrons, the 5*d* valence electrons and the lattice. By fitting the simulation based on the three-temperature model to the experimental data, the coupling between 4*f* and 5*d* electrons is found to increase with the amount of valence electrons, able to distribute enough energy to lift the 4*f* electronic system to the energetically lowest excited 4*f* multiplet $^7F_5$.

According to the 3rd rule of Thole and van der Laan [5], the absorption branching ratio of M_5 to M_4 decreases with the reduction of the total angular momentum J, as expected for transitions into energetically higher multiplets $^7F_{J=5,4,..0}$ of the 4*f* electronic system. With time-resolved XAS experiments at the FemtoSlicing facility BESSY II, it was demonstrated, that this correlation can be used to probe and evaluate 4*f* multiplet excitations, even with sources exhibiting limited energy resolution.

The reported 5*d*-4*f* scattering mechanism transiently alters the magnetocrystalline anisotropy and hence the coupling of the 4*f* system to the lattice. With up to 22 % of all probed atoms being excited to energetically higher multiplets, inelastic 5*d*-4*f* scattering is deemed to have a significant impact on the ultrafast demagnetization in terbium metal and must be taken into account for a full description of the magnetization dynamics in rare-earth metals.

Zusammenfassung

Seit einigen Jahren werden optisch getriebene, physikalische Prozesse studiert, die ultraschneller Änderungen der Magnetisierung in 4*f* seltenen Erden bewirken. Die unterschiedlichen Entmagnetisierungszeitskalen in verschiedenen 4*f* Metallen wurden *z.B.* durch Magnonen-Erzeugung [1, 2] oder Elektronen-Phononen getriebene Spin-Flip Streuung [3, 4] erklärt. Anregungen innerhalb des 4*f* Elektronensystems wurden jedoch nicht diskutiert, da diese rein optisch nicht direkt induziert werden können.

Diese Dissertation berichtet von zeitaufgelösten Experimenten, die an den Freie Elektronen Laser Einrichtungen EuXFEL und FLASH ausgeführt wurden und einen bislang vernachlässigten Mechanismus in 4*f* Metallen identifizieren, welcher Anregungen der 4*f* Elektronen durch Wechselwirkung mit laserstimulierten 5*d*6*s* Valenzelektronen hervorruft.

Durch die Analyse von ultraschnellen spektralen Änderungen im Signal der Röntgenabsorption (XAS) und der resonanten inelastischen Röntgenstreuung (RIXS) sowie deren Simulationen durch atomistische Rechnungen, wurde für metallisches Terbium belegt, dass inelastische 5*d*-4*f* Elektron-Elektron Streuung Energie und Drehimpuls zwischen dem 4*f*- und dem 5*d*-System austauschen kann. Als Konsequenz werden 4*f*-Elektronen aus dem Grundzustand $^7F_6$ in energetisch höhere ^7F_J Multipletts angeregt.

Aufbauend auf diesen Ergebnissen wurde ein Drei-Temperaturen-Modell erstellt, mit separierten Temperaturen für die 4*f*-Elektronen, die 5*d* Valenzelektronen und das Gitter. Durch Anpassung der Simulation basierend auf dem Drei-Temperatur-Modell an die experimentellen Daten, wurde gezeigt, dass die Wechselwirkung zwischen 4*f*- und 5*d*-Elektronen sich mit der Anzahl an 5*d*-Valenzelektronen verstärkt, welche über ausreichend Energie verfügen, um das 4*f*-Elektronensystem in das energetisch niedrigste, angeregte 4*f*-Multiplett $^7F_5$ anzuheben.

Die 3. Regel von Thole und van der Laan [5] besagt, dass das Absorptions-Verzweigungsverhältnis zwischen M_5 und M_4 mit verringertem Gesamtdrehimpuls J abnimmt. Solch eine Reduktion des Gesamtdrehimpulses ist auch bei einer Anregung von energetisch höheren 4*f*-Multipletts zu erwarten. Mit einem zeitaufgelösten XAS Experiment an der FemtoSlicing Einrichtung am BESSY II wurde gezeigt, dass dieser Zusammenhang dazu genutzt werden kann, die Anregung von 4*f*-Multipletts auch an Quellen mit limitierter Energieauflösung zu messen und auszuwerten.

Der beschriebene 5*d*-4*f* Streuprozess verändert vorübergehend die magnetische Anisotropie und beeinflusst deshalb die Wechselwirkung zwischen 4*f*-Elektronen und dem Gitter. Da in den beschriebenen Experimenten bis zu 22 % aller untersuchten Atome in energetisch höhere Multipletts angeregt wurden, wird geschlussfolgert, dass inelastische 5*d*-4*f* Streuung einen wesentlichen Einfluss auf die ultraschnelle Entmagnetisierung in metallischem Terbium hat und deshalb bei einer vollständigen Beschreibung der Magnetisierungsdynamik in Metallen der seltenen Erden berücksichtigt werden muss.

Contents

Chapter 1

Introduction

In this rapidly evolving world, the need for digital data storage and transfer has become essential and the demand for faster and more energy efficient storage devices is ever increasing. Especially processes effectuating magnetic all-optical switching (AOS) [6] promise fast and energy efficient manipulation of magnetization and are hence pushed towards application for information storage and writing. Prototype AOS materials comprise $3d$ transition metals and $4f$ rare-earth metals, making use of their different magnetic response to optical excitation, which results in a reorientation of the net magnetization. The different magnetic behavior stems from the distinct electronic structures, constituted when the $3d$ or $4f$ shell is being filled [7].

In the case of $4f$ rare-earth metals the magnetic moment is mainly carried by the localized $4f$ electrons and only a small contribution arises from the delocalized valence $5d6s$ states [8]. It is the localized character of the $4f$ electrons, which governs formation of both spin and orbital angular momenta. Orbital degrees of freedom, contributing to the $4f$ magnetic moments, allow for coupling to the crystal lattice and give rise to magnetocrystalline anisotropy [9, 10], a crucial property for magnetic devices to form stable magnetic domains. As the $4f$ electronic structure determines spin and orbital wavefunctions and defines magnetic coupling, the element specific electronic state is decisive for the observed magnetic order dynamics in $4f$ metals. Thus, it is of crucial importance to explore excitation mechanisms, that affect the $4f$ electronic state, in order to understand magnetization dynamics in rare-earth metals.

As electronic excitations in the $4f$ shell can not be provoked directly by optical means, such alterations of the $4f$ electronic structure were neglected in previous discussions on the ultrafast magnetization dynamics in rare-earth metals [1, 2, 3, 4, 11, 12, 13, 14, 15, 16, 17, 18]. This thesis proves that $4f$ electronic excitations can be induced indirectly on ultrafast timescales by inelastic 5d-4f electron-electron scattering, transferring energy and angular momentum between the laser-excited valence system and the 4f electrons.

Therefore, time-resolved experiments exploiting different X-ray based techniques were performed at the SCS instrument [19] of the free-electron laser facility EuXFEL, the TRIXS endstation [20] at the PG1 beamline at FLASH as well as at the FemtoSlicing facility [21, 22, 23, 24] at the synchrotron BESSY II. On basis of atomistic calculations and simulations of the experimental results, distinct 4f multiplet transitions and responsible excitation mechanisms were identified. For further evaluation, a three-temperature model is formulated to describe the temperature evolution of the 4f and valence electrons as well as the lattice.

The thesis starts with a brief introduction into the field of ultrafast magnetization dynamics, the creation of ultrashort X-ray pulses and atomistic calculations. Chapter 3 introduces the applied experimental techniques (X-ray Absorption Spectroscopy (XAS) [25, 26, 27] and Resonant Inelastic X-ray Scattering (RIXS) [28, 29, 30]), the experimental setups at the different visited facilities as well as the studied samples. The experimental results are presented and discussed in Chapter 4, involving four sections, focusing on the XAS experiment at EuXFEL (4.1), the RIXS experiment performed at FLASH (4.2), the development of a three-temperature model, taking into account a specific temperature of the 4f electronic system and allowing for energetically higher 4f multiplet excitations (4.3) and finally Section 4.4, which addresses a novel experimental approach for detecting 4f excitations via transient changes in the absorption branching ratio. The findings of this thesis are summarized in Chapter 5 and an outlook for future investigations is given.

The reported pathway for redistribution of angular momentum between the 5d and 4f electronic systems must be taken into account for a full description of the demagnetization process in rare-earth metals. Upcoming experimental capabilities at BESSY II and FLASH will allow us to directly connect transient changes of the electronic and magnetic structure, further pioneering the understanding of ultrafast magnetization dynamics in 4f materials.

Chapter 2

Scientific background

The present chapter provides the scientific background and motivation for this thesis. It introduces the field of ultrafast magnetization dynamics with the focus on $4f$ rare-earth metals, describes the generation of ultrashort X-ray pulses and establishes atomistic calculations as the basis for the simulations performed in this work.

2.1 Magnetism

In physics, electric and magnetic phenomena are intrinsically connected and find their relation in Maxwells equations. By looping an electric charge, a magnetic dipole oriented orthogonal to the plane of rotation arises, quantified by the magnetic dipole moment or just magnetic moment, equal to the product of loop area and electric current.
The macroscopic magnetization of a ferromagnetic solid, however, cannot be explained in this classical picture of circulating electric currents, which would result in extremely large surface currents when creating the observed magnetic moments.
It was the foundation of quantum mechanics, which accomplished the knowledge about the intrinsic angular momentum of an electron and the understanding, that the magnetic moment of an atom stems from two contributions, the electron spin and its orbital angular momentum, both quantized in units of $\frac{\hbar}{2}$ and $\hbar$, respectively.
In solid samples, especially crystals, $\sim 10^{23}$ atoms/cm^3 are present in a periodic structure. All these atoms contribute to the magnetization of the sample. If all the magnetic moments cancel each other out, the overall magnetization is zero, such as in paramagnetic samples with a random orientation of the atomic magnetic moments. Otherwise the magnetic

moments tend to also form periodic structures, representing an energetically optimal configuration, which is dependent on the spin and orbital magnetic moment of each atom, the electronic and crystal structure as well as the sample temperature.

The simplest magnetic configuration is observed in ferromagnetic materials exhibiting spontaneous magnetization. Applying an external magnetic field to a ferromagnetic sample aligns all magnetic moments parallel along the outer field, leading to a saturated state. If the outer field is removed, the sample shows remanence, keeping a residual magnetization. The magnetic alignment can be broken by heating the sample, which will result in a paramagnetic state when the thermal fluctuations overcome the magnetic interaction at the material-dependent Curie temperature T_C.

The ability of a ferromagnetic material to form stable magnetic domains is given by spin-lattice interaction: spin-orbit-coupling together with an asymmetric orbital wavefunction orientates the orbital and spin moment along an energetically preferable lattice direction. The preference of a magnetization direction due to interaction with the crystal field is called magnetocrystalline anisotropy (MCA) [31].

The most relevant magnetic elements are $3d$ transition metals and $4f$ rare-earth metals, in which magnetism arises either from itinerant $3d$ bands or is formed by strongly localized $4f$ states. The control of magnetic order by optical means in both types of elements is subject of research in ultrafast magnetization dynamics.

2.2 The field of ultrafast magnetization dynamics

The field of ultrafast spin physics was established with the development of femtosecond lasers, which enabled the pioneering experiment by Beaurepaire *et al.* [32] in 1996, showing the magnetic remanence of a ferromagnetic nickel sample to be quenched within less than 1 ps. In a time-resolved experiment using pump and probe pulses of 60 fs length and 620 nm wavelength, they could follow the spin dynamics via the longitudinal Kerr signal and the electronic thermalization from optical transmitivity. Within a phenomenological three-temperature model involving spin, electron and lattice temperature they could derive coupling parameters for spin-electron, electron-lattice and spin-lattice interaction.

This experiment kick-started the rise of the field of ultrafast magnetization dynamics aiming to understand the femtosecond response of the spin system followed after optical excitation. Numerous experimental and theoretical studies were striving to identify microscopic mechanics involved [12, 33]. Conservation laws teach us, that a reduction of macroscopic magnetization must arise from transport of angular momentum out of the spin system, which forms the ordered magnetic moments. A prominent localized process redistributing angular momentum is Elliot-Yafet-like spin-flip scattering [17, 18, 34, 35, 36]. Angular momentum is transferred out of the spin system into the crystal lattice by scattering between electrons and phonons. Demagnetization can also involve more delocalized processes transferring angular momentum, such as generation of spin polarized currents [37, 38, 39, 40, 41, 42, 43] or magnons [1, 2, 44, 45, 46, 47].

These mechanism have been extensively investigated for elemental 3*d* metals like iron, cobalt and nickel, where delocalized 3*d* electrons contribute to the magnetic moment, resulting in quenched orbital magnetic moments L and a main contribution of spin magnetic moment S to magnetization in these type of materials. However, more complex magnetic materials can also involve a significant orbital magnetic momentum L. The influence of orbital degrees of freedom on ultrafast magnetization dynamics as well as on the conservation of the orbital magnetic moment is not well understood yet and subject of many recent research projects [48, 49, 50].

This thesis adds a novel perspective to this ongoing discussion by investigating the spin-orbit dynamics in the rare-earth metal terbium.

2.3 Rare-earth 4*f* metals

The rare-earth 4*f* elements involve the lanthanides, ranging from lanthanum with an atomic number of 57 to lutetium with an atomic number of 71. Additionally, yttrium and scandium are often categorized as rare earths. The lanthanides are of special interest, because the lowest shell with *f* character is increasingly filled, resulting in intriguing characteristics that are not found for the lighter 3*d* elements.

This chapter will elucidate the electronic structure of rare-earth 4*f* metals, resulting magnetization dynamics in the 4*f* metals gadolinium and terbium and the role of electronic excitations in earlier time-resolved experiments.

2.3.1 Electronic structure of 4*f* metals

While forming metallic solids, the rare-earth elements tend to transfer a 4*f* electron to the 5*d* shell, building up a delocalized valence band of hybridized 5*d*6*s* electrons and leaving behind triple ionized atomic cores. Figure 2.1 a shows the radial densities for typical Bloch states in gadolinium [8]. The 4*f* states are quite close to the atomic cores, have no overlap with 4*f* states from neighboring atoms, and hence do not interact with other 4*f* electrons directly. On the other hand, the 5*d* and 6*s* states are overlapping with each other and involve much larger radii than the 4*f* shell. The overlap with 5*d*6*s* states from adjacent atomic sites leads to the formation of the hybridized 5*d*6*s* valence band. Despite carrying most of the magnetic moment, the 4*f* electrons only interact indirectly with each other via the spin-polarized valence electrons. The latter is called Ruderman-Kittel-Kasuya-Yosida (RKKY) interaction [7, 51, 52, 53, 54]. It results in a 4*f* magnetic coupling parameter, whose sign alters and whose amplitude is damped with atomic distance. This leads to strong magnetostriction in these materials and the formation of diverse magnetic ordering [55] such as ferromagnetic, helical antiferromagnetic, cone-like and longitudinal oscillating spin structures.

Besides magnetostriction effects, the coupling between spin magnetic moments and lattice can be substantiated by 4*f* orbital degrees of freedom. It is the localized 4*f* electronic structure, which governs the orbital momentum L. The contribution of S and L to the atomic magnetic moment is strongly element-specific and directly connected to the 4*f* Hund's rule ground state. This is demonstrated in Fig. 2.1 b, showing the L, S and J quantum numbers for the trivalent 4*f* ions and how drastically those numbers change for the different 4*f* metals. The corresponding ground state multiplet for these metals is in accordance with Hund's rules and of the form $^{2S+1}L_J$. For the ground state, $J = |L-S|$ for a less than half filled shell and $J = L+S$ for a more than half filled shell. Because in these materials L-S coupling is stronger than the interaction with the crystal field, the good quantum number characterizing these states is J.

All $^{2S+1}L_J$ states show a degeneracy of $2J+1$. This degeneracy is however lifted by the crystal field, resulting in split sublevels $m_J = -J,..,0,..,+J$. Below the Curie temperature the thermal occupation favors the energetically lower m_J levels and especially in 4*f* metals MCA can increase the m_J level splitting. In combination with inter-site alignment of magnetic moments mediated by the RKKY interaction this gives rise to a magnetic ordering.

To summarize, rare-earth metals have two coupled electronic systems that

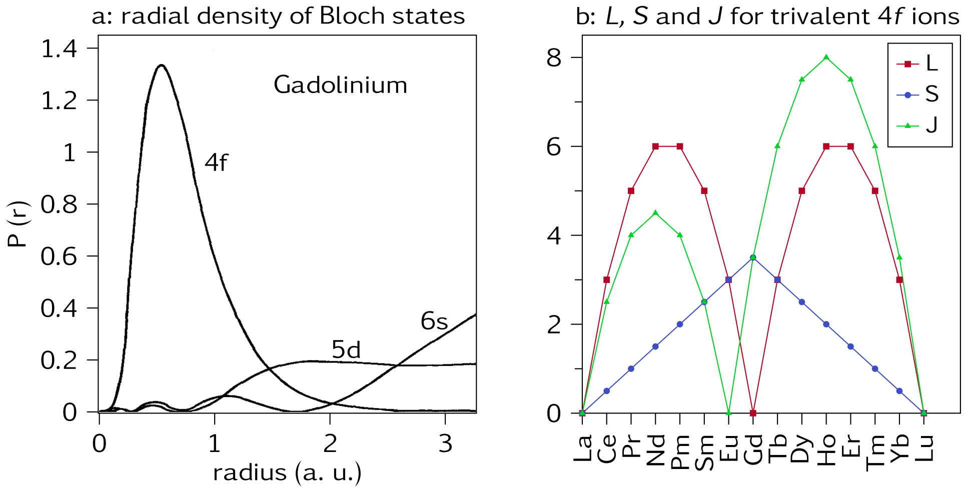

Figure 2.1: a: Radial density of Bloch states for the rare-earth metal gadolinium. The 4*f* states are localized close to the atomic core, while the 5*d* and 6*s* states are more delocalized. Graphic adapted from [8].
b: *L*, *S* and *J* for trivalent 4*f* ions in their Hund's rule ground state. Graphic adapted from [56].

contribute to magnetism. Most of the magnetic moment is carried by the localized 4*f* electrons with element specific contribution of S and L. The second system are the hybridized 5*d*6*s* electrons. Due to their itinerant character, their orbital angular momentum L is quenched and their spin magnetic moment S dominates resulting in only a small contribution to the overall magnetic moment per atom.

2.3.2 Magnetization dynamics in gadolinium and terbium

The rare-earth metals gadolinium (Gd) and terbium (Tb) very well demonstrate, how the 4*f* electronic structure and the resulting orbital angular momentum determines magnetic properties as well as ultrafast magnetization dynamics. Gadolinium metal has a half filled 4*f* shell, resulting in a ground state $^8S_{7/2}$ carrying an orbital angular momentum $L = 0$ and a spin angular momentum of $S = 7/2$. As the S-orbital is spherically symmetric, the coupling of the spin to the lattice involves a very small MCA ($\sim 0.03\,\mathrm{meV}$) [9]. In contrast, terbium with just one 4*f* electron more, has an orbital angular momentum of $L = 3$ and a spin $S = 3$ in the ground state

$^7F_6$. This configuration results in a very anisotropic orbital wavefunction and hence a strong coupling between the lattice and the orbital magnetic moment and accordingly to an extremely large MCA ($\sim 16.5\,\mathrm{meV}$) [10].
Frietsch *et al.* [2] used time- and angle-resolved photoelectron spectroscopy in the extreme ultraviolet regime to record state-dependent magnetization dynamics in gadolinium and terbium after near-infrared (800 nm) excitation. Pumping in this energy regime only excites the $5d6s$ valence electrons, the $4f$ states are not directly accessible. The magnetization of the valence electrons was quantified by the $5d6s$ exchange splitting, while in $4f$ photoemission the $4f$ ferromagnetic order was related to the magnetic linear dichroism arising for opposite magnetic field directions. They observed a stronger and faster reduction of the exchange splitting in the terbium valence system ($\tau_{Tb,5d} \approx 300\,\mathrm{fs}$) than for gadolinium ($\tau_{Gd,5d} \approx 700\,\mathrm{fs}$). While the $4f$ demagnetization in terbium essentially follows the $5d$ exchange splitting with a timescale of $\tau_{Tb,4f} \approx 400\,\mathrm{fs}$, in the case of gadolinium, $5d$ and $4f$ system exhibit strongly different dynamics. Here, the $4f$ magnetic order is reduced on a timescale of 14 ps, an order of magnitude slower than the $5d$ dynamics. They assign the different $4f$ magnetic response in gadolinium and terbium to the strongly diverging MCA in both metals.
Elliot-Yafet-like electron-phonon spin-flip scattering efficiently transfers energy and angular momentum from the directly excited $5d$ system to the lattice, leading to the femtosecond response in the exchange splitting. In gadolinium the small MCA results in a weak $4f$-spin-lattice coupling, *i.e.* the $4f$ magnetic system reacts on a rather slow timescale. In terbium, however, the large MCA and consequent strong $4f$-spin-lattice coupling appears to efficiently alter $4f$ magnetic order after heating the crystal lattice by $5d$-electron-phonon scattering. The excitation of phonons, however, directly generates magnons in terbium metal. As a consequence of intra-atomic exchange, they argue, the ultrafast $4f$ demagnetization in terbium to additionally affect the $5d$ spin system, leading to the more efficient quenching of $5d$ exchange splitting.
A mechanism which has so far not been considered are the excitations of the $4f$ electronic system triggered by direct $5d$-$4f$ interaction, the excitation channel explored in this thesis.

2.3.3 Electronic excitations in $4f$ metals

The contribution of orbital angular momentum L and spin S to the total angular momentum J in terbium and gadolinium are vastly different.

Attempts were made to separate the dynamics of S and L via XMCD measurements and sum rule application [57, 58, 59]. This works well for transition metals at the L-edges as *e.g.* demonstrated by Boeglin *et al.* for cobalt [60], but the few investigations concerning rare-earth metals [15, 16] are rather inconclusive, mostly due to large errors overshadowing the rather small effects seen.

As changes in L and S for the $4f$ system of rare-earth metals must be linked to electronic excitation within the $4f$ system, elevating the $4f$ electronic system out of the ground state into energetically higher multiplets, these studies were looking for this kind of excitation without explicitly stating it. Hence these studies can be taken as an indication, that electronic excitations including the $4f$ shell may be present.

A change in the electron distribution in the $4f$ shell leads to higher excited states with changed L, S or J. However, because J is the good quantum number, all states with the same J will hybridize, forming mixed states and altering their energy position. For a simplified notation in this thesis, all hybridized states will be referenced by their largest contribution. All possible states for a given amount of electrons n form the $4f^n$ multiplet.

In this thesis a novel approach allowing investigation of $4f$ electronic excitations in rare-earth metals is presented, which combines tr-XAS (3.1 and 4.1) and tr-RIXS (3.2 and 4.2) measurements with atomistic calculations. In order to perform such time-resolved measurements, sources for ultrashort X-ray pulses are needed. Only the recent development of free-electron lasers supplies X-ray pulses with the necessary energy and time resolution to probe electronic excitations in the $4f$ shell.

2.4 Sources for ultrashort X-ray pulses

The development of ultrashort optical pulses and experimental techniques using them for pump-probe experiments allowed for the investigation of the ultrafast demagnetization in nickel, as demonstrated by Beaurepaire *et. al.* [32]. These femtosecond pulses were essential, as for pump-probe experiments, time resolution is directly linked to the cross-correlation between pump and probe pulse and hence the pulse duration.

Today, ultrafast phenomena like all optical switching [6, 13, 14], in *e.g.* materials composite of $4f$ rare-earth and $3d$ transition metals, or initial electronic excitations as discussed to provoke inter-site spin transfer [61, 62] are of high interest to the community. For a detailed understanding of the microscopic mechanisms involved, a state and element specific probe is indispensable. A well suited method to study magnetic and electronic properties, selectively for specific electronic shells, is X-ray absorption spectroscopy (see Chapter 3.1). To resolve magnetic and electronic structure in the ultrafast regime, femtosecond X-ray pulses are needed.

For wavelengths in the optical regime pulsed laser systems are commercially available. The most common laser systems are based on Ti:Sa crystals as lasing material. They show a broad bandwidth reaching from 570 to 1070 nm with an intensity maximum around 800 nm and generate pulses in the range from tens of femtoseconds to few picoseconds. For these wavelengths suited transmission optics with very low losses are available, allowing to stretch, compress or filter the pulses in time, space and energy.

In contrast, in the X-ray regime, traditional optics like mirrors and lenses introduce much larger losses. Hence, mostly reflective optics, based on small angle reflection gratings, are used. However, this reduces the capability to shape or filter X-ray pulses, especially in time and energy. Therefore, sources are needed that produce inherently short and well defined pulses.

2.4.1 Synchrotrons and the slicing method

For long years synchrotrons were the most brilliant sources for X-ray pulses. Originally synchrotron radiation was discovered as an unwanted side effect in particle accelerators. If the path of an electron close to the speed of light is bent in a magnetic field, X-rays are emitted tangentially to their moving direction due to relativistic effects.

Synchrotron sources are particle accelerators that utilize this synchrotron radiation for X-ray based experiments. Undulators are employed to increase the brightness and reduce the bandwidth of the radiation. An undulator is an array of periodically spaced magnet pairs, leading to an oscillation of the electron beam perpendicular to its pointing direction (see Fig. 2.2 a). Due to those oscillations, X-ray radiation occurs alongside the electron beam. Radiation from each oscillation period can constructively interfere, resulting in a narrow X-ray beam with a well defined bandwidth and low dispersion.

Nowadays, undulator designs allowing for linearly and circularly polarized radiation as well as for a broad range of photon energies are available, enabling research in vast fields of different scientific disciplines world wide.

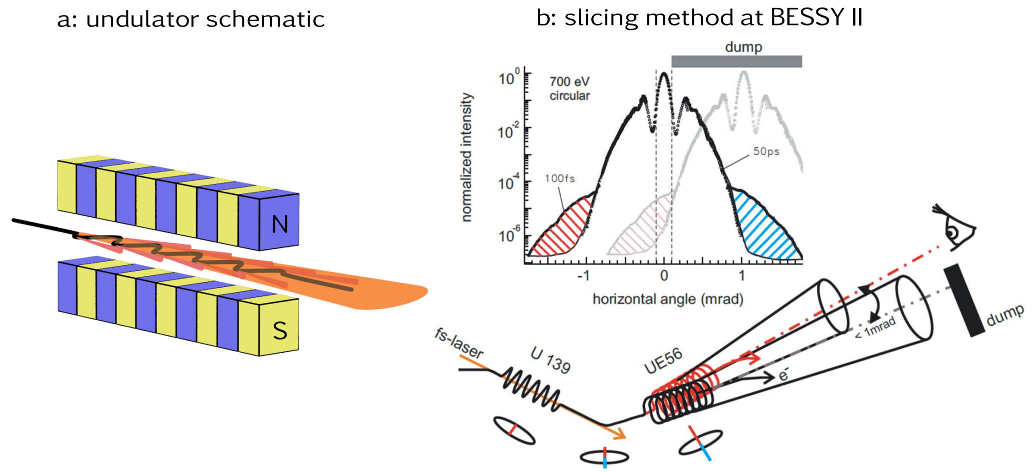

a: undulator schematic

b: slicing method at BESSY II

Figure 2.2: a: Electrons, passing through an undulator, oscillate in the magnetic field. Interference of radiation emitted from the same electron at different positions in the undulator leads to a narrow bandwidth and dispersion.
b: Implementation of the slicing method at the FemtoSlicing facility at BESSY II [22]. The lower panel shows the modulation and radiation process. By modulation of the electron bunches (oval) with femtosecond laser pulses, electrons are bunched together to slices. After spatial separation in a bending magnet, radiation of circular polarized X-rays occurs in the undulator 'UE56'. Due to the spatial separation, the modulated electrons radiate at a different angle. The angular distribution of the radiation is shown in the upper panel. The blue and red parts stem from the slice and have a much shorter temporal profile in the range of 100 fs.

However, as electrons travel in bunches in a synchrotron, X-ray pulses with a temporal width proportional to the spatial distribution of electrons in the bunch alongside the beam direction are created. Depending on the operation mode the resulting pulse duration is in the range of 5 – 100 ps. This is short enough for some experiments, however, to investigate ultrafast phenomena like demagnetization induced by an optical pulse in the femtosecond regime, even shorter pulses are needed.
In 1996 Zholents and Zolotorev proposed a method to produce even shorter pulses in the range of tens of femtoseconds [63]. Using optical laser pulses in the femtosecond regime, the electron bunches in an undulator can be modulated. If the optical pulse polarization is in the same plane as the electron oscillation while traveling alongside, the electric field induced by the optical photons can accelerate or decelerate parts of the electron bunch. Thus, some of the electrons become bunched together even more, creating a slice of electrons with a modulated energy. Passing

through a bending magnet after modulation induces a spatial displacement perpendicular to the beam direction for this slice in correspondence to the energy modulation. Passing through another undulator, the radiation from this slice will occur at a slightly different angle as for the rest of the electron bunch and hence can be spatially separated. Because such a slice has much shorter length than the entire electron bunch, also the emitted X-ray pulse from this slice is much shorter in time.
This method is called ′slicing′ and is employed at very few synchrotrons across the world. Figure 2.2 b shows a schematic, how the slicing method is applied at the FemtoSlicing facility at BESSY II [22]. In the lower panel the modulation and radiation process is depicted. The electron beam (black line) passes through the first undulator ′U 139′ and is modulated by femtosecond laser pulses. The oval below represents the electron bunch with parts of the electrons energetically modulated to form a slice (red line). By altering the electron path in the bending magnet behind the modulator ′U139′, the sliced electrons become spatially separated. In the oval the red line represents the decelerated and the blue line the accelerated electrons. Circular polarized X-ray pulses are radiated in the undulator ′UE56′. Due to the spatial separation of the sliced electrons from the rest of the bunch, these electrons radiate under a different emission angle of the order of 1 mrad. The upper panel shows the angular distribution of the radiation. The red and blue colored parts stem from the modulated electrons and have a much shorter temporal profile. By employing a local orbit bump in the electron beam path to change the pointing of the radiation, the experiment can be supplied with either 50 ps X-ray pulses or with much shorter 100 fs X-ray pulses, but at a lower brilliance.

2.4.2 X-ray free-electron laser (XFEL)

In recent years the first X-ray free-electron laser (XFEL) facilities were established as the newest generation of X-ray radiation sources. They supply ultrashort (<100 fs) X-ray pulses with very narrow energy resolution (resolving power up to 10000) at high brilliance in the soft and hard X-ray regime. At some of these facilities, attempts were made to push the pulse duration even further down into the range of attoseconds [64, 65]. Those XFELs are based on very long linear accelerators, employing self-amplified spontaneous emission (SASE). In comparison to the slicing method, no additional laser is needed. An electron bunch of homogeneous density accelerated close to the speed of light can travel alongside its own radiation, when being wiggled in an undulator. The emitted light is only slightly faster and surpasses the electron bunches. At each undulator period the electron bunch is modulated by the co-propagating light. Depending on their relative phase to the photons, the electrons in the bunch will be accelerated or decelerated, forming a periodic density distribution at the radiation wavelength [66]. This is called micro-bunching. Under favorable conditions coherent emission occurs, leading to self-amplification of the micro-bunching process and intensity gain at the radiation wavelength over many undulator periods [67].

This new generation of X-ray pulse sources enables experiments, which rely on a very high photon count and at the same time require high energy resolving power and femtosecond time resolution.

This thesis presents an experiment based on time-resolved RIXS, a method which is greatly facilitated by FEL generated X-ray pulses and allows to selectively track ultrafast electronic excitations.

2.5 Atomistic calculations

In this thesis, the $4f$ electronic transitions setting in after optical excitation of terbium metal were experimentally observed in time-resolved M_5 edge XAS and $N_{5,4}$ RIXS spectra. M_5 XAS probes transitions from the $3d$ to the $4f$ shell while $N_{5,4}$ RIXS studies resonant inelastic scattering from $4d^{10}4f^n$ to $4d^9 4f^{n+1}$ intermediate states and $4d^{10}4f^{n*}$ final states. The analysis of the pump-induced spectral changes relies on atomistic calculations, proven to be well suited to determine transition probabilities into the strongly localized $4f$ shell of rare-earth metals. The description of the X-ray spectra can be based on the atomic $4f$ multiplets as the $4f$ states do not form broad bands, but instead exhibit discrete atomic-like energy levels. This holds true even for laser excited samples [68].

In order to simulate the atomistic XAS and RIXS spectra for the excited sample, the spectrum for the $4f$ ground state will be superposed with spectra for energetically higher $4f$ multiplets, fitting the spectral changes observed in the experiments.

X-ray absorption and emission processes mediate between different atomic configurations defining possible $4f$ initial and final states in XAS. In RIXS a possible intermediate state is taken into account additionally. These atomic configurations can be described by a ${}^{2S+1}L_J$ format, with the orbital angular momentum L, the spin angular momentum S and J as the total angular momentum.

The energy for such a configuration is given by the Schrödinger equation for a free atom:

$$H_{\mathrm{ATOM}} = \sum_{N} \frac{p_{\mathrm{i}}^2}{2m} + \sum_{N} \frac{-Ze^2}{r_{\mathrm{i}}} + \sum_{pairs} \frac{e^2}{r_{\mathrm{ij}}} + \sum_{N} \zeta(r_{\mathrm{i}}) l_{\mathrm{i}} \cdot s_{\mathrm{i}}.$$

In this equation, N stands for the number of electrons, $\frac{p^2}{2m}$ is the kinetic energy of each electron, $\frac{Ze^2}{r}$ describes the electrostatic interaction between electrons and the nucleus, $\frac{e^2}{r}$ is the electron-electron repulsion, while the spin-orbit coupling for each electron is contained by $l \cdot s$.
In a given configuration the kinetic energy as well as the electrostatic interaction is equal for all electrons. The corresponding terms can be summarized to an average energy H_{av}. Furthermore the electron-electron repulsion can be split into a spherical average and a non-spherical part. Thereby the Hamiltonian can be separated into an average part, given by H_{av} and the spherical part of the electron-electron repulsion, and into a form giving part, including the non-spherical part of the electron-electron repulsion (H'_{ee}) and the spin-orbit coupling (H_{ls}). The average part leads to an energy shift of the whole spectrum. This part will be neglected in the atomistic calculations. It will be included later in the simulations to align the calculated and measured spectra by means of an energy shift.
The relative energy of an electronic configuration can be calculated by the corresponding matrix elements with the effective electron-electron interaction H'_{ee} and the spin-orbit coupling H_{ls} [69]. For example, the general formulation of the matrix element for the effective electron-electron interaction is:

$$\left\langle {}^{2S+1}L_J \left| \frac{e^2}{r_{12}} \right| {}^{2S+1}L_J \right\rangle = \sum_{\mathrm{i}} f_{\mathrm{i}} F^{\mathrm{i}} + \sum_{\mathrm{i}} g_{\mathrm{i}} G^{\mathrm{i}}.$$

$F^{\mathrm{i}}(f_{\mathrm{i}})$ is the Slater-Condon parameter for the radial part of the direct Coulomb repulsion and the Coulomb exchange interaction, while $G^{\mathrm{i}}(g_{\mathrm{i}})$ is for the angular part. Depending on the involved configurations, the f_{i} and g_{i} are mostly zero except for certain integer values of i [69].
The M_5 XAS and $N_{5,4}$ RIXS experiments presented in this thesis probe transitions from the $3d$ or $4d$ states into the unoccupied $4f$ states. For these transitions Slater-Condon parameters must be included that correspond to d-f interaction as well as for f-f interaction. d-d interaction will be neglected, because it is expected to only play a minor role.
The initial state in these calculations corresponds to the trivalent ion, involving a $4f^n$ configuration and completely filled core levels. In this case

the radial part originates solely from direct f-f interaction and is given by f_0, f_2, f_4 and f_6. The angular part is only present for inter-shell interaction. Because all lower shells are fully filled in the initial state, no inter-shell interaction occurs and the angular part for the initial state is zero. The value for the static part of the direct coulomb interaction f_0 is based on the reduced f_2, f_4 and f_6 values:

$$f_0(ff) = \frac{4}{195} \cdot f_2 + \frac{2}{143} \cdot f_4 + \frac{100}{5577} f_6 .$$

In the final/intermediate state either a $3d^9 4f^{n+1}$ or a $4d^9 4f^{n+1}$ state is occupied. Here, the radial part consists of f_0, f_2, f_4 and f_6 for f-f interaction, while additionally f_2 and f_4 are included for d-f interaction. The angular part stems from the d-f interaction and is given by g_1, g_3 and g_5. The static part of the direct Coulomb interaction for the final state is:

$$f_0(ff) = \frac{4}{195} \cdot f_2 + \frac{2}{143} \cdot f_4 + \frac{100}{5577} \cdot f_6$$

and

$$f_0(df) = \frac{3}{70} \cdot g_1 + \frac{2}{105} \cdot g_3 + \frac{5}{231} \cdot g_5 .$$

The calculations shown in this thesis were performed by P. Miedema for the terbium M_5 XAS and by R.-P. Wang for the terbium $N_{5,4}$ RIXS experiment using the Quanty routine [70, 71, 72].

The used Slater-Condon parameters stem from T. Thole's multiplet extension [73] to the Cowan code [74], which underlies the CTM4XAS interface maintained by de Groot *et al.* [69]. A table for those values can be found in the Appendix A.1. However, as the Hatree-Fock approximation usually overestimates the energies for the electron-electron interaction, Slater reduction factors need to be applied. These factors are dependent on the probed absorption resonances and are influenced by the target sample and hence must be optimized for each experiment individually.

For the XAS calculation of the terbium $M_{5,4}$ edge, adjustment with experimental data resulted in the Slater reduction factors $F_{ff} = 0.61$, $G_{df} = 0.70$, and $F_{df} = 0.80$. The calculated imaginary part of the scattering amplitude for $3d \rightarrow 4f$ transitions starting in the ground state or the first six excited multiplets are shown in Fig. 2.3. The multiplets show clear differences in their shape. The corresponding excitation energies for those multiplets are shown in Tab. 2.1.

To simulate RIXS spectra at the terbium $N_{5,4}$ edge, the Kramers-Heisenberg formula was used. According to the experimental setup, the emission angle was set to 105°, while the incident angle was 25°. The best agreement between the unpumped experimental data and the calculations was found for the Slater reduction factors $F_{ff2} = 0.80$, $F_{ff4} = 0.91$, $G_{df} = 0.60$ and $F_{df} = 0.60$. The corresponding excitation energies for the first seven inner shell excitations are also shown in Tab. 2.1.

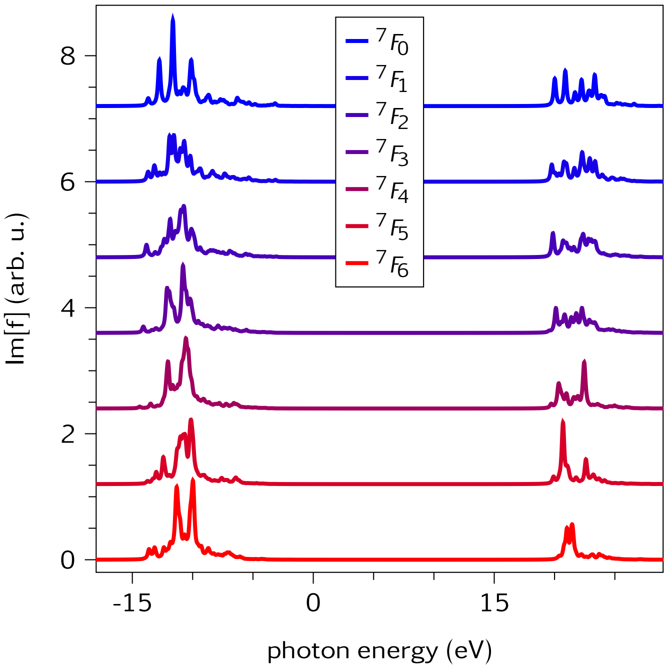

Figure 2.3: Calculated imaginary part of the scattering amplitude of the terbium M_5 and M_4 edge for the ground state ($^7F_6$) and the first six excited multiplets (^7F_J). Calculations were done by P. Miedema.

Table 2.1: Calculated excitation energies (E_i in eV) for the first seven inner shell excitations in terbium metal. The calculation differ by the Slater reduction factors.

	$^7F_6$	$^7F_5$	$^7F_4$	$^7F_3$	$^7F_2$	$^7F_1$	$^7F_0$	$^5D_4$
P. Miedema	0	0.28	0.41	0.54	0.62	0.68	0.71	1.71
R.-P. Wang	0	0.262	0.436	0.533	0.652	0.701	0.73	2.649

Chapter 3

Methods and experiment

This chapter describes the different experimental techniques and facilities used as well as the samples studied in this thesis.

3.1 Time-resolved X-ray absorption spectroscopy (tr-XAS)

X-ray absorption spectroscopy (XAS) is an originally synchrotron-based technique that becomes increasingly relevant also in the laboratory environment, driven by the progress in higher-harmonics-generation from table-top setups. XAS provides detailed insight into the chemical, electronic and magnetic properties of solids. This chapter will give an overview on XAS; for an in-depth explanation please refer to, e.g., [27].

If light passes through a thin film, it will partially be absorbed. The respective intensity reduction is caused by the photo-electric effect and follows the Lambert-Beer law:

$$I_T(d) = I_0 \cdot e^{-\mu(E) \cdot d}, \tag{3.1}$$

where $I_T(d)$ is the intensity after passing through the sample of thickness d, I_0 denotes the intensity before interaction with the sample and $\mu(E)$ stands for the absorption coefficient at a given X-ray energy E. Because I_0 and d are specific for each experiment and sample, the property of interest in physics is $\mu(E)$.

However, because the sample thickness is often not known well enough but constant, the X-ray absorption is typically evaluated using the extinction XA:

$$XA = -ln(I_T/I_0) = \mu(E) \cdot d. \tag{3.2}$$

The extinction crucially depends on the elements comprised by the sample and exhibits sharp resonances for X-ray energies corresponding to the binding energy of specific core-level electrons. The near-edge X-ray absorption fine structure at these absorption edges corresponds to the transition probability from the core levels to the unoccupied states and therewith carries information on the local electronic and magnetic structure.

A second contribution to the extinction comes from excitation into the continuum [25]. Those lead to a broad-band increase in absorption at the high energy side of an absorption edge. This is called the *edge jump*. Including the edge jump, the extinction can be formulated as:

$$XA = \mu(E) \cdot d + \text{edge jump}(E). \tag{3.3}$$

The absorption of a photon is directly followed by multiple-electron coherent and incoherent scattering, fluorescence- and Auger-electron-decay as well as by electron-hole pair creation [26]. All those processes lead to relaxation back to the ground state.

In the XAS experiments on terbium presented in this thesis a transition from the $3d$ core levels to the unoccupied $4f$ density of states is driven resonantly. A total energy scheme illustrating this mechanism is shown in Fig. 3.1. As the $3d$ electrons are energetically split by spin-orbit coupling, two absorption edges can be found for the $3d$-$4f$ transition. These resonances are called M_5 and M_4 edge for the excitation from the $3d_{5/2}$ and the $3d_{3/2}$ shell, respectively, and appear at energies around 1241 and 1277 eV [75]. At the $M_{5,4}$ edges, transitions into the unoccupied $5d6s$ valence states are suppressed. Therefore, they represent pure transition probabilities into the $4f$ states, making them highly suited to investigate the $4f$ electronic structure.

With the XAS probe the temporal response of the $4f$ electronic state in different rare-earth metals after near-infrared laser excitation can be investigated. Time resolution is achieved in a pump-probe scheme, in which the so-called pump pulse is creating an event and a so-called probe pulse captures the physical quantity, here the XAS signal. By changing the delay between these two pulses, the temporal profile of the probe signal can be mapped over time. The experimental time-resolution depends on the respective duration of the pump and probe pulse, as well as on the correlation between them, including jitter and long-term temporal drifts.

The near-infrared pump pulse excites mainly the more delocalized $5d6s$ valence electrons, because no $5d$-$4f$ or $4f$-$4f$ dipole transitions can be driven resonantly at these photon energies. Furthermore, excitations

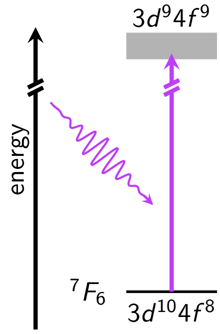

Figure 3.1: Total energy scheme for the XAS process in terbium. Upon absorption of an X-ray photon of about 1237 eV for the M_5 edge or 1269 eV for the M_4 edge a 3*d* electron is excited into the unoccupied 4*f* states, hence transiently a $3d^94f^9$ state gets occupied.

within the 4*f* electronic system are weak due to dipole selection rules only slightly lifted due to the non-rotational crystal symmetry.
In the two XAS experiments performed at the EuXFEL and the FemtoSlicing facility at BESSY II, near-infrared pump-laser pulses were used to deposit energy into the 5*d*6*s* valence states and, via X-ray-probe pulses at the energy of the terbium $M_{5,4}$ resonance, ultrafast changes in the 4*f* electronic structure were studied.

3.1.1 tr-XAS at EuXFEL

A change of the multiplet occupation in the 4*f* system causes slight variations in the spectral shape of the absorption signal. Probing them after optical pumping requires an energy resolving power in the range of the lifetime broadening and a time resolution down to tens of femtoseconds. Currently, the only sources combining these parameters with high photon flux and core selective probe in the soft X-ray regime are free-electron lasers.
A tr-XAS experiment was performed at the SASE3-beamline of EuXFEL in Schenefeld, Hamburg. This beamline uses self-amplified spontaneous emission (see Chapter 2.4.2) to create ultrashort, linear polarized X-ray pulses. The EuXFEL SCS Instrument [19] was used to measure ultrafast changes of the X-ray absorption in terbium metal at the $M_{5,4}$ edges around 1237 and 1269 eV, respectively. This instrument (simplified scheme in Fig. 3.2) features an X-ray gas monitor to measure the intensity of the

incoming X-rays (I_0) and a cwd diamond scintillator as transmission intensity monitor (TIM) to detect the transmitted intensity (I_T). An energy resolving power of $E/\Delta E = 3500$ can be achieved for energies around 1 keV as used to measure the $M_{5,4}$ edges of rare-earth metals.

The SASE3 PP laser system supplies the experiment with 800 nm (1.55 eV) pulses at 10 kHz for pumping the sample. An incident pump fluence of $(10 \pm 2)\,\mathrm{mJ\,cm^{-2}}$ was used to excite the rare-earth transmission samples. With a size of $(0.28 \times 0.2)\,\mathrm{mm}^2$ the pump-laser spot was sufficiently larger than the X-ray-probe-beam spot of $(0.1 \times 0.1)\,\mathrm{mm}^2$ to ensure a nearly homogeneous excitation profile in the probed volume. By cross-correlation of optical pump and X-ray-probe pulses, a temporal resolution of 65 fs was determined. Due to slower drifts, only a time resolution of 200 fs was achieved for very long scans.

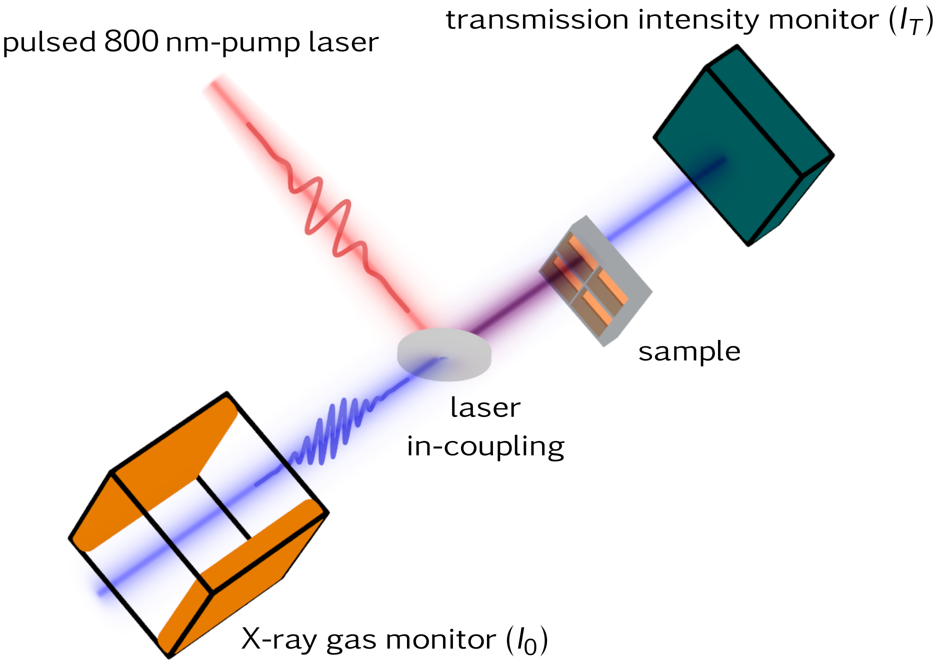

Figure 3.2: Simplified scheme of the SCS endstation at the SASE3 beamline at EuXFEL. The intensity of the incoming X-ray beam is measured with an X-ray gas monitor. The 800 nm-pump laser is coupled inline with the X-rays. After interaction with the sample, the transmitted X-ray intensity is detected by a transmission monitor.

3.1.2 XAS at BESSYII

The 3rd generation synchrotron radiation source BESSY II in Berlin offers great capabilities for XAS experiments. Static measurements can be performed at the PM3 beamline [76, 77]. This beamline supplies the attached endstation with high-intensity X-rays in the range of 20 – 2000 eV photon energy with variable polarization at high energy resolution and high stability. A resolving power of up to 34000 can be achieved at an energy of 64 eV. However, to keep a high flux even for higher energetic X-rays around the terbium M_5 edge, a larger exit slit width of 50 µm was used, with a resolving power of 20000.

Experiments can be performed either in the permanently attached PM3 scattering chamber or in variable endstations, attachable to the open port behind the PM3 scattering chamber. The PM3 scattering chamber itself features a decoupled rotation of the sample and the detector around the same vertical axis, enabling measurements in various measurement geometries within the scattering plane. A rotatable magnet provides a magnetic field up to 200 mT in the same plane. The sample manipulator is equipped with a cryostat and internal heating for temperature control down to LHe-temperatures, enabling precise regulation of the sample temperature in a range from around 20 to 300 K .

For time resolved XAS studies pump-probe experiments can be performed at the FemtoSpeX slicing facility (FemtoSlicing) in the DynaMaX scattering chamber installed to the UE56/1 ZPM beamline [21, 22, 23]. A simplified scheme of the setup is shown in Fig. 3.3. At this facility the slicing method (described in detail in Chapter 2.4.1) is utilized to create femtosecond X-ray pulses. A pulsed 800 nm Ti:Sa laser, which is synchronized to the master clock of the BESSY II accelerator, is used as seed laser for the slicing and as pump laser. In the U139 modulator the electron bunches are energy modulated by the slicing laser. Radiation of circularly polarized X-ray pulses occurs in the UE56/1 radiator. In order to optimize the photon flux, high transmission optics and a reflection zone plate monochromator with 9 zone plates for the mostly studied elements between 410 and 1333 eV are used. The pump laser gets coupled inline with the X-rays and both are focused onto the sample. The delay between pump and probe pulse can be adjusted via a delay stage in the pump-laser path. The pump laser operates at half the frequency of the slicing laser, such that every second X-ray pulse measures the signal from the unpumped sample.

The DynaMaX scattering chamber features, similar to the PM3 scattering chamber, independent rotational degrees of freedom for sample and

detector in the scattering plane, enabling transmission, reflection and diffraction experiments. Temperature control down to 20 K is possible.
Particularly the fast ramping 3D vector magnet makes the DynaMaX endstation a state of the art setup for time resolved experiments. Three pairs of coils provide up to 1.5 T inplane and 0.75 T vertical to the scattering plane, enabling large fields and precise control over them in all spatial directions.
After interaction with the sample, the X-rays are detected by a gated avalanche photo diode, operated close to the breakthrough voltage, therewith facilitating single photon counting.
The DynaMaX setup uniquely allows to probe the magnetic dynamics element selectively on ultrafast timescales for $L_{3,2}$ absorption edges of 3*d* transition metals and $M_{5,4}$ resonances of 4*f* rare-earth elements [24].

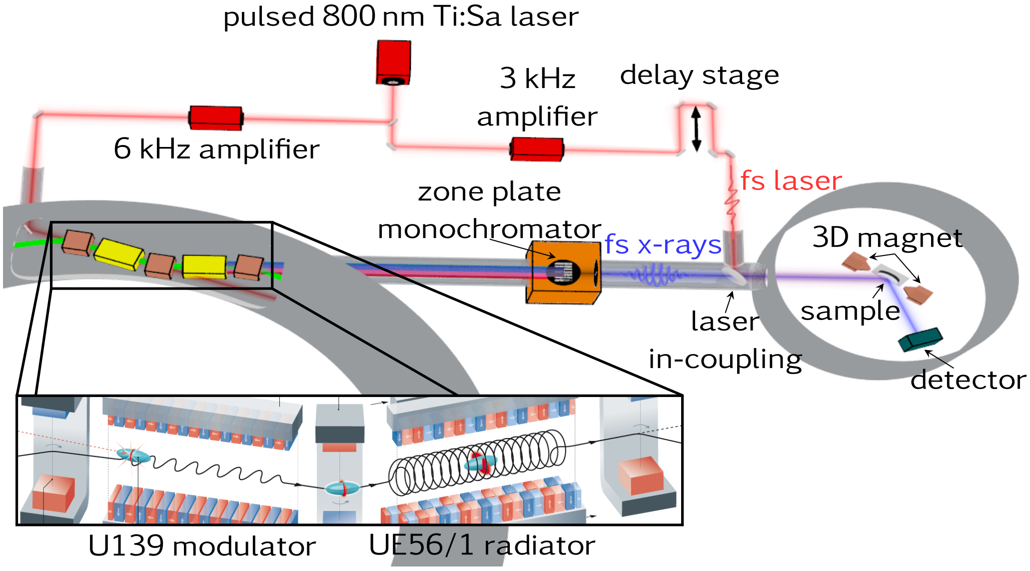

Figure 3.3: Simplified scheme of the FemtoSlicing facility at BESSY II. Adapted from [22], inset taken from [78]. The slicing method is applied by modulating the electron bunches at a 6 kHz frequency. The emitted X-ray pulses are monochromatized by a reflection zone plate monochromator. The scattering endstation is equipped with a 3D vector magnet that can apply fields up to 1.5 T. A 3 kHz pump laser is coupled inline with the X-rays. The difference in repetition rate between electron bunch modulation and the pump pulses enables parallel recording of spectra for the pumped and unpumped sample.

3.2 Resonant inelastic X-ray scattering (RIXS)

Resonant inelastic X-ray scattering (RIXS) is a photon-in photon-out process which is used as spectroscopy method by analyzing inelastically scattered X-ray photons with regard to the energy loss they experienced in the scattering process. The energy loss stems from intrinsic excitations in the material which can be of electronic, magnetic or structural nature. With tunable X-rays energy and angular momentum transfer paths can be studied element and state selectively, showing a strong dependence on the excitation energy as well as on the photon polarization.

Choosing the excitation energies such that they coincide with specific X-ray absorption edges, the intrinsically low RIXS cross-section and hence the amount of inelastic scattered photons can be strongly increased. Additionally, the experimental geometry is optimized in a way that specular reflection is suppressed to not overshadow the RIXS signal.

The analysis of the RIXS spectra presented in this thesis focuses on electronic excitation in terbium metal. A broader discourse into the RIXS technique is given in different review articles [28, 29, 30].

For a basic understanding of the RIXS process in terbium, a closer look into the possible excitation and relaxation pathways is necessary. In case of the performed experiment the RIXS signal at the $4d \rightarrow 4f$ transition, *i.e.* the $N_{5,4}$ resonance, was studied. Because of the localized character of the $4f$ electronic states, $4f$ RIXS spectra can be well described within an atomistic framework, even for metallic terbium. Figure 3.4 gives an energy scheme for the RIXS process at the terbium $N_{5,4}$ edge. At this absorption edge an electron from $4d$ core levels is excited into an empty $4f$ state, leaving behind a $4d$ hole, while changing the $4f$ electronic configuration. This way, a transition from the $4d^{10}4f^{8}$ initial state, where the $4f$ electrons occupy the ${}^{7}F_{6}$ ground state multiplet, into a transient $4d^{9}4f^{9}$ intermediate state is provoked.

For the relaxation into the final state different transitions can occur. They can be grouped into three categories:

i) energy conserving: First and foremost the excited electron can relax to the hole it left behind, bringing the $4f$ system back to the ${}^{7}F_{6}$ state. This will result in an emitted photon of exactly the same energy as the absorbed photon. These photons form the so called elastic peak at zero energy loss.

ii) spin conserving: In the second scenario, another electron in the $4f$ shell relaxes, while conserving the spin, leading to an ${}^{7}F_{J}$ state with $J = 5, 4, 3, 2, 1$ or 0. The emitted photon energy is reduced according to the energy difference between ${}^{7}F_{6}$ ground state and ${}^{7}F_{J}$ multiplet.

iii) spin changing: Lastly, due to the hybridization between states with the same J but different S and L, also states with altered spin values can be reached. Such transitions allow for changes in S, L and J resulting in a huge number of inelastic lines in the RIXS spectrum. Occupying these states with changed spin requires significantly higher energies in terbium. Additionally, because RIXS is a photon-in photon-out process involving only the absorption and emission of two photons, also the maximum change in total angular momentum provoked can not be greater than two ($max|\Delta J| = 2$).
The energy levels of the different $4f$ multiplets can be calculated as described in Chapter 2.5. A list of them was taken from [79] and is shown in Tab. 3.1. However, these values are only valid in the case of ionized atomic terbium. For metallic terbium, grown as a crystal, they can be reduced by the crystal field, influencing the d-d, d-f and f-f interaction. The intensity of the RIXS elastic contribution and inelastic lines is given by the probability for the different transitions. Thus, RIXS spectra are strongly dependent on the exciting wavelength, the polarization of the incoming light, as well as the crystal field of the sample.
For the time-resolved RIXS experiment presented in this thesis the transition to the $^5D_4$ state was very well suited for investigation, because it is energetically well separated from other possible transitions and can be easily resolved.

Table 3.1: Energy-level assignments in Tb^{3+} $4f$ multiplets taken from [79]. Values are the energy position above the ground state and are given in eV. Gray colored states can not be reached in the RIXS process ($|\Delta J| > 2$).

$^7F_6$ 0	$^7F_5$ 0.26	$^7F_4$ 0.42	$^7F_3$ 0.54	$^7F_2$ 0.62	$^7F_1$ 0.68	$^7F_0$ 0.71	$^5D_4$ 2.54	$^5D_3$ 3.27	$^5G_6$ 3.28
$^5L_{10}$ 3.37	$^5G_5$ 3.45	$^5D_2$ 3.49	$^5G_4$ 3.51	$^5L_9$ 3.53	$^5G_3$ 3.60	$^5L_8$ 3.62	$^5L_7$ 3.65	$^5L_6$ 3.66	$^5G_2$ 3.67
$^5D_1$ 3.80	$^5D_0$ 3.87	$^5H_7$ 3.91	$^5H_6$ 4.09	$^5H_5$ 4.20	$^5H_4$ 4.27	$^5F_5$ 4.33	$^5H_3$ 4.34	$^5I_8$ 4.37	$^5F_4$ 4.39
$^5F_3$ 4.53	$^5I_7$ 4.55	$^5F_2$ 4.61	$^5F_1$ 4.66	$^5I_4$ 4.66	$^5I_6$ 4.68	$^5I_5$ 4.72	$^5K_9$ 4.84	$^5K_8$ 5.05	$^5K_7$ 5.16

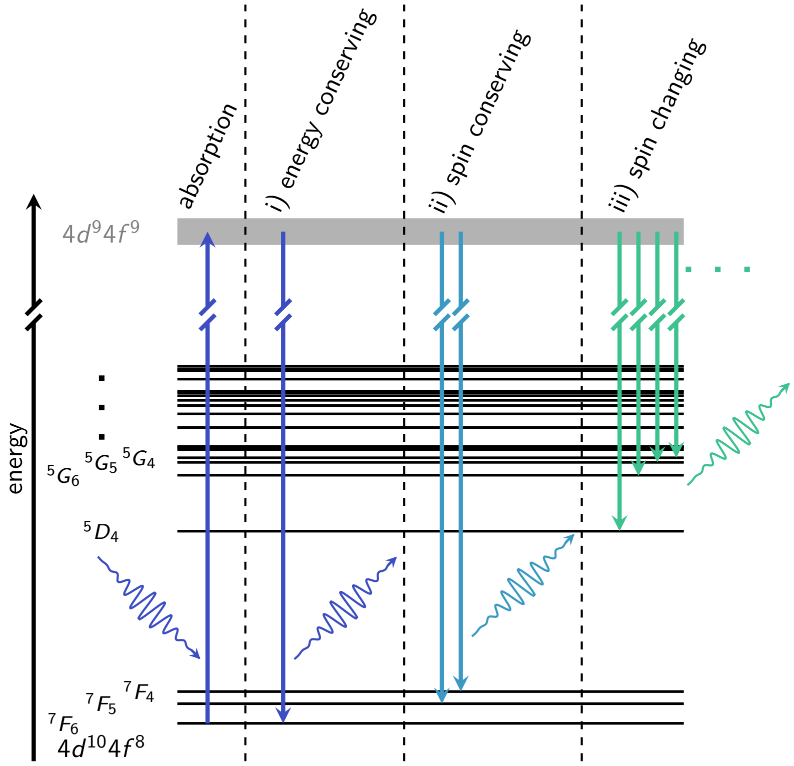

Figure 3.4: Energy scheme for the absorption and the different relaxation channels during the RIXS process at the terbium $N_{4,5}$ edge. The absorption excites the system into a transient $4d^94f^9$ state. Following the absorption, either the previous transferred electron can relax by emitting a photon with zero loss or another electron from the $4f$ shell relaxes, leading either to a state with the same or changed spin. The energy loss measured in RIXS corresponds to the energy difference between the ground state $^7F_6$ and the resulting final state. Since only two photons are involved the maximal change in total angular momentum J between ground and final state is 2.

3.2.1 tr-RIXS at FLASH

Time-resolved RIXS experiments, capable to resolve alteration of the electronic structure, *i.e.* after optical pumping, require time resolution in the femtosecond regime and meV energy resolution. Currently, only FELs provide the required parameters at sufficiently high photon flux.

The RIXS experiment presented in this thesis has been performed at the PG1 Raman beamline of FLASH at DESY in Hamburg, Germany. This FEL beamline reaches energies between 36 and 200 eV with an energy resolving power of ~1700. This is optimal for RIXS measurements at the $N_{4,5}$ edge of terbium at around 147 eV.

The PG1 TRIXS endstation [20] (simplified schematic in Fig. 3.5) allows for grazing incident angles of about 25° to the sample surface plane and a collection angle for the outgoing photons close to the sample surface normal around 105° with respect to the sample surface plane. This geometry ensures that the specular reflected X-rays do not affect the RIXS signal while at the same time, elastically scattered photons are suppressed for incident p-polarization. Within a grating spectrometer the collected photons are spatially separated according to their energy and then recorded by a CCD camera. For incident energies of about 147 eV a resolution of 33 meV/px is achieved. However, because the grating spectrometer uses a parabolic mirror, only energies close to the focus energy are well resolved. To counteract the resolution off-focus, all spectra over an extended energy loss range were stitched together from spectra taken at different energy foci of the spectrometer. Still, the ^7F_J lines at low energy loss below 1 eV are overshadowed by the strong elastic peak and can not be resolved. Hence, the analysis focuses on the energetically higher lying loss features between 2.5 and 4 eV.

A pulsed infrared (IR) laser with about 1030 nm wavelength ($h\nu = 1.2\,\mathrm{eV}$) is used for pumping the sample [80]. The laser in-coupling is collinear to the X-rays, and the IR laser with a spot size of $(150 \times 150)\,\mu\mathrm{m}^2$ is sufficiently larger than the X-ray spot size on the sample of $(20 \times 40)\,\mu\mathrm{m}^2$. Due to the penetration depth for the pump laser being much higher than for the probe pulses at a resonant X-ray energy, the whole probed volume is homogeneously pumped. The PG1 setup provides a time resolution of about 300 fs. All time traces were recorded using a delay hopping routine, that switches randomly between delays to avoid any cross-correlations.

The RIXS measurements were performed in the paramagnetic phase of terbium at room temperature.

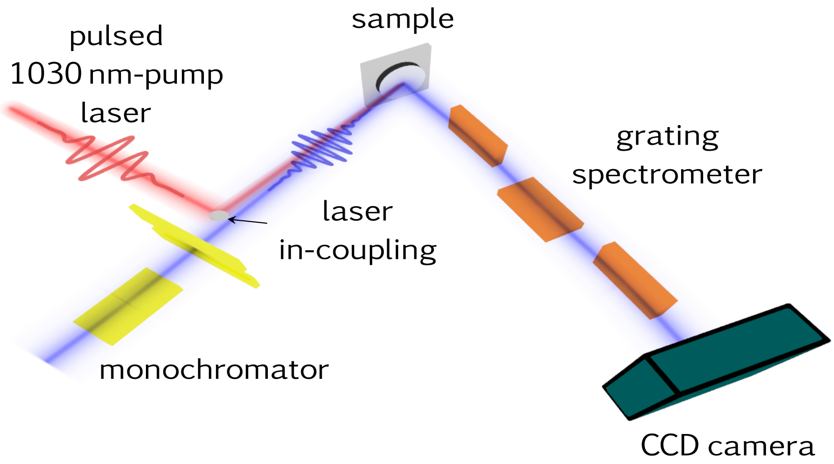

Figure 3.5: Simplified scheme of the experimental setup at the PG1 beamline [20]. The monochromatized, p-polarized X-ray pulses hit the sample at an incident angle of about 25° to the sample surface plane. The scattered X-rays are collected at an angle of about 105°. The 1030 nm-pump-laser pulses are coupled in such, that they propagate collinearly with the X-rays.

3.3 Sample preparation

The XAS and RIXS experiments described above require different sample compositions, which needed to be tailored to experimental parameters, such as measurement geometry or X-ray excitation energy. Therefore, high quality rare-earth samples (gadolinium and terbium) were grown on different substrates with thicknesses adjusted to the experimental geometries and with different buffer and capping materials. A schematic overview of the sample compositions is given in Fig. 3.6.

The Weinelt workgroup setup a dedicated molecular beam epitaxy (MBE) chamber at the PM3 beamline of BESSY II. This chamber features space for up to six different evaporation sources and includes analytical tools like low-energy electron diffraction (LEED), reflection high-energy electron diffraction (RHEED), mass-spectrometer and quartz micro balance. A sputter deposition growth unit attached to the MBE chamber diversifies the growing conditions and parameters and further allows for deposition of various materials. Additionally, an in-vacuum transfer to the PM3 scattering endstation is possible, giving access to static XAS and XMCD measurements.

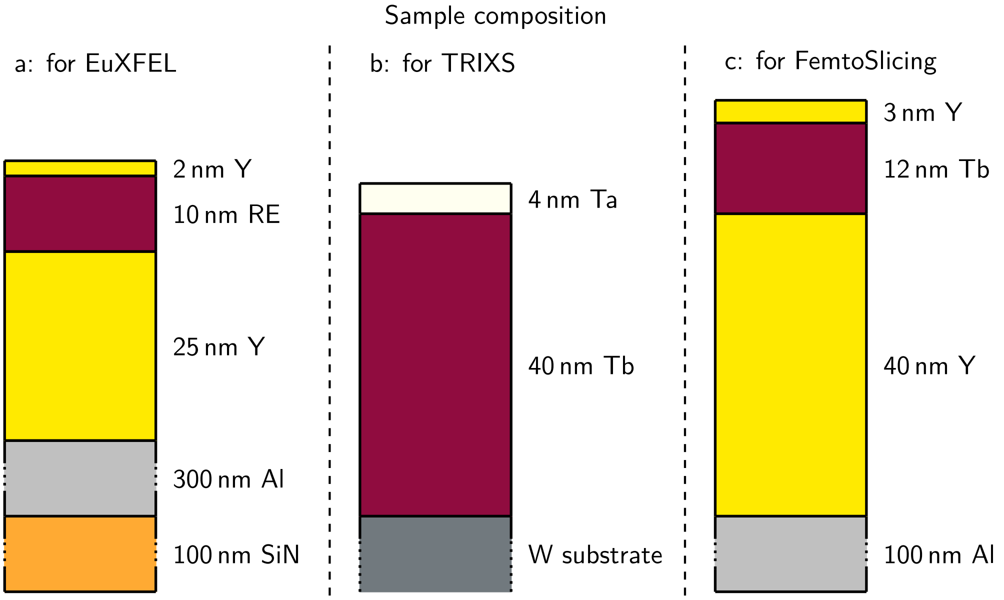

Figure 3.6: Overview of the different sample compositions.
a: Y(2 nm)/RE(10 nm)/Y(25 nm)/Al(300 nm)/SiN(100 nm foil, substrate) for EuXFEL.
b: Ta(4 nm)/Tb(40 nm)/W(substrate) for TRIXS.
c: Y(3 nm)/Tb(12 nm)/Y(40 nm)/Al(100 nm foil, substrate) for FemtoSlicing.

3.3.1 Rare-earth transmission samples for XAS at EuXFEL

For the XAS experiments at the EuXFEL thin-film samples were used, allowing for X-ray transmission. Therefore, a 100 nm thin SiN foil was chosen as substrate. To improve the heat distribution in the sample after pumping and therewith protecting the SiN foil from ripping, a 300 nm aluminum heat sink layer was put on top the SiN foil. A 25 nm yttrium buffer layer was grown on the aluminum film to reduce the strain on the rare-earth layer grown on top and to protect it from oxidation. The metallic rare-earth (RE) film with a thickness of 10 nm was grown at a pressure of 10^{-9} mbar during the evaporation process. To protect the rare-earth layer against ambient condition the sample was capped with 2 nm yttrium.
This procedure leads to a polycrystalline rare-earth layer, which allows for X-ray transmission at the $M_{5,4}$ resonance. With an overall sample configuration of Y(2 nm)/RE(10 nm)/Y(25 nm)/Al(300 nm)/SiN(100 nm foil, substrate) metallic terbium and gadolinium films were studied at EuXFEL.

3.3.2 Terbium bulk sample for RIXS at FLASH

With the small scattering cross-section in RIXS, experimental geometry and samples need to be adjusted to maximize the detected signal. Therefore, a detection angle close to the sample surface normal and a sample thickness larger than the photon escape depth were used. As substrate a mono-crystalline tungsten (W) crystal with (110) orientation and well polished surface was chosen. This allows to grow highly ordered rare-earth films, because of the lattice matching between the W(110) surface and the rare earth hexagonal lattice. The minimal amount of strain enables deposition of a nearly defect-free rare-earth metal layer.
After cleaning the tungsten crystal of all absorbents by repeated flashing to 1800 °C, 40 nm of terbium were grown on top using MBE with a deposition rate of about 0.52 nm/min. Afterward, the sample was annealed to 600 – 630 °C for 5 min. To protect the terbium layer from contamination during the transport outside of vacuum, a capping layer of 4 nm tantalum (Ta) was grown on top of the terbium layer by magnetron sputtering at a deposition rate of 0.07 nm/s. The resulting sample configuration is Ta(4 nm)/Tb(40 nm)/W(substrate).
The sample was statically pre-characterized in the scattering endstation of the PM3 beamline at BESSY II. Figure 3.7 a shows the reflected signal at the terbium M_5 edge for parallel and antiparallel magnetization direction measured with circular polarized X-rays. For a grazing incident angle of 5° and a sample temperature of 100 K the signal is shown for different ages of the sample. The red colored lines show the data recorded directly after growth and in-vacuum transfer to the measurement chamber. The blue lines represent the data taken after storing the sample for one day in ambient conditions and the green data set was measured after 14 days of exposure to ambient conditions. The solid and dashed lines for each color show the data for opposite magnetization field directions. Their difference represents the XMCD. From this data the normalized XMCD can be calculated as $\frac{2*|I_{M+}-I_{M-}|}{|I_{M+}+I_{M-}|}$ and is shown in Fig. 3.7 b with the same color coding. It shows, that the XMCD is stronger off-resonant than at the resonance at 1240 eV. This can be explained considering the X-ray penetration depth. Figure 3.7 c shows the X-ray absorption recorded via the drain current signal corresponding to the number of free charge carriers created by X-ray absorption. A high absorption at the resonance leads to a shallow penetration depth while going off-resonance to lower absorption leads to larger sampling depth. From the reduced XMCD for smaller sampling depth it can be concluded that the sample is less magnetic in the region close to

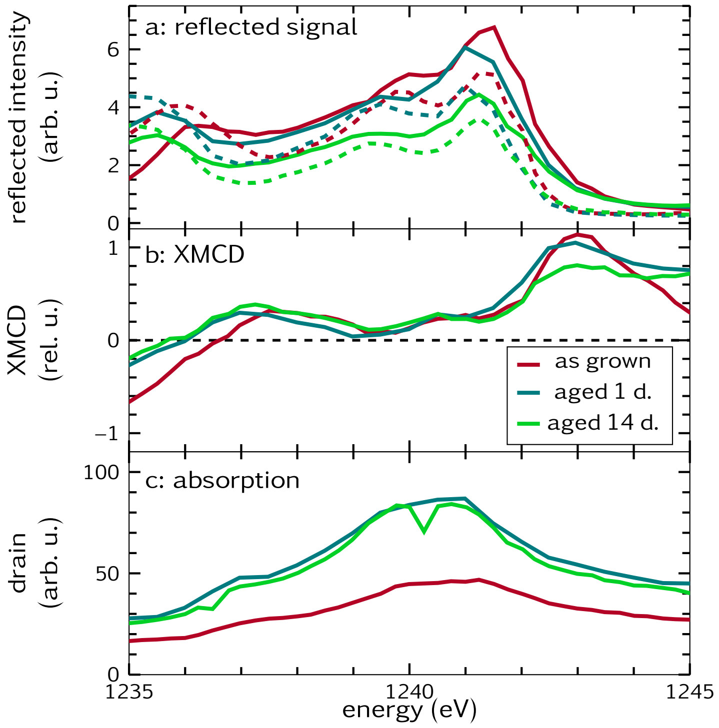

Figure 3.7: Static pre-characterization of the terbium RIXS sample. Data were recorded at the PM3 beamline of BESSY II. The red colored lines correspond to a measurement directly after growth and in-vacuum transfer to the X-ray scattering chamber, the blue lines represent measurements after one day of exposure to ambient conditions and the green colored data were recorded after 14 days of exposure.
a: shows the reflected signal at an incident angle of 5°. The solid and dashed lines were recorded for opposite magnetic field directions.
b: displays the XMCD calculated from a. The sample seems to be less magnetic at the surface (resonance) than in deeper regions (see text).
c: presents the absorption of the sample, measured via a drain current signal.

the surface while being well magnetic in deeper regions. This is most likely caused by the sputtering process, in which tantalum atoms intermix with the terbium surface layers during deposition and hence affect magnetic order. As RIXS measurements at the $N_{5,4}$ edge are not surface sensitive and with the sample hold at room temperature in the paramagnetic phase, the metallic terbium layer is nicely suited for RIXS investigation at the PG1 beamline of FLASH.
Regarding the aging process of the sample the exposure to ambient conditions led to an increase of the absorption during the first day. This can

be explained, e.g., by oxidation of the surface leading to reduced X-ray reflectivity and thus increased absorption of photons. Prolonged exposure to ambient conditions for 14 days did not change the sample noticeably.

3.3.3 Terbium transmission sample for XAS at FemtoSlicing

For the XAS experiments at the FemtoSlicing facility a thin-film transmission sample has been prepared. The substrate was a 100 nm aluminum foil on a copper frame. A 40 nm yttrium layer grown on the substrate with a deposition rate of 0.2 nm/min acts as buffer, that protects the terbium film against contamination from the substrate and reduces the strain in the terbium film due to lattice matching between yttrium and terbium. The actual sample was grown as 12 nm terbium film with a deposition rate of 0.6 nm/min. The sample was capped with additional 3 nm yttrium grown at a deposition rate of 0.3 nm/min as oxidization protection. The base pressure of the growth chamber was 5×10^{-10} mbar and increased to 1×10^{-9} mbar during the growth process. The overall sample composition is Y(3 nm)/Tb(12 nm)/Y(40 nm)/Al(100 nm foil, substrate).

Figure 3.8 a shows the intensity of circular polarized X-rays transmitted through the sample for a photon energy range around the terbium M_5 and M_4 edges and a sample temperature of 150 K. Two spectra for oppositely applied magnetic fields of 1.5 T are depicted. Both exhibit only dips at the M_5 and M_4 edges, characteristic for terbium. However, they reveal a contrast in intensity at both edges. This is a proof for the sample being ferromagnetic when cooled down. As ferromagnetism in 4*f* metals strongly depends on a periodic crystal structure to form, the sample must be at least polycrystalline. For further investigation a hysteresis was recorded at 1238.8 eV (marked as brown dashed line in Fig. 3.8 a). The hysteresis loop (Fig. 3.8 b) shows a coercive field of about 0.25 T and a slope towards saturation. The slope of the hysteresis indicates that the sample has different magnetic domains switching successively. At a magnetic field of 1.5 T the sample is well saturated.

Overall, these measurements show that the sample is a polycrystalline, metallic terbium film of high quality.

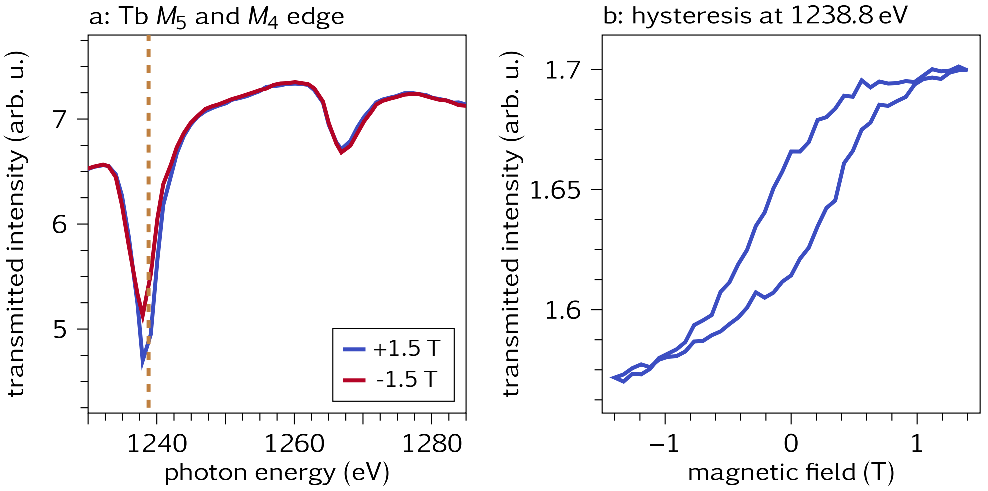

Figure 3.8: a: Transmitted intensity at the M_5 and M_4 edges of terbium measured for oppositely applied magnetic fields of 1.5 T at a sample temperature of 150 K. A clear contrast between the two spectra is visible at the M_5 edge. This proves the sample being ferromagnetic when cooled down. At an energy of 1238.8 eV (brown dashed line) the hysteresis shown in b was measured.
b: Hysteresis at the M_5 edge of terbium. The coercive field is about 0.25 T and the sample is well saturated at 1.5 T.

Chapter 4

4*f* multiplet excitation studied by X-rays

This chapter presents the results from XAS experiments performed at EuXFEL and at the FemtoSlicing facility of BESSY II as well as RIXS measurements from the PG1 beamline of FLASH. The XAS and RIXS signal from rare-earth metals at the $M_{5,4}$ and $N_{5,4}$ resonances, respectively, probes the 4*f* electronic structure with high sensitivity (compare Chapters 3.1 and 3.2).

The central question discussed in this thesis is, how 5*d* and 4*f* electrons interact on ultrafast timescales in terbium metal. To answer this question, pump-probe experiments, in which the 5*d* electrons are excited by an IR-pump-laser pulse and the response in the 4*f* electronic system is probed with X-ray pulses at the $M_{5,4}$ or $N_{5,4}$ edges, were conducted and analyzed.

The results shown in Chapters 4.1 and 4.2 are published as ′N. Thielemann-Kühn, T. Amrhein *et al*. Optical control of 4*f* orbital states in rare-earth metals, Science Advanced **10**, eadk9522 (2024)′[81]

The XAS experiment at the EuXFEL was performed by N. Thielemann-Kühn, T. Amrhein, W. Bronsch, S. Jana, N. Pontius, R. Y. Engel, P. S. Miedema, M. Beye, B. E. van Kuiken, M. Teichmann, R. E. Carley, L. Mercadier, A. Yaroslavtsev, G. Mercurio, L. Le Guyader, N. Agarwal, R. Gort, A. Scherz, M. Weinelt and C. Schüßler-Langeheine. Sample preparation was done by T. Amrhein. N. Thielemann-Kühn and T. Amrhein carried out the data analysis. Atomistic calculations were performed by P. S. Miedema. DFT calculations were performed by D. Legut, K. Carva and P. M. Oppeneer.

The RIXS experiment at FLASH was performed by N. Thielemann-Kühn, T. Amrhein, W. Bronsch, S. Dziarzhytski, G. Brenner, F. Pressacco, R.-P. Wang, J. O. Schunck, M. Sinha, G. S. Chiuzbăian, M. Weinelt and C. Schüßler-Langeheine. Sample preparation was performed by N. Thielemann-Kühn and T. Amrhein. Data analysis was carried out by T. Amrhein. Atomistic calculations were done by R.-P. Wang.

The results shown in Chapter 4.4 are in preparation for publication. The XAS experiment at the FemtoSlicing facility was conducted by B. Salantur, T. Amrhein, M. Mawass, N. Pontius, C. Schüßler-Langeheine and N. Thielemann-Kühn. The samples were prepared by N. Thielemann-Kühn, T. Amrhein and B. Salantur. Data analysis was performed by T. Amrhein and B. Salantur. Some of the shown results are also part of the master thesis of B. Salantur.

4.1 XAS at EuXFEL

One of the time-resolved XAS experiments was setup at the SCS beamline at EuXFEL. As pump stimulus 800 nm-laser pulses were used to excite the 5*d* system, while the M_5 edge of terbium was probed using X-ray pulses at around 1236 eV.

Due to the absorption cross-section, it is safe to assume, that the 800 nm-laser pulses initially excite only the 5*d* electronic system and that energy is deposited only indirectly into the 4*f* subsystem by interaction with the 5*d* electrons or the lattice. As for the probe energy around the M_5 resonance, electrons from the filled $3d_{5/2}$ core level are excited into the unoccupied states of the 4*f* shell, resulting in a spectrum which is a convolution of those states. Excitations involving the 5*d* states are suppressed. A change of the 4*f* electronic configuration is reflected directly in the shape of the XAS spectrum.

Additionally, the XAS spectra at the M_5 edge of terbium can readily be calculated for different 4*f* occupation as described in Chapter 2.5. Therefore, any changes observed in the XAS signal caused by alterations in the 4*f* electronic system should be describable by simulations based on superpositions of these calculated spectra.

4.1.1 Terbium M_5 edge tr-XAS

The experimental setup is described in Chapter 3.1.1, while details on the sample used can be found in Chapter 3.3.1.

Figure 4.1 a shows the X-ray absorption $A = -\ln(I/I_0)$ recorded at the M_5 edge of terbium, taken at the SCS beamline at EuXFEL. The spectrum

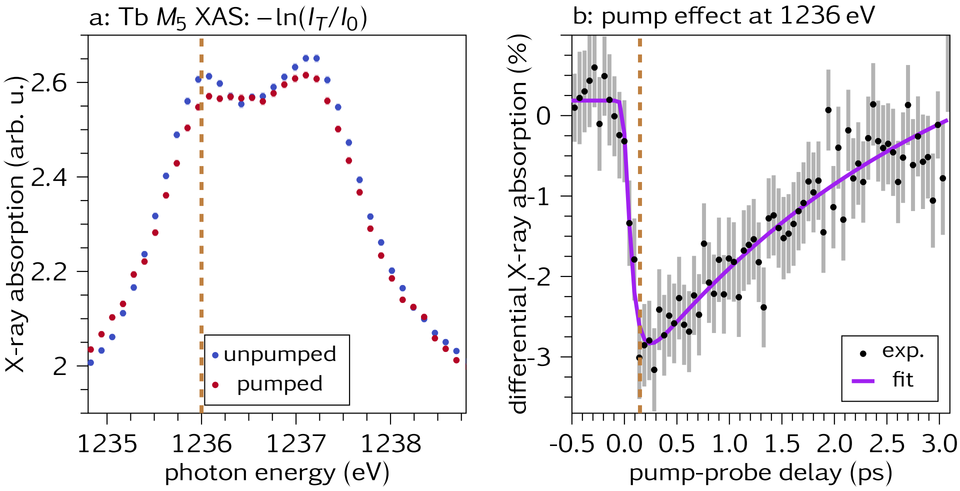

Figure 4.1: a: X-ray absorption spectrum of the terbium M_5 edge recorded at the SCS beamline at EuXFEL. The blue dots represent the data measured for the unpumped sample, the red dots show the spectrum for a pump-probe delay of 150 fs. The brown dashed line marks the energy at which the time trace shown in b was measured. Both dominant features at 1236 and 1237.4 eV show a reduced absorption upon pumping.
b: The differential X-ray absorption for 1236 eV (black dots) drops around 3% in the first 150 fs. The purple line is a double exponential fit to the differential X-ray absorption. The time constant for the decay of intensity is $\tau_1 = (70 \pm 30)$ fs and $\tau_2 = (3.0 \pm 1.6)$ ps for the recovery. The brown dashed line marks the delay at which the spectrum shown in a was measured. The displayed error bars stem from Gaußian error propagation of the standard deviation $\pm\sigma$.

marked by the blue dots (unpumped) was recorded without pump laser and the red dots (pumped) show the spectrum 150 fs after excitation. The spectrum for the unpumped sample exhibits two distinguishable features at 1236 and 1237.4 eV. After pumping, the spectrum shows a clear reduction of intensity at both these features. This indicates changes of the 4f electronic configuration in the probed volume.

Figure 4.1 b shows the temporal evolution of the pump-effect at an energy of 1236 eV (indicated by the brown dashed line in Fig. 4.1 a). The black dots in Fig. 4.1 b describe the differential X-ray absorption calculated by the normalized difference between the spectra for the unpumped and pumped sample:

$$P = 100 \cdot \frac{I_p - I_u}{I_u},$$

where I_u is the unpumped signal and I_p is the pumped signal. The X-ray absorption is reduced by about 3 % within the first 150 fs and recovers over the following 3 ps.
The shape of the temporal evolution can be fitted by a double exponential function (see Appendix A.2) and is shown as purple line in Fig. 4.1 b. The time constant for the exponential decay is $\tau_1 = (70 \pm 30)$ fs and $\tau_2 = (3.0 \pm 1.6)$ ps for the recovery. These timescales resemble those observed for the temperature evolution of the valence electronic system after IR-laser excitation [3].
This already indicates that the alterations in the $4f$ electronic state observed in the M_5-edge XAS originates from direct interaction between $5d$ and $4f$ electrons.

Ground state simulations

Having these indications for excitations of higher $4f$ multiplets, it is attempted to simulate the experimental data using atomistic calculated spectra (see Chapter 2.5).
The first step is to fit the spectrum for the ground state $4f^8\ {}^7F_6$, described by atomistic calculation, to the unpumped spectrum in Fig. 4.1 a. As the calculations give the imaginary part of the scattering amplitude $\mathfrak{Im}[f]_{GS}$ on an arbitrary shifted energy scale e, an energy offset a is introduced:

$$E(a) = e + a.$$

To account for the limited energy resolution of the experiment and the core-hole lifetime broadening, $\mathfrak{Im}[f]_{GS}(E)$ is convoluted with a Gaussian function. Dividing this by the wavelength λ results in the absorption coefficient:

$$\mu_{GS}(E) = 4\pi(\mathfrak{Im}[f]_{GS}(E) * \text{Gauss}(\Delta E))/\lambda.$$

With this, the X-ray absorption signal can be calculated as:

$$XAS_{GS} = I_0 e^{-\mu_{GS}(E)d + \text{edge jump}} + C, \tag{4.1}$$

where I_0 is the incoming intensity, C is an offset and d denotes the sample thickness. The edge jump is approximated by a Heaviside function $\Theta(E_B)$ at the binding energy E_B, scaled by a factor I_{ej} and core-hole life time broadened by convolution with a Gaussian function:

$$\text{edge jump} = I_{ej}\Theta(E_B) * \text{Gauss}(\Delta E_{\text{lifetime}}).$$

The incoming intensity I_0 was measured in the experiment and can be used to normalize XAS_{GS}, yielding the X-ray absorption A:

$$A = -\ln(XAS_{GS}/I_0) = \mu_{GS}(E)d + \text{edge jump} + C'. \tag{4.2}$$

The fit based on Equation 4.2 to the unpumped experimental data is shown in Fig. 4.2. While fit 1 uses the whole energy range as fitting area, fit 2 is limited to a range from 1234.8 to 1238.8 eV. Both fits have difficulties fitting the unpumped spectra offside the resonance. However, close to the resonance, where the pump effect is observed, fit 2 simulates the experimental data much better. Thus, to concentrate on the interesting features at the resonance, the fitting area is limited for all further analysis to the area between 1234.8 and 1238.8 eV. The fit parameters for fit 2 are shown in Tab. 4.1.

Table 4.1: Fit parameters used for fitting the unpumped spectrum.

a	(1247.25 ± 0.01) eV	C	1.767 ± 0.006
d	$(1.14 \pm 0.01) \times 10^{-10}$ m	ΔE	(0.41 ± 0.01) eV
E_B	(1237.707 ± 0.001) eV	I_{ej}	0.085 ± 0.005
$\Delta E_{\text{lifetime}}$	(0.20 ± 0.01) eV		

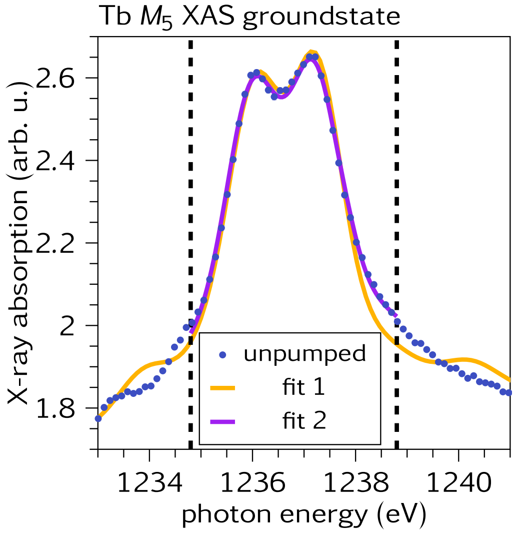

Figure 4.2: Comparison between two different fits to the unpumped spectrum of terbium. Fit 1 uses the whole energy range as fitting area while fit 2 is limited to the range between 1234.8 to 1238.8 eV. Fit 2 simulates the features around the resonance better, hence this will be the basis for further analysis.

Excited state simulations

The experiment- and sample-specific parameters will not vary upon pumping and can be used to simulate the XAS spectrum from the pump-laser excited sample, which is assumed to contain contributions from energetically higher $4f$ multiplets. The absorption coefficient for the pumped spectrum can thus be written as:

$$\mu_{exc} = \left(1 - \sum_{\mathrm{i}} c_{\mathrm{i}}\right)\mu_{GS} + \sum_{\mathrm{i}} c_{\mathrm{i}}\mu_{\mathrm{i}},$$

where i is the excited $4f$ state, μ_{i} the respective absorption coefficient and c_{i} the relative contribution of μ_{i} to the total absorption coefficient.
Analogue to the ground state spectrum, broadening is included in the absorption coefficient and the X-ray absorption for the pumped sample becomes:

$$A = \mu_{exc}(E)d + \text{edge jump} + C, \tag{4.3}$$

with the same parameters as used for the ground state spectrum (see Tab. 4.1). Combining Equations 4.2 and 4.3 yields the differential X-ray absorption for the simulated data:

$$P = 100 \cdot \frac{A_{exc} - A_{GS}}{A_{GS}}.$$

In order to identify the admixture of possible higher multiplets, it proved feasible to fit the differential X-ray absorption spectrum (Fig. 4.3 a, black dots).
In the first step only the energetically lowest excitation out of the ground state into the $4f^8\ {}^7F_5$ multiplet is considered. Hence the only fitting parameter is c_1. The best match between simulation and experiment is obtained for an admixture of (17 ± 2) % of the ${}^7F_5$ multiplet and (83 ± 2) % of the ground state multiplet ${}^7F_6$.
The fit result is shown in Fig. 4.3 a as purple curve. In comparison with the experimental data, the overall trend is described very well; peaks and dips are displayed at the right energy positions and the feature around 1236 eV is more pronounced compared to the one at 1237.4 eV. However, it appears that, for a quantitative description of the relative intensities, additional multiplet components are still missing.
Figure 4.3 b depicts the simulation of the X-ray absorption based on the fit result.

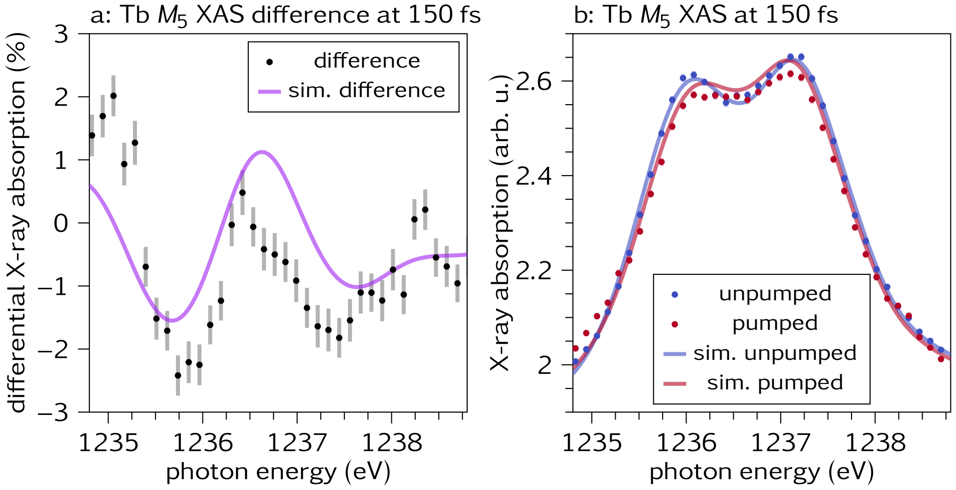

Figure 4.3: a: Differential X-ray absorption at the terbium M_5 edge at a pump-probe delay of 150 ps (black dots). The purple line denotes the simulation involving solely admixtures of the $4f^8\ {}^7F_5$ multiplet, the energetically lowest excited state above the ground state $4f^8\ {}^7F_6$. The best agreement between simulation and data is found for a contribution of $(17 \pm 2)\,\%\ {}^7F_5$ and $(83 \pm 2)\,\%$ of ${}^7F_6$.
b: X-ray absorption spectra for the pumped (red dots) and unpumped (blue dots) sample. The lines depict the simulated spectra based on the ground state multiplet ${}^7F_6$ (blue line) and with admixture from the ${}^7F_5$ multiplet (red line).

Inelastic 5*d*-4*f* electron-electron scattering

The temporal evolution of the overall spectral changes indicates direct 5*d*-4*f* interaction as trigger of the ${}^7F_6 \rightarrow {}^7F_5$ transition.
In order to identify a concrete microscopic process responsible for the observed excitation, the following assumptions must be fulfilled.

- An energy transfer from the 5*d* to the 4*f* system of 0.28 eV is required to excite the energetically lowest multiplet ${}^7F_5$ above the ground state multiplet ${}^7F_6$.
- Exciting higher 4*f* multiplets reduces the total 4*f* angular momentum *J*. Thus, transfer of angular momentum out of the 4*f* system must be included.
- Because the 4*f* system reacts and recovers on similar timescales as the 5*d* electronic temperature, a scattering rate proportional to the amount of excited 5*d* electrons must be assumed.

These assumptions can be met by inelastic scattering via screened Coulomb interaction between 5d and 4f electrons. The transferred angular momentum could stem from a 5d spin-flip, changing the 5d spin by $\Delta S = 1$.

Figure 4.4 explains the electronic excitations involved in the pump probe experiment in a total energy scheme. Upon pumping with the 800 nm laser, the 5d6s electrons are excited from the initial ground state $3d^{10}4f^{8}(5d6s)^{3}$, in which the 4f electrons populate the $^7F_6$ multiplet. The excitation in the valence system elevates the energy level of the full electronic configuration (Fig. 4.4 left, red line). Within 100 – 200 fs the 5d6s system thermalizes via electron-electron scattering [3], forming a hot Fermi distribution (Fig. 4.4 middle, red area). Now, a 5d electron with sufficient energy can relax into an empty state, while scattering with an 4f electron, indicated by the Feynman diagram in Fig. 4.4. Upon transfer of energy of 0.28 eV and angular momentum of $\Delta J = -1$ to the 4f system via screened Coulomb interaction, the 4f system is excited from the $^7F_6$ ground state to the $^7F_5$ configuration. Considering the energy needed to reach the first excited 4f state $^7F_5$ of $\Delta E = 0.28\,\text{eV}$, only 5$d$ electrons that can distribute at least this energy may contribute. As a consequence of the 4f electronic excitation, the initial state in the probe process is altered, directly impacting the $3d \rightarrow 4f$ transition probability and hence the M_5 edge XAS spectrum.

Multiple scattering events, *i.e.* scattering involving already excited 4f states, could successively transfer angular momentum via 5d spin-flips, resulting in $\Delta J > 1$ and occupation of energetically higher lying ^7F_J multiplets with $J = 4, 3, 2, 1, 0$. Because of the direct interaction with the hot 5d system, it can be assumed, that 5d and 4f electronic system equilibrate on ultrafast timescales, populating the 4f multiplets according to a Boltzmann distribution.

About the implications of 5d-4f scattering for ultrafast magnetization dynamics in 4f metals can only be speculated at this point. Multiple scattering events and possible 5d-4f thermalization could directly contribute to ultrafast demagnetization via occupation of different m_J levels within the excited multiplets as well as redistribution of angular momentum from the 4f electronic system into the lattice via the 5d electrons.

Additionally, changing the 4f state should directly influence the 4f-spin-lattice coupling, an important channel for magnetic dynamics of rare earth metals [2, 16]. Hence, 4f excitations need to be taken into account for a full description of the demagnetization process.

D. Legut, K. Carva and P. M. Oppeneer performed DFT calculations to de-

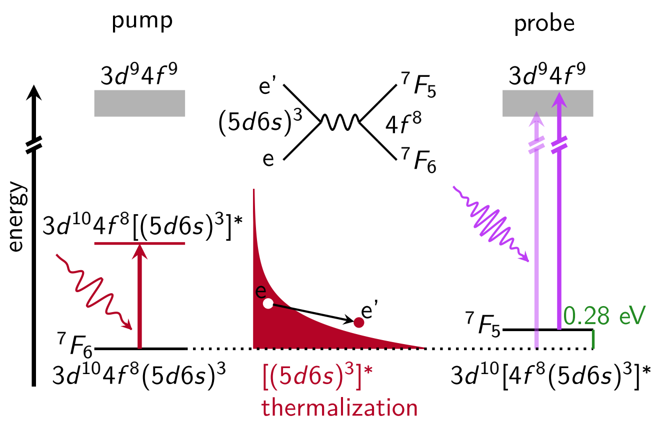

Figure 4.4: The pump pulse of 800 nm is absorbed by the $(5d6s)^3$ valence electrons, elevating those electrons to an excited state $[(5d6s)^3]^*$ (left part). Within 100 – 200 fs those excited electrons thermalize and form a hot Fermi distribution (middle part). A hot valence electron can scatter with an $4f$ electron (Feynman diagram), transferring energy and angular momentum to the $4f$ system and occupying an empty state at lower energy. Thus, a portion of all probed $4f$ atoms will be in an excited state, *e.g.* $^7F_5$. The $4f$ excitation alters the initial state in the M_5 edge X-ray absorption, directly affecting the measured spectral shape (right part). Probing a collection of partially excited atoms results in a measured spectrum which can be described as an admixture of spectra for different $4f\ ^7F_J$ configurations.

termine the MCA for different terbium $4f$ states. Regarding the magnetic terbium ground state with $m_l = 3$ the *ab initio* calculations provide an MCA of 15 meV per atom with an easy axis in the hcp basal plane along the crystallographic a axis. This is well in accordance with experiment [10]. For the excited $^7F_5$ state the minority terbium $4f$ electron occupation was considered to mainly involve the $m_l = 2$ configuration and a one-step calculation of the total energies was performed. This leads to a reorientation of the easy axis to the c axis perpendicular to the basal plane. Such a rotation from in-plane to out-of-plane corresponds to a MCA sign change. This was further verified by creating a self-consistent state with dominant $m_l = 2$ occupation by modifying the Coulomb repulsion between $4f$ electrons (adjustment of Hubbard U), which also causes the MCA sign to change.

These calculations show that the MCA of terbium can be strongly influenced via specific $4f^8$ multiplet excitations. Thus, an understanding and control of the $5d$-$4f$ scattering process might enable transient manipulation of the MCA, a crucial aspect for the development of *e.g.* future magnetic storage devices.

4.1.2 Cross-check in Gadolinium

To ensure that all pump-induced changes to the terbium XAS spectrum stem from 4*f* electronic excitations, a reference measurement on gadolinium was done.
In gadolinium, the energetically lowest excitation out of the $^8S_{7/2}$ ground state is a transition into the spin-changed $^6P_{7/2}$ multiplet [82], which requires 4.1 eV, considerably exceeding the 1.55 eV pump energy and therefore assumed to be suppressed.
The unpumped spectrum and a spectrum integrated over the first 200 fs after pump excitation is shown in Fig. 4.5 a. The integration over 200 fs pump-probe delay was done for better statistics. No pump effect can be found at the gadolinium M_5 edge. This is visualized even better by the differential X-ray absorption shown in Fig. 4.5 b.
Therefore, the spectral alteration observed in terbium can be safely attributed to electronic excitation in the 4*f* system.

4.1.3 Summary

The investigation of time-resolved spectral changes in M_5 edge XAS for terbium metal and corresponding simulation within an atomistic framework revealed inelastic 5*d*-4*f* electron-electron scattering to excite 4*f* multiplets out of the electronic ground state configuration.
The involved transfer of energy and angular momentum between 5*d* and 4*f* system as well as a concomitant alteration of the 4*f*-spin-lattice coupling must be considered in the discussion on angular momentum flow and ultrafast magnetization dynamics in 4*f* rare-earth metals.

4.2 RIXS at FLASH

Complementary to the XAS measurements, a time-resolved RIXS experiment was carried out on a 40 nm terbium layer (see Chapter 3.3.2) at the PG1 Raman beamline of FLASH at DESY in Hamburg, Germany (see Chapter 3.2.1). With RIXS as selective probe of specific multiplet excitations, the population of the $^7F_5$ state after optical pumping could be unequivocally proven.

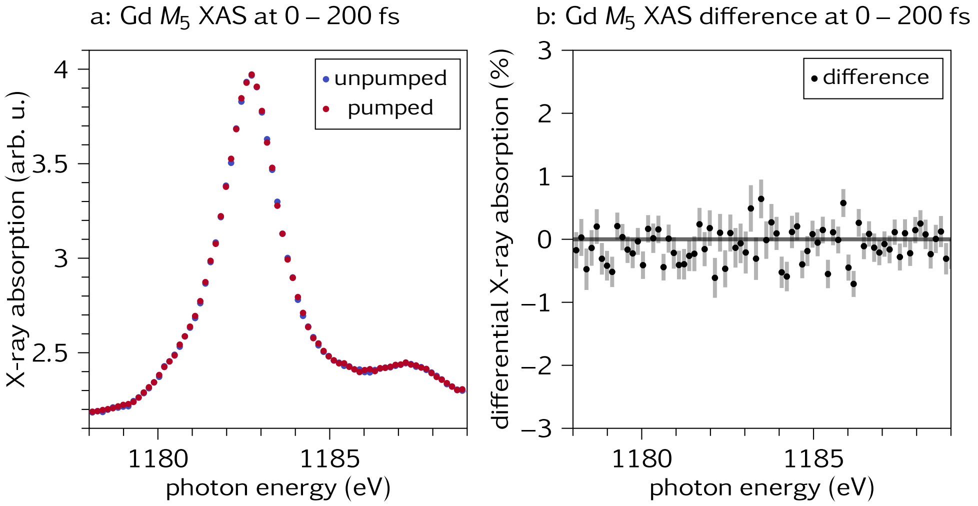

Figure 4.5: a: XAS measured at the gadolinium M_5 edge. The spectrum for the pumped sample is integrated for a pump probe delay from 0 – 200 fs for better statistics.
b: Corresponding differential X-ray absorption. No pump effect is observed.

4.2.1 Terbium $N_{5,4}$ edge tr-RIXS

In a first step a static RIXS map over an excitation energy range from 147.0 to 152.5 eV around the terbium $N_{5,4}$ edge and a loss energy range from −1 to 5.5 eV was recorded (see map in Fig. 4.6 a and the separated graphs used to create it in Fig. 4.6 b). In addition to the strong elastic feature at 0 eV loss energy, several features at loss energies above 2.5 eV are visible. This static RIXS map is used to calibrate the energy axis for atomic calculations depicted in Fig. 4.6 c as RIXS map and in Fig. 4.6 d as spectra integrated over the energy ranges marked by the colored lines in Fig. 4.6 c. The RIXS lines observed in the static experiment can be reproduced by the calculations for the $^7F_6$ ground state (solid lines in Fig. 4.6 d) in the same energy regions. Remaining discrepancies in intensity stem from the very high sensitivity of spectral weight to the excitation energy and different broadening of the experimental and theoretical spectra. While the calculated spectra exhibit constant broadening over the whole energy range, the experimental data include slightly discontinuous broadening. The latter result from stitching of spectra recorded at three energy loss foci (0, 2.5 and 4 eV), beyond which energy resolution declines. In addition to spectra for the $^7F_6$ ground state also the spectra for the excited state $^7F_5$ were calculated and are shown as dashed lines in Fig. 4.6 d. Especially

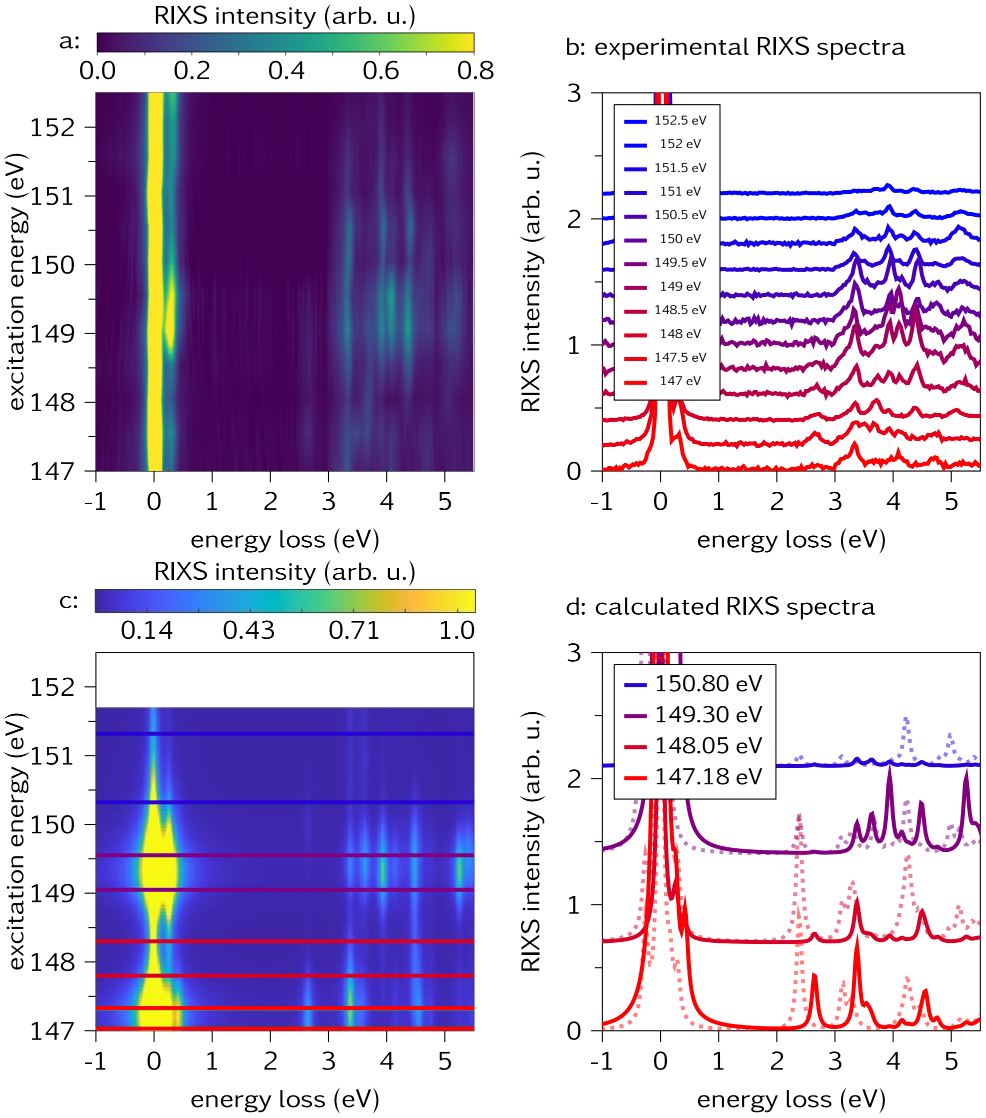

Figure 4.6: a: Static RIXS map of terbium recorded around the terbium $N_{5,4}$ edge. Besides the strong elastic line at zero energy loss also features at higher energy loss between 2.5 and 5.5 eV are visible.
b: Experimental RIXS spectra which were used to create the map in a.
c: RIXS map predicted by atomistic calculations.
d: Calculated RIXS spectra. The solid lines represent spectra for the $^7F_6$ ground state, the dashed lines for the $^7F_5$ configuration.

in the region of 147 – 148 eV excitation energy pronounced differences at 2 – 3 eV energy loss between the $^7F_6$ and $^7F_5$ RIXS spectra appear. In principle the excited state spectrum involves all RIXS lines, which are also present in the ground state spectrum, however with varied spectral weight and shifted to lower energy loss by the very same energy, which is needed to excite the higher multiplet. This connection is exemplary sketched in Fig. 4.7 in the case for the decay into the $^5D_4$ multiplet. Photons of about 2.6 eV energy loss are emitted for excitations from the initial state $^7F_6$ (light green and light blue arrows). With the excited multiplet $^7F_5$ as initial state and the same excitation energy (dark blue arrow), the energy of the emitted photons will be increased (dark green arrow) resulting in reduced energy loss and a shift of spectral features.

In the RIXS experiment the same effect was observed after pumping the terbium sample with 1.2 eV-laser pulses. The measured spectra are shown in Fig. 4.8 a. The energy loss covers the region of interest with two prominent features at around 2.6 and 3.4 eV resulting from decay into the $^5D_4$ and $^5G_6$ multiplet. While the blue dots display the spectrum for the unpumped sample, the red dots show the spectrum recorded at a pump-probe delay of 300 fs. In the blue marked area just below 2.5 eV and in the green marked area around 3 eV an increase of scattered intensity can be noticed. At the same time the intensity of the main features is reduced. For better visualization of the pump effect, the differential RIXS signal, *i.e.* the relative change in intensity, is displayed as black dots in Fig. 4.8 b.

Both, the spectra and the respective pump effect can be qualitatively well described by the theoretical RIXS signal at 147.2 eV. Assuming the pure $^7F_6$ state (blue curve) for the unpumped and an admixture of 95 % $^7F_6$ and 5 % $^7F_5$ (red curve) for the pumped case (Fig. 4.8 c), the differential RIXS reproduces the distinct intensity increase at around 260 meV below the two main features very well (Fig. 4.8 b, black line). This energy difference corresponds to the energy difference between the $^7F_6$ and the $^7F_5$ state of 260 meV.

Residuary differences between simulation and experiment might be caused by mismatching excitation energy ranges and energy resolution. Another explanation could be the excitation of higher ^7F_J multiplets, whose contribution is not considered in the simulation. Those would provoke additional shifts of spectral weight towards lower energy loss (marked by the red dashed lines) and, as observed in the differential RIXS signal, an increase of intensity below the theoretically predicted features.

A quantitative evaluation of the contribution of excited multiplets is difficult, because the RIXS cross-section for specific multiplets across the

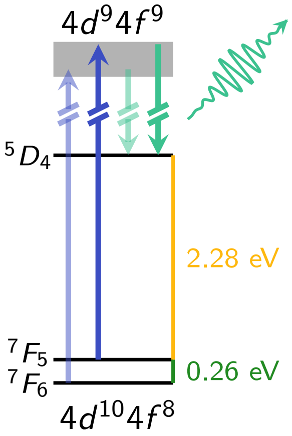

Figure 4.7: Probing the $^7F_5$ configuration with photons of about 147 eV (dark blue and dark green arrows) leads to a different position in total energy compared to probing the $^7F_6$ state (light blue and light green arrows). Hence, relaxation to *e.g.* the $^5D_4$ state results in a reduced energy loss, determined by the energy difference between the $^7F_6$ and $^7F_5$ configuration.

terbium $N_{5,4}$ resonance depends strongly on the incoming photon energy. Consequently, also the admixture of $^7F_5$ excited ions in the probed volume deviates from the theorized 5 %.
The time evolution of the measured pump effect is shown in Fig. 4.8 d as blue dots for the differential RIXS signal integrated over the blue marked area and as green dots for the green marked area, respectively. The time resolution in the RIXS experiment was only around 300 fs, hence larger than the expected rising edge of the pump effect considering the EuXFEL data. In connection with the little number of data points on the rising edge, the time evolution can not be modeled meaningfully. However, when comparing it to the temporal profile found for the pump effect at EuXFEL, the data can be well described (purple curve in Fig. 4.8 d).

4.2.2 Summary

Complementary to the time-resolved terbium M_5 XAS measurements, a terbium $N_{5,4}$ RIXS experiment was performed.
Although a quantitative evaluation of excited multiplet contributions with RIXS is not straightforward, the measurements unequivocally proof the population of the $^7F_5$ multiplet after optical excitation of terbium metal.

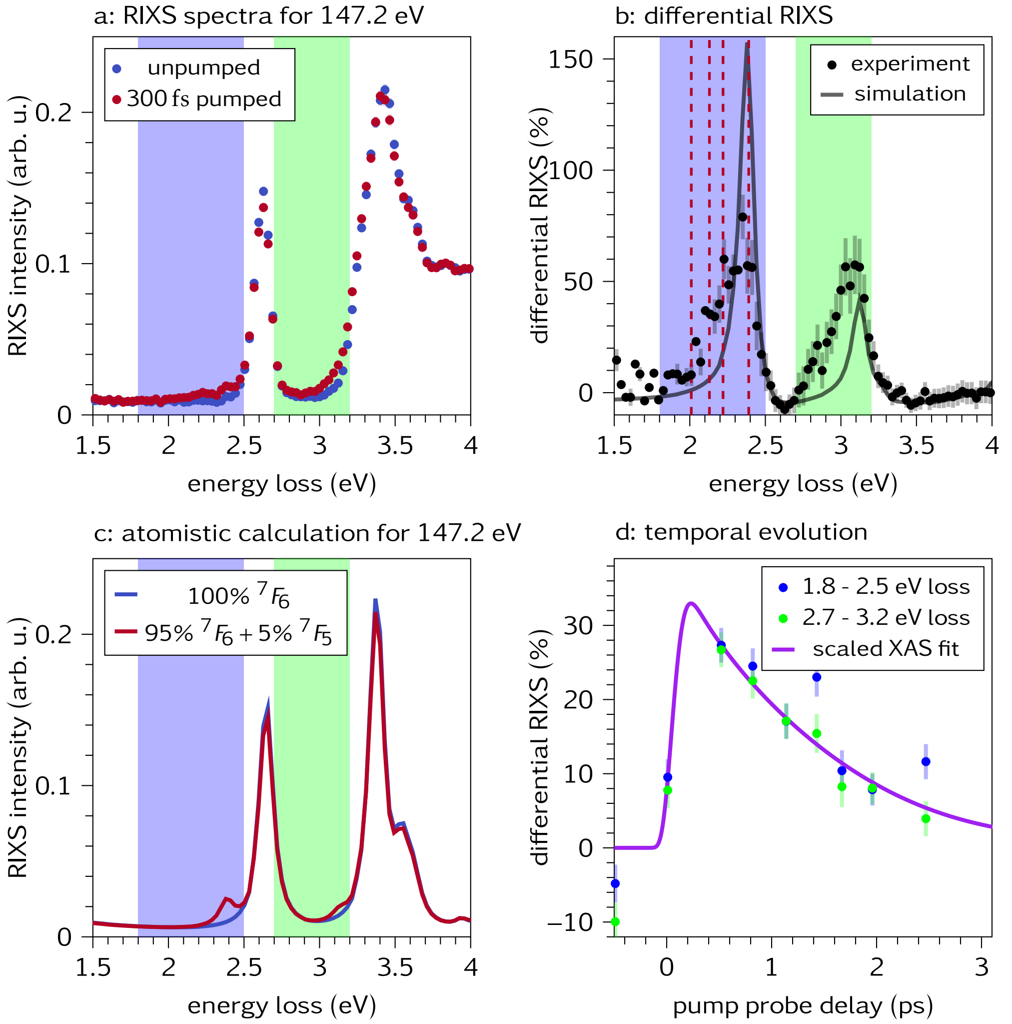

Figure 4.8: a: RIXS spectra for the unpumped sample (blue dots) and 300 fs after pump-pulse arrival (red dots) for 147.2 eV excitation energy and 2.5 eV energy loss focus. Intensity rises in the green marked area around 3 eV and in the blue marked region below 2.5 eV.
b: Comparison between the differential RIXS signal for the experimental data (dots) and the calculations (line). The red dashed lines mark the energy shift of the $^5D_4$ feature for initial excited multiplets.
c: Calculated RIXS spectra for 147.2 eV excitation energy. The blue line depicts calculations for a pure $^7F_6$ configuration. The red line displays an admixture of 95 % $^7F_6$ and 5 % $^7F_5$. These calculations predict a pump effect in the green marked area around 3 eV and in the blue marked area below 2.5 eV.
d: Differential RIXS signal integrated over the in b green marked (green dots) and blue marked (blue dots) pump-probe-delay regions. The temporal profile fits to the time evolution of the change in X-ray absorption measured at EuXFEL (purple line from Fig. 4.1 b).

Further, RIXS appears to be a powerful tool for selectively probing electronic excitations, which become visible as distinct shifts of spectral weight correspondent to the specific multiplet energy level.
The studied RIXS data give indications for higher ^7F_J multiplets populated after optical pumping of terbium metal. Hence, these will be the focus of the following Chapter 4.3.

4.3 Excitation of higher multiplet terms in terbium

The tr-RIXS spectra presented in Chapter 4.2 exhibit signatures of energetically higher lying multiplets ^7F_J with $J = 4, 3, 2, 1, 0$. Further, the temporal evolution of the $4f$ excitations indicates that they are continuously driven by scattering with hot $5d$ electrons.
Assuming that each scattering event causes transfer of energy and angular momentum $\Delta J = 1$ (provided by *e.g.* a $5d$ spin-flip), multiple scattering events involving the very same $4f$ ion will provoke angular momentum transfer $\Delta J > 1$ and consequent population of higher ^7F_J multiplets.
Such interaction will lead to ultrafast thermalization between the $5d$ and $4f$ electronic systems and establish a Boltzmann occupation of the $4f$ multiplets.
In this chapter a simulation of the experimental XAS data by a Boltzmann-distributed occupation of the $4f$ multiplets is attempted. Afterwards, the deposited energy by the pump laser pulse is estimated and a two-temperature model involving $5d$ electrons and lattice is discussed. Finally, a three-temperature model including a separate temperature for the $4f$ system is introduced.

4.3.1 Boltzmann-distributed simulation

The simulation of XAS spectra, involving energetically higher lying $4f^8$ states, is based on a temperature-dependent probability for populating ^7F_J multiplets according to a Boltzmann distribution with a relative contribution $c_\mathrm{i} = g_\mathrm{i} \cdot e^{-E_\mathrm{i}/(k_B T)}$. While the temperature T is the fitting parameter, E_i corresponds to the excitation energy of the first six inner shell excitations (see Tab. 2.1) and $g_\mathrm{i} = 2J + 1$ is the corresponding degeneracy. The best fit is achieved for a $(2038 \pm 83)\,\mathrm{K}$ Boltzmann distribution and is shown in

Fig. 4.9. The overall matching to the experimental data is qualitatively good and improved in contrast to the first attempt, which only considered contribution of the ${}^7F_5$ multiplet. Still, it overestimates the pump effect between the two main features at around 1236.5 eV and undervalues the one in the region of the first peek at 1235.8 eV. Possibly additional excited multiplets are involved. This will be further discussed in Chapter 4.3.5, which focuses on contributions from $5d$-$4f$ charge transfer.

The admixtures of states corresponding to $(2038 \pm 83)\,\mathrm{K}$ is shown in Tab. 4.2. About 22 % of all probed atoms are in an excited state at this temperature. How can this temperature be understood? 2000 K is well above the melting point of terbium metal. In the case of non-equilibrium, the temperature of the different microscopic subsystem need to be considered. To do so, the two-temperature model involving $5d$ electrons and the lattice will be introduced in the following. On that basis, the model will be extended by including the $4f$ electronic system. Finally, the temporal evolution of the pump effect observed in XAS will be discussed in view of the three temperatures involved.

4.3.2 Absorbed laser power

For further analysis of the sample temperature, an estimation of the amount of energy deposited by the pump-laser pulse is needed.

During the experiment at the EuXFEL the laser-beam power as well as the spot size were measured. By dividing the measured laser-beam power $P \approx (56 \pm 11)\,\mathrm{mW}$ by the laser-spot size $A = (0.028 \times 0.02)\,\mathrm{cm}^2$ and the repetition rate $f = 10\,\mathrm{kHz}$, an incident pump fluence of $(10 \pm 2)\,\mathrm{mJ\,cm}^{-2}$ per pulse can be calculated. Now, the absorbed laser power in the terbium layer during the experiment can be estimated.

For a first, very rough estimation, the Lambert Beer law can be used directly

Table 4.2: Admixture of states corresponding to a $(2038 \pm 83)\,\mathrm{K}$ Boltzmann distribution.

T	${}^7F_6$	${}^7F_5$	${}^7F_4$	${}^7F_3$	${}^7F_2$	${}^7F_1$	${}^7F_0$	$\sum {}^7F_{J<6}$
1955	79.4 %	12.8 %	4.9 %	1.8 %	0.8 %	0.3 %	0.1 %	21.6 %
2038	78.0 %	13.4 %	5.2 %	2.0 %	0.9 %	0.4 %	0.1 %	22.0 %
2121	76.6 %	14.0 %	5.7 %	2.3 %	1.0 %	0.4 %	0.1 %	23.4 %

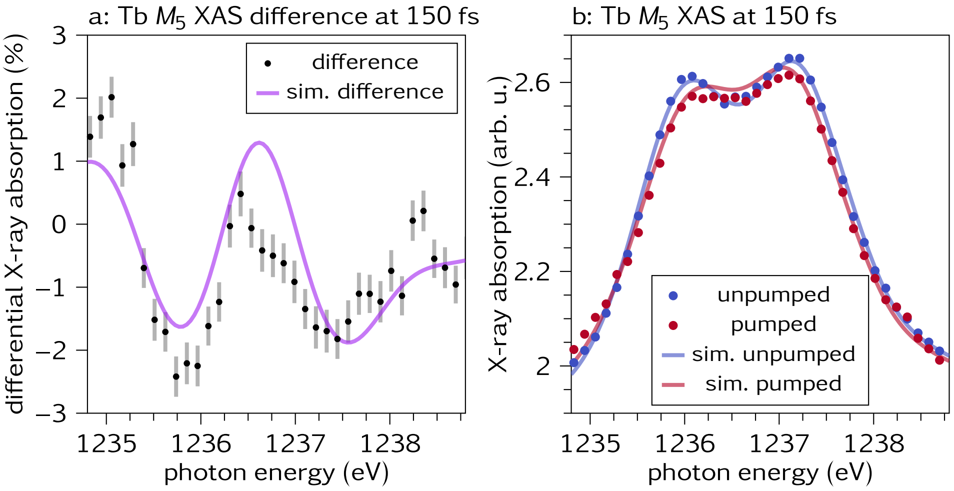

Figure 4.9: a: Simulation of the differential X-ray absorption at 150 fs pump-probe delay. The displayed fit is obtained for a (2038 ± 83) K Boltzmann distribution of excited $4f^8$ states.
b: Simulated XAS spectra for the pumped and unpumped sample.

to calculate the transmitted intensity of a layer system:

$$\Delta I = \frac{I}{I_0} = e^{-\mu(E)\cdot d} = e^{-4\pi\cdot\frac{k}{\lambda}\cdot d} = e^{-4\pi\cdot\frac{\sum_{\mathrm{i}} k_{\mathrm{i}}\cdot d_{\mathrm{i}}}{\lambda}}, \tag{4.4}$$

with I_0 as the incoming intensity of light at wavelength λ, k_{i} as the imaginary part of the refractive index for layer i and d_{i} as the thickness of layer i. The absorption can be estimated as $A = 1 - \Delta I$. To evaluate the absorption of a specific layer x, the respective incoming fluence needs to be considered reduced by the layers before layer x:

$$A_{\mathrm{x}} = 1 - e^{-4\pi\cdot\frac{\sum_{\mathrm{i=0}}^{\mathrm{x}} k_{\mathrm{i}}\cdot d_{\mathrm{i}}}{\lambda}} - (1 - e^{-4\pi\cdot\frac{\sum_{\mathrm{i=0}}^{\mathrm{x-1}} k_{\mathrm{i}}\cdot d_{\mathrm{i}}}{\lambda}}) = e^{-4\pi\cdot\frac{\sum_{\mathrm{i=0}}^{\mathrm{x-1}} k_{\mathrm{i}}\cdot d_{\mathrm{i}}}{\lambda}}(1 - e^{-4\pi\cdot\frac{k_{\mathrm{x}}\cdot d_{\mathrm{x}}}{\lambda}}). \tag{4.5}$$

Regarding the given sample layout, only the yttrium capping layer and the terbium sample layer need to be taken into account. Hence, for λ =(800 ± 10) nm, an yttrium layer thickness of d_Y = (2.0 ± 0.5) nm, a terbium layer thickness of d_{Tb} = (10 ± 2) nm and the optical constants for yttrium (n=2.10, k=2.67) and terbium (n=2.36, k=3.21) [83], Equation 4.5 results in A_{Tb} = (37 ± 1) % with respect to the total incoming fluence.
However, this approach vastly overestimates the absorbed laser power, due to the disregarded reflection at the layer interfaces. Additionally, in the case of normal incidence, the incoming and reflected beam are spatial

overlapping and interference occurs. This modulates the effective electric field of the light and thus also influences the absorption. This becomes especially complicated when multiple reflections in a stack of different layers are taken into account. David Windt created the simulation program IMD [84], which uses a recursive approach to address these problems. For this thesis, IMD was used in conjunction with the XOP (X-ray oriented programs) driver software [85, 86].

Using IMD, the absorption and reflection for an idealized sample can be calculated. Simulation for a stack of 2 nm Y | 10 nm Tb | 20 nm Y | 300 nm Al | 100 nm Si_3N_4, a wavelength of 800 nm in normal incidence and the same optical constants for yttrium and terbium as used above, result in a total absorption of $A = 33.24\,\%$ and a total reflection of $R = 66.75\,\%$. In addition, IMD provides the intensity profile $I(z)$. To calculate the amount of laser power absorbed only in the terbium layer, the intensity profile $I(z)$ is integrated over the terbium layer and then divided by the integral over the whole sample. About 48.6 % of the total absorbed laser power is deposited in the terbium layer. Multiplying this with the total absorption of the sample, leads to $A_{Tb} = 15.6\,\%$ absorption with respect to the total incoming fluence.

The assumption of an idealized sample can be easily disproved, though. By measuring the reflectivity of the sample under nearly normal incidence for 800 nm wavelength in a lab based experiment, the total reflection of the sample was found to be $R = (49.8 \pm 0.8)\,\%$. This discrepancy between the real sample and the idealized conditions may stem from various reasons, including slightly different layer thicknesses, sample contamination like an oxidized aluminum surface layer or interface roughness due to stress induced by the SiN substrate due to lattice mismatching.

As a reduction in reflectivity coincides with an increased absorption, also the amount of laser power absorbed in the terbium layer must be higher. Assuming the same intensity profile as for the idealized sample, A_{Tb} needs to be corrected to $(23.5 \pm 0.4)\,\%$ of the incoming fluence in case of taking a total absorption of $A = 1 - R = (50.2 \pm 0.8)\,\%$ in the sample into account. Overall, it is estimated that about 15.6 – 23.9 % of the laser power is absorbed in the terbium layer. Regarding the incident pump fluence of $(10 \pm 2)\,\mathrm{mJ\,cm^{-2}}$ this corresponds to a total absorbed energy density of $E_{abs,Tb} = (1.6 \pm 0.6)$ to $(2.4 \pm 1.0)\,\mathrm{kJ\,cm^{-3}}$ for a (10 ± 2) nm thick terbium layer. The lab based measurement of the reflectivity of the sample shows that a higher total absorbed energy density is more likely.

4.3.3 Two-temperature model

After excitation of a metal with near-infrared laser pulses, the 1.55 eV photons interact with the valence electrons. In the case of terbium metal the laser power is predominantly absorbed by the 5*d*6*s* valence electrons (see Chapter 3.1). The excitation leads to an increase in temperature of the valence electronic system on femtosecond timescales. Equilibration within the electronic system is assumed to set in after tens of femtoseconds [3]. The lattice heats up on slightly slower timescales via electron-phonon interaction until electronic and lattice system have equilibrated (typically on timescales of about two picoseconds [3]). This process can be captured by considering the temperature in two separated systems: the electronic system and the phonon bath. The temperature evolution can be described by the so called *two-temperature model* (2TM) [87, 88, 89]. In this model, the electrons and the lattice are treated as coupled but separated systems with their own temperature T_{el} and T_{ph}. In both systems energy can be stored. To model the temporal evolution of T_{el} and T_{ph}, the energy exchange between and in the systems needs to be considered. In case that only heat can be exchanged between the systems, a model can be formulated, that couples the two temperatures via a certain coupling parameter and the difference between the temperatures. In addition, the model should include transport of heat along the sample normal via the valence electrons. This assumption presumes a homogeneously pumped sample area, which is much larger than the probed area. Otherwise heat transport vertically to the sample normal must be taken into account. In the model introduced here, the transport is only realized in the valence electron system. Transport of energy in the phonon system is expected to only play a role on larger timescales [90]. Implementing such a transport in the phonon system might improve the model in future iterations, but is neglected for now.

With the energy initially deposited by a laser pulse only into the electronic system, the 2TM describes the coupled electronic and phonon system via two coupled differential equations:

$$\frac{\mathrm{d}E_{el}}{\mathrm{d}t} = \frac{\mathrm{d}(C_{el}\mathrm{d}T_{el})}{\mathrm{d}t} = -g_{ep}(T_{el} - T_{ph}) + \nabla \cdot (\kappa_{el} \nabla T_{el}) + P_{laser}(t, z),$$

$$\frac{\mathrm{d}E_{ph}}{\mathrm{d}t} = \frac{\mathrm{d}(C_{ph}\mathrm{d}T_{ph})}{\mathrm{d}t} = +g_{ep}(T_{el} - T_{ph}).$$

The specific heat C is indirectly dependent on the time via the temperature and hence must be included in the time derivative. It can be written as

$$\frac{\mathrm{d}(C\mathrm{d}T)}{\mathrm{d}t} = \frac{\mathrm{d}C}{\mathrm{d}t}\mathrm{d}T + C\frac{\mathrm{d}T}{\mathrm{d}t} = \frac{\mathrm{d}C}{\mathrm{d}T}\frac{\mathrm{d}T}{\mathrm{d}t}\mathrm{d}T + C\frac{\mathrm{d}T}{\mathrm{d}t} = \left(\frac{\mathrm{d}C}{\mathrm{d}T}\mathrm{d}T + C\right)\frac{\mathrm{d}T}{\mathrm{d}t} = (C+\mathrm{d}C)\frac{\mathrm{d}T}{\mathrm{d}t}.$$

The term $\mathrm{d}C$ can be made insignificantly small, when the time steps are made very small. Hence to simplify the model, this term will be ignored. Thus the differential equations for the temperature evolution are:

$$\frac{\mathrm{d}T_{el}}{\mathrm{d}t} = \frac{-g_{ep}(T_{el} - T_{ph}) + \nabla\cdot(\kappa_{el}\nabla T_{el}) + P_{laser}(t,z)}{C_{el}},$$

$$\frac{\mathrm{d}T_{ph}}{\mathrm{d}t} = \frac{+g_{ep}(T_{el} - T_{ph})}{C_{ph}},$$

where C_{el} and C_{ph} are the specific heat for electrons and phonons, respectively. Coupling between the electron temperature T_{el} and the phonon temperature T_{ph} is realized via electron-phonon coupling, defined by the electron-phonon coupling strength g_{ep}. κ_{el} is the thermal conductivity. Transport of energy is implemented via the term $\nabla\cdot(\kappa_{el}\nabla T_{el})$.
The absorbed laser power density by the electron system $P_{laser}(t,z)$ can be written as

$$P_{laser}(t,z) = \frac{A\cdot F_0}{d}\frac{e^{\frac{-t^2}{2\tau^2}}}{\sqrt{2\pi\tau}}e^{-\mu_{opt}z},$$

with F_0 as incidence fluence, d as layer thickness and A as absorption. The laser duration τ was set to 85 fs, stemming from cross-correlation of the pump-pulse duration with a Gaußian with a full width at half maximum of 200 fs, accounting for internal thermalization of the valence electrons via electron-electron scattering. Normally the attenuation length of the laser μ can be calculated as $\mu = \frac{4\pi\cdot k}{\lambda} = \frac{4\pi\cdot 3.27}{800\,\mathrm{nm}} \approx \frac{1}{20\,\mathrm{nm}}$. However, experiments have shown, that the attenuation length is seemingly increased by ballistic electron excitation in rare-earth metals [11]. Accounting for this extension, an effective attenuation length of $\mu = \frac{1}{40\,\mathrm{nm}}$ was estimated.
The electronic specific heat for a thin terbium film can be written as $C_{el} = \gamma_{el}T_{el}$ with $\gamma_{el} = 2.25\times10^2\,\mathrm{J/(m^3K^2)}$ [91]. To describe the phonon specific heat, the Einstein model [92] was used:

$$C_{ph} = C_{ph}^{\infty}\left(\frac{T_E}{T_{ph}}\right)^2 \frac{e^{T_E/T_{ph}}}{(e^{T_E/T_{ph}} - 1)^2}, \tag{4.6}$$

where T_E, the Einstein temperature, was set to $T_E = 0.75 \cdot T_D$, with the Debye temperature for terbium $T_D = 174\,\mathrm{K}$ [91]. C_{ph}^{∞} is $2.2 \times 10^6\,\mathrm{J/(m^3K)}$ [93]. The electron-phonon coupling $g_{ep} = 2.5 \times 10^{17}\,\mathrm{J/(sm^3K)}$ was taken from [3, 4]. The thermal conductivity κ_{el} is temperature-dependent. According to [90], it increases for higher transient electron temperature: $\kappa_{el} = \kappa_0 T_{el}/T_{ph}$, where $\kappa_0 \approx 16\,\mathrm{W/(mK)}$ [94]. The initial temperature was estimated as $T_0 = 300\,\mathrm{K}$. The calculations were done for an absorbed energy density $E_{abs} = \frac{A \cdot F_0}{d} = 3.2\,\mathrm{kJ\,cm^{-3}}$. The described model was implemented in Python with the respective code shown in Appendix A.3.

The result is displayed in Fig. 4.10 a. The electron temperature rises very quickly to about 4500 K in the first 150 fs after excitation and then cools down over the next few picoseconds. The phonon temperature starts to rise a little delayed and reaches only around 1200 K after 7 ps, ensuring that the crystal structure is not changed and the crystal does not melt. However, at these timescales, transport of heat via phonons will start to play a role, probably reducing the maximal phonon temperature.

Figure 4.10 b shows a comparison between the experimental time-dependent XAS pump effect at 1236 eV (black dots, left axis) and the calculated electron temperature (blue line, right axis). The measurement shows a slightly delayed drop and a faster recovery compared to the calculated electron temperature, but the overall temporal evolution is already quite similar.

The description of the time-dependent pump effect can be improved, by simulating the temperature of only those $5d$ electrons, which carry enough energy to excite the first excited state in the $4f$ electronic system. Therefore, it is assumed, that all $5d$ electrons are energy-distributed according to a Fermi function. Electrons, which can transfer $\Delta E = E_1 - E_F = 280\,\mathrm{meV}$, can contribute to a population of the state at E_1 via scattering. Thus, the number of excited $4f$ states will be proportional to the amount of $5d$ electrons, able to relax into a hole that is ΔE below. Assuming a constant DOS $D(E) = D$ for simplicity, this number of $5d$ electrons is proportional to the convolution of the Fermi function $f(E)$ for electrons and a Fermi function $1 - f(E - \Delta E)$ for holes 280 meV below from $-\infty$ to ∞ (for mathematical derivation, see Appendix A.4):

$$g(E_1, T_{el}) = \int_{-\infty}^{\infty} D f(E, T_{el})(1 - f(E - \Delta E, T_{el}))\,\mathrm{d}E = D \frac{\Delta E}{e^{\frac{\Delta E}{k_B T_{el}}} - 1}. \qquad (4.7)$$

To determine the scaling factor between $g(t) = g(E_1, T_{el}(t))$ and the differential X-ray absorption signal $P(t)$, $g(t)$ is normalized such that

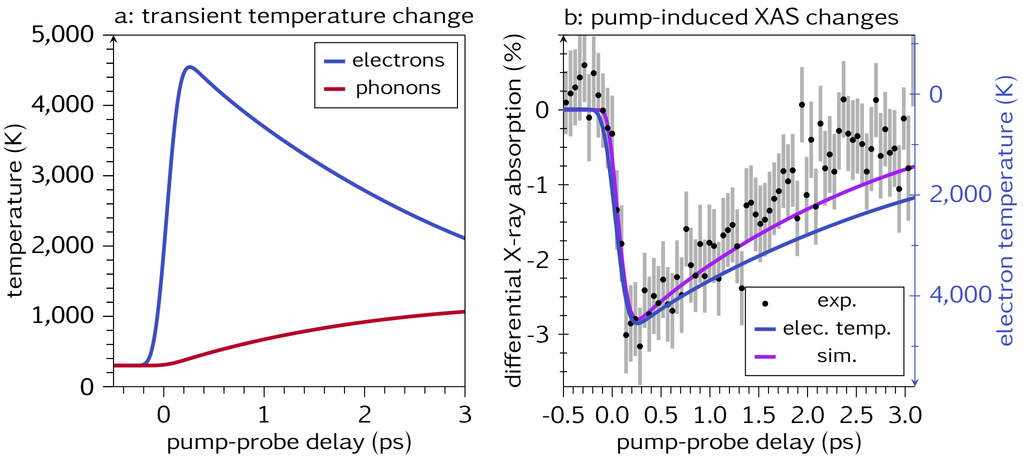

Figure 4.10: a: Pump-induced changes of electron (blue) and lattice (red) temperatures for an absorbed laser energy density of 3.2 kJ cm^{-3}, calculated by using a two-temperature model. At a pump-probe delay of about 150 fs an electron temperature of about 4500 K is reached, while the lattice temperature is far below.
b: Comparison between the measured transient XAS changes at 1236 eV (black dots, left axis) and the calculated electron temperature (blue line, right axis). The purple line is a simulation based on the electron temperature of those 5d electrons which can actually transfer enough energy to the 4f electronic system to provoke excitations out of the 4f ground state.

$\Delta g_{max} = P_{max}$. This leads to $P = -0.028\,\frac{g(t)}{g_{max}}$.
The result is displayed as solid purple line in Fig. 4.10 b. The estimated curve describes the experimental data a bit better. The drop is captured quite well, while the recovery is still slower in the simulation than in the experimental data.
The improvement of the simulation by taking into account only those 5d electrons able to scatter into a hole 280 meV below, consolidates the assumption of direct scattering between 4f and 5d electrons. Especially because the XAS signal does not only drop corresponding to the electron temperature but also recovers on a similar timescale, an exchange scattering rate proportional to the amount of 5d electrons can be assumed.

In this chapter it was demonstrated, that the difference in rise and decay times between the 5d electron temperature and transient XAS changes stem from the fact, that only those 5d electrons which can distribute $\Delta E = 280\,\text{meV}$ take part in $^7F_6 \rightarrow {}^7F_5$ 4f electronic excitation via inelastic scattering. The 5d electronic system must be sufficiently heated to continuously drive the 4f excitations, which becomes directly visible from the slight delay of the initial drop in XAS intensity in contrast to the temperature evolution of the whole 5d electronic system. These findings corroborate that 5d electrons with sufficient energy contribute substantially via inelastic decay to excitation of the ^7F_J multiplets.

4.3.4 Three-temperature model

In the previous chapter it was demonstrated that the valence-electron temperature simulated within a two-temperature model describes qualitatively well the pump effect which was observed in $3d \rightarrow 4f$ XAS, representing transient changes in the 4f electronic structure. Mismatches regarding the rising edge and recovery could be reduced by evaluating the temperature of only those valence electrons, which can transfer enough energy into the 4f electron system to provoke the $^7F_6 \rightarrow {}^7F_5$ multiplet excitation. However, the maximum temperature, which is reached by the 5d electron system, is around 4500 K, hence far above the 4f electronic temperature of (2038 ± 83) K estimated from the fit to the non-equilibrium XAS spectrum assuming Boltzmann-occupied 4f multiplets. The scattering processes between 5d and 4f electrons should be rather expected to cause thermalization between both systems associated with a specific coupling parameter.

Therefore, as a next attempt, a three-temperature model involving 5d valence electrons, 4f electrons and the lattice will be developed.

The 5d6s valence electronic system will be established similarly to the electronic system in the two-temperature model. It can interact with the lattice via electron-phonon interaction as well as with the 4f system via electron-electron scattering. Additionally, ballistic electron transport into less excited regions is taken into account by an effective attenuation length. The laser pulse will only deposit energy into the valence electrons. For a simpler notation, this system will be called 5d system.

The 4f system can interact with the lattice as well as with the valence electrons, but due to their localized character transport of electrons is not occurring.

The lattice system can interact with the valence electrons and the 4f electrons. Transport of energy via phonons to other areas of the sample is not implemented yet, because it plays only a very minor role on these ultrafast timescales [90].

The heat exchange between these systems can be described by three coupled differential equations similar to the two-temperature model. The differential equations for the temperature evolution are:

$$\frac{\mathrm{d}T_{5d}}{\mathrm{d}t} = \frac{-g_{5dp}(T_{5d} - T_{ph}) - g_{5d4f}(T_{5d} - T_{4f}) + \nabla \cdot (\kappa_{el} \nabla T_{5d}) + P_{laser}(t,z)}{C_{5d}},$$

$$\frac{\mathrm{d}T_{4f}}{\mathrm{d}t} = \frac{-g_{4fp}(T_{4f} - T_{ph}) + g_{5d4f}(T_{5d} - T_{4f})}{C_{4f}},$$

$$\frac{\mathrm{d}T_{ph}}{\mathrm{d}t} = \frac{+g_{5dp}(T_{5d} - T_{ph}) + g_{4fp}(T_{4f} - T_{ph})}{C_{ph}}.$$

In these equations the electron transport in the $5d$ system as well as the laser pulse P_{laser} are implemented as for the electronic system in the two-temperature model. Likewise, the phonon heat capacity C_{ph} is defined via the Einstein model as shown in Equation 4.6 and the $5d$ heat capacity C_{5d} is defined like the electronic heat capacity as $C_{5d} = \gamma_{el} * T_{5d}$ with $\gamma_{el} = 2.25 \times 10^{2}\,\mathrm{J/(m^3K^2)}$ [91]. The g terms describe the coupling strength between the systems. The $5d$-phonon coupling $g_{5dp} = 2.5 \times 10^{17}\,\mathrm{J/(m^3K)}$ was set to the same value as the electron-phonon coupling in the two-temperature model.

This leaves the model with three unknown parameters: the $4f$ heat capacity C_{4f}, the $4f$-phonon coupling strength g_{4fp} and the $5d$-$4f$ coupling strength g_{5d4f}.

C_{4f} can be calculated, when treating the $4f$ system in the local environment of the isolated atom. For a collection of separated atoms the temperature can be defined by the occupation of discrete states according to a Boltzmann distribution.

As the ^7F_J multiplets and their respective energy $E_{^7F_J}$ is known (see Tab. 2.1), the density of states (DOS) can be calculated by considering the degeneration of each state (deg$= 2J+1$) and spacing the states according to the corresponding energies. Figure 4.11 a presents the DOS for the ^7F_J multiplets by plotting the total amount of states per atom over energy.

Considering a thermal occupation for these states, a Boltzmann-like probability distribution is assumed as shown for different temperatures in Fig. 4.11 b. Combining the DOS with the probability distribution results in the occupation ($n_{^7F_J}(T)$) of the different ^7F_J multiplets. Normalizing $n_{^7F_J}(T)$ to the total amount of occupied states ($n_{total}(T) = \sum_J n_{^7F_J}(T)$) results in the relative occupation of the different ^7F_J multiplets as displayed over the $4f$ temperature in Fig. 4.11 c. Below a few hundred Kelvin, only the $^7F_6$ ground state is occupied. Higher multiplets become occupied only at elevated temperatures above 700 K. Multiplets at even higher energies

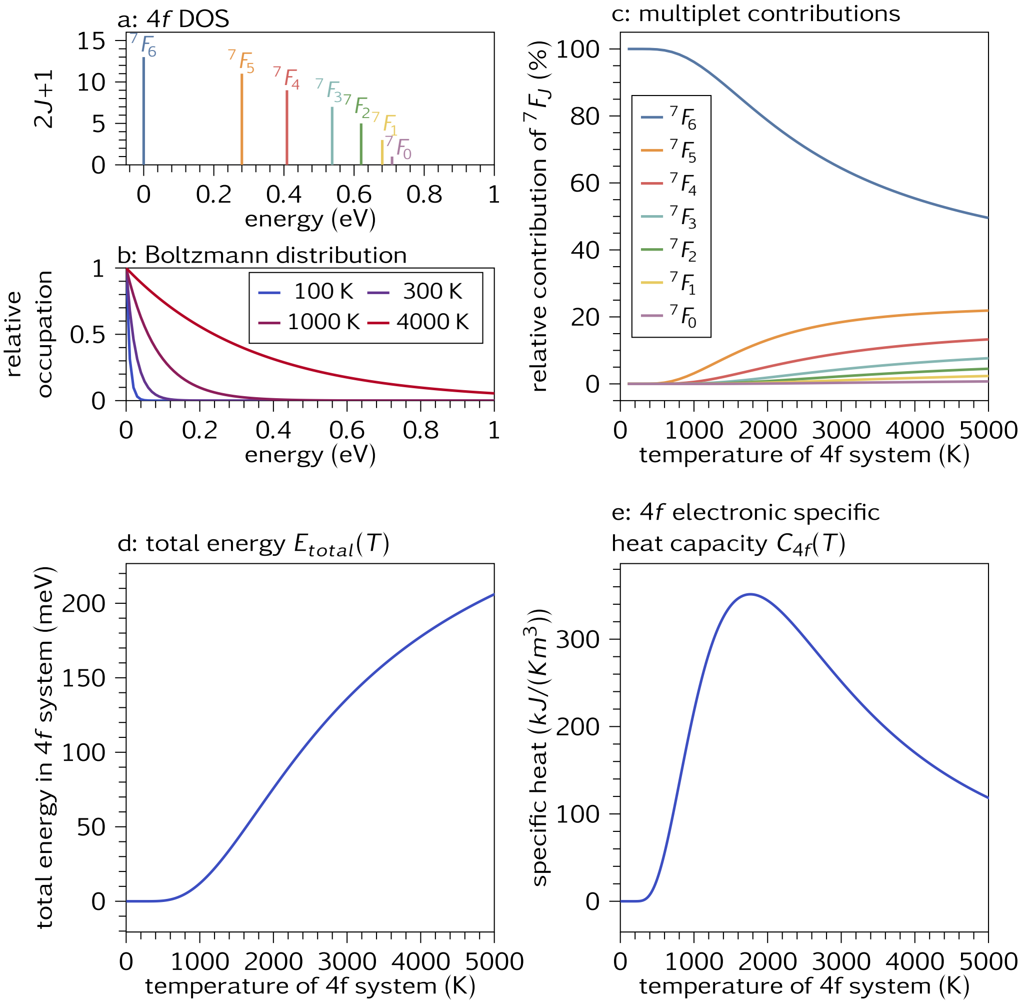

Figure 4.11: a: Degeneracy of the ^7F_J multiplet states.

b: Energy-dependent Boltzmann distribution for different temperatures.

c: Boltzmann-distributed occupation of ^7F_J multiplets over temperature.

d: Total energy stored in the 4f system.

e: Specific heat capacity of the 4f electronic system (derivative of the total energy).

than the $^7F_0$ state are neglected due to their by orders of magnitude smaller occupation.

Because the energy levels are known for all these states, the total energy stored in the 4f system can be calculated as

$$E_{total} = \frac{\sum_J (E_{^7F_J} \cdot n_{^7F_J}(T))}{n_{total}(T)}$$

and is shown in Fig. 4.11 d. The total energy stored in the 4f system increases as soon as higher multiplets become occupied around 700 K.

The heat capacity of the 4f system can now be calculated by derivating E_{total} by the temperature: $C_{4f}(T) = \frac{dE}{dT}$. Figure 4.11 e displays the 4f electronic heat capacity C_{4f} over the 4f temperature. This calculation was also done in Python and the code is shown in Appendix A.5.

In order to estimate the remaining two parameters g_{5d4f} and g_{4fp}, it is attempted to simulate experimental data. By calculating the 4f temperature with a three-temperature model, extracting the ^7F_J occupation for each temperature and using those to estimate admixtures of higher multiplets, the temporal evolution of the differential X-ray absorption can be simulated in an atomistic framework. By adapting the two missing coupling strength parameters, the simulated temporal evolution of the differential X-ray absorption can be matched to the respective experimental data.

Figure 4.12 a shows the evolution of the 5d, 4f and phonon temperatures calculated with the three-temperature model, based on g_{5d4f} and g_{4fp} parameters adjusted to fit the experimental data. Due to the excitation by the laser pulse, the 5d temperature rises very quickly in the first few hundred femtoseconds and then cools down until equilibration with the other subsystems. The 4f temperature follows the 5d temperature with a slight delay. The phonon temperature rises on a considerably slower timescale until equilibration with the electronic systems.

To achieve this behavior, the 4f-phonon coupling was set to a value of $g_{4fp} = 1.8 \times g_{5dp} = 4.05 \times 10^{17}$ J/(m^{3}K), while the 5d-4f coupling was made temperature-dependent by scaling it with the amount of electrons, that can excite at least the first excited 4f multiplet $^7F_5$ (compare Equation 4.7). The 5d-4f coupling is formulated accordingly as

$$g_{5d4f}(T_{5d}) = g_{5d4f,0} * D * \frac{\Delta E}{e^{\frac{\Delta E}{k_B T_{5d}}} - 1},$$

with $\Delta E = 0.28$ eV corresponding to the energy needed to excite the $^7F_5$ multiplet. The DOS D of the 5d system was calculated by K. Carva and is

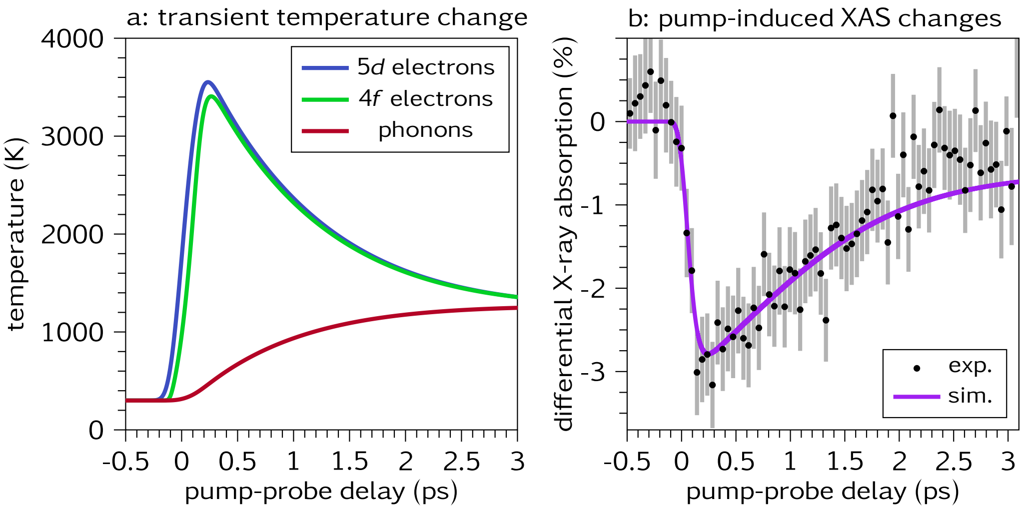

Figure 4.12: a: Pump-induced changes of 5*d* electron (blue), 4*f* electron (green) and lattice (red) temperatures for an absorbed energy density of 3.2 kJ cm^{-3} calculated by using a three-temperature model. At a pump-probe delay of about 150 fs a 5*d* electron temperature of about 3500 K is reached. The 4*f* temperature follows with a slight delay, while the lattice temperature is far below.
b: Comparison between the measured pump-induced changes in the XAS signal at 1236 eV (black dots) and the simulation (purple) based on the 4*f* temperature and respective admixtures of higher multiplets. The temporal evolution is described very well.

shown in the appendix of [2]. It shows that the DOS varies slightly around the Fermi edge, but can be averaged to 4 eV^{-1} for ±2 eV around the Fermi edge. $g_{5d4f,0}$ was set to 1.25×10^{19} J/(m^{3}K). The Python implementation is shown in Appendix A.6.

That the electron-phonon coupling is stronger for the 4*f* system than for the 5*d* system can be justified by the larger orbital momentum carried by the 4*f* electrons. The temperature dependence of g_{5d4f} stems from the assumption that energy between the 5*d* and the 4*f* system can only be exchanged by 5*d*-4*f* scattering as described in Chapter 4.1.1. If enough energy is available to excite the 4*f* multiplet via scattering, the process is assumed to be very effective, because it bases on direct interaction of electrons with a large wavefunction overlap. Hence, $g_{5d4f,0}$ is quite large. The comparison to the temporal evolution of the differential X-ray absorption is shown in Fig. 4.12 b. The experimental data (black dots) were measured at an energy of 1236 eV, while the simulation (purple curve) corresponds to the temperature based simulated differential X-ray absorption at 1235.8 eV. However, the experimental data is described very well by the simulation. Only at larger pump-probe delays ($> 2\,\mathrm{ps}$) experiment and simulation diver slightly.

During the XAS experiment at the EuXFEL the data displayed in Fig. 4.13 a was measured. Shown is a color-coded map for the differential X-ray absorption over pump-probe delay and photon energy. After excitation of the $5d$ electrons a clear pattern evolves with decreased absorption below 1236 eV and above 1237 eV, while increased absorption is observed between 1236 and 1237 eV and around 1235 eV.

Such a map can as well be simulated, using the $4f$ temperature and is shown in Fig. 4.13 b. The simulated map takes into account a $4f$ temperature broadened in time by a Gaußian with $\sigma = 0.25\,\mathrm{ps}$ to compensate for the worse time resolution for longer scans at EuXFEL during the measurement. Then spectra were calculated by superposition of atomically calculated multiplet spectra corresponding to the occupation at a certain $4f$ temperature. The same energy-dependent pattern, as observed in the experimental data, is nicely reproduced by the simulation.

For a better comparison the differential X-ray absorption was integrated over two different time windows marked with I ($-0.03 - 0.14\,\mathrm{ps}$) and II ($0.14 - 0.43\,\mathrm{ps}$) in Fig. 4.13 a and b and are shown in Fig. 4.13 c and d, respectively. The experimental data (black dots) can be qualitatively described by the simulation (purple line) within the error bars. The fits can be improved slightly by choosing a larger σ for time broadening, hinting on a lower time resolution than expected.

Being able to simulate the experimental data with this simple three-temperature model solidifies the assumption that $5d$-$4f$ electron-electron scattering, which leads to an excitation of the $4f$ multiplets, transfers energy between the $5d$ and the $4f$ electrons on ultrafast timescales. The $4f$ temperature can be understood as Boltzmann-distributed occupation of ^7F_J multiplets.

Some possible improvements to this three-temperature model are to include phonon heat transport, to use the DOS calculated by K. Carva [2] to estimate the amount of electrons available for $5d$-$4f$ scattering more accurately or to describe the sample more appropriately by adding layers of different material to the model.

Overall, the simulations show that the $4f$ system reaches at least a temperature of over 2000 K. Assuming the density of atoms for terbium to be $3.12 \times 10^{22}\,\mathrm{atoms/cm^3}$ and a total energy stored per atom of 75.8 meV at 2000 K (taken from Fig. 4.11 d), an energy density of $0.379 \times 10^3\,\mathrm{J\,cm^{-3}}$ stored in the $4f$ system can be calculated. This means, about 11% of the maximum total absorbed energy density of $3.4 \times 10^3\,\mathrm{J\,cm^{-3}}$ (see

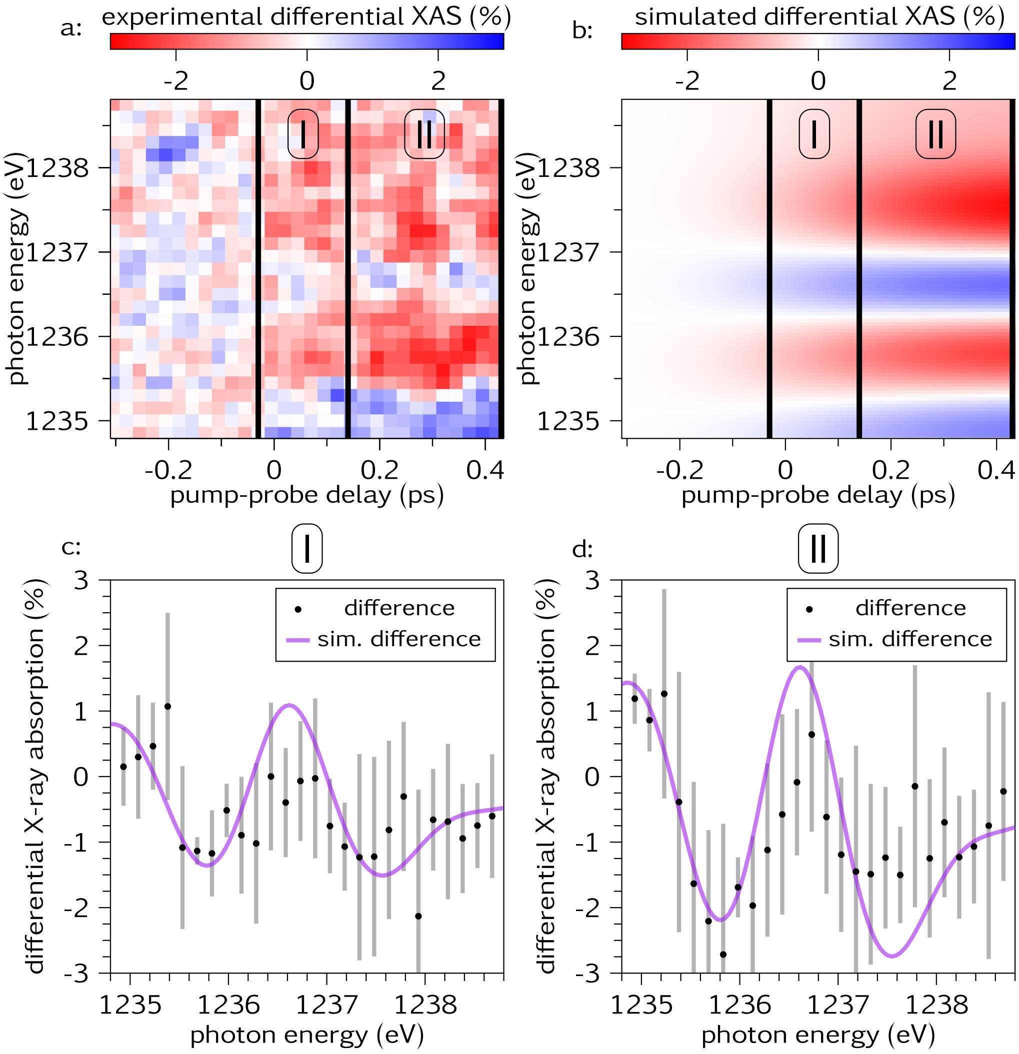

Figure 4.13: a: Differential X-ray absorption map of the Tb M_5 edge.
b: Simulation of the differential X-ray absorption based on the 4*f* temperature and corresponding admixtures of higher multiplets to the spectrum.
c: Comparison between experiment and simulation of the differential X-ray absorption integrated over area I (−0.03 – 0.14 ps).
d: Comparison between experiment and simulation of the differential X-ray absorption integrated over area II (0.14 – 0.43 ps).

Chapter 4.3.2) is transiently transferred into the 4*f* system. It can be speculated that this might be improved by *e.g.* suited sample compositions with altered valence band structure, influencing the 5*d*-4*f* electronic overlap and hence increasing the efficiency of the 5*d*-4*f* scattering process.

4.3.5 5*d*-4*f* electron transfer

The time-resolved spectral changes in M_5 edge XAS (Chapter 4.1) and $N_{5,4}$ edge RIXS (Chapter 4.2) were qualitatively well described on the basis of atomistic calculations and respective superposition of the $^7F_6$ ground state and energetically higher ^7F_J multiplet spectra. Via the temporal evolution of the differential XAS and RIXS signals and the dominant contribution of the $^7F_6 \rightarrow {}^7F_5$ transition, the excitation mechanism involving inelastic 5*d*-4*f* electron-electron scattering were identified.

Still, the comparison between experimental XAS data and simulations (Fig. 4.9) discloses deviations, which cannot be conformed to each other by involving $4f^8$ multiplets only.

An excitation process that was not considered yet, is electron transfer from the 5*d* into the 4*f* electronic system, or vice versa. Figure 4.14 visualizes such electron transfer processes between Fermi-distributed 5*d* states and discrete 4*f* energy levels. A 5*d* electron, with sufficient energy, can transfer into the lowest unoccupied 4*f* state, resulting in a $4f^9$ $^6H_{15/2}$ configuration or the highest bound 4*f* electron can transfer into an empty 5*d* state, leading to an $4f^7$ $^8S_{7/2}$ state. These transitions require 2.8 and 2.3 eV, respectively [95].

As the energy of the pump laser is only 1.55 eV, such excitation can not be driven directly by the optical pulse. However, the 5*d* electronic system thermalizes within tens of femtoseconds after excitation, forming a hot Fermi distribution. This leads to a very small amount of 5*d* electrons at very high and holes at very low energy. For example at 4500 K about 0.07% of all states at 2.8 eV above E_F are filled and about 0.26% of all states at −2.3 eV below E_F are empty.

Certainly, only a small amount of 5*d* electrons or holes would allow for such charge transfer. However, the mechanism is expected to be efficient, though: The 5*d*-4*f* electron transfer is dependent on the overlap and thus the hybridization of 5*d* and 4*f* states. In fact, this overlap mediates magnetic order in 4*f* metals via the so called RKKY exchange [51, 52, 53]. As the 4*f* moments of adjacent atomic sites do not interact directly with each other, magnetism stems from the indirect exchange via the itinerant

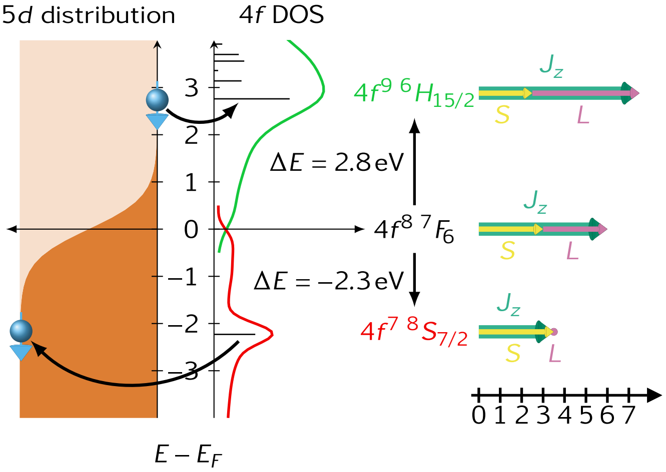

Figure 4.14: Scheme demonstrating the electron-transfer process between 5*d* electronic system (left) and 4*f* states (right). After thermalization of the laser excited 5*d* electrons, they form a hot Fermi distribution. A small amount of 5*d* electrons has enough energy ($E_F + 2.8\,\mathrm{eV}$) to tunnel into the lowest empty 4*f* state, leading to a $4f^9\ {}^6H_{15/2}$ configuration. Likewise the highest bound 4*f* electron can occupy an empty 5*d* state at $E_F - 2.3\,\mathrm{eV}$, leaving behind a $4f^7\ {}^8S_{7/2}$ configuration.

and spin-polarized 5*d* electrons [7]. This suggests a strong hybridization of 5*d* and 4*f* states, which can be described by virtual *f*-*d*-*d*-*f* scattering processes. Actual occupation of *d* and *f* states will strongly amplify respective tunneling processes and hence makes the electron transfer very efficient.

The spectral shape for the $4f^9\ {}^6H_{15/2}$ and $4f^7\ {}^8S_{7/2}$ can be reliably calculated, however, the energy position with respect to the $4f^8$ ground state is uncertain. Adding or removing a localized 4*f* electron changes the core-hole screening and hence influences the energy position of the XAS spectrum. Consequently, an energy shift needs to be considered in the simulation as additional parameter.

The simulations, including $4f^9$ and $4f^7$ multiplets, describe the differential XAS very well and in a quantitative manner (Fig. 4.15). The purple curve in Fig. 4.15 a considers a 4*f* temperature of $(2071 \pm 93)\,\mathrm{K}$ combined with $(2.8 \pm 0.1)\,\%$ $4f^9$ and $(7.4 \pm 1.5)\,\%$ $4f^7$. Also the absolute XAS signal is well described (Fig. 4.15 b).

The higher contribution of the $4f^7$ compared to the $4f^9$ multiplet can be explained by the lower transition energy. As described above, at a 5*d* temperature of about 4500 K, the number of holes at an energy of $E_F - 2.3\,\mathrm{eV}$ is three times larger than the number of electrons at $E_F + 2.8\,\mathrm{eV}$. Hence,

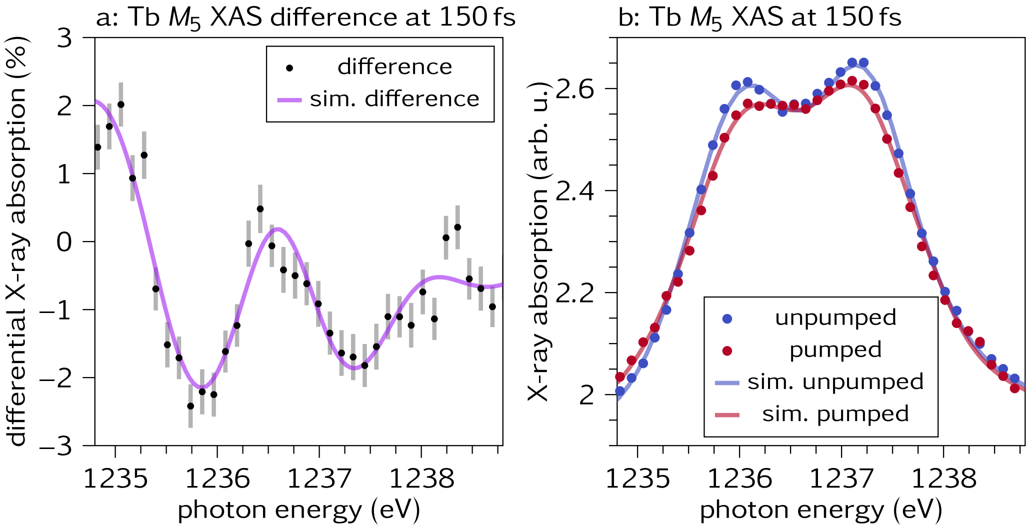

Figure 4.15: a: Simulation of the differential X-ray absorption for the terbium M_5 edge at 150 fs delay including $4f^9$ and $4f^7$ multiplets. The best agreement between simulation and data is found for a $4f$ temperature of (2071 ± 93) K admixed with (7.4 ± 1.5) % of the $4f^7$ multiplet and (2.8 ± 0.1) % of the $4f^9$ multiplet. b: Simulated and experimental X-ray absorption data for the pumped (red) and the unpumped (blue) sample.

the contribution of the $4f^7$ multiplet is about three times higher compared to the $4f^9$ multiplet. The $4f$ temperature of (2071 ± 93) K is also well in accordance with the simulation without transfer states.

Another indication that more than only the $4f^8\ {}^7F_J$ states get excited, can be found, when looking at the time evolution of the energy-dependent pump effect. The differential X-ray absorption map in Fig. 4.13 a shows, that after laser excitation the XAS signal at 1236 and 1237.4 eV is reduced. However, the feature at 1237.4 eV seems to evolve differently than the feature at 1236 eV. This becomes more obvious when Fig. 4.13 c and d are compared, *i.e.* the differential X-ray absorption integrated over an earlier time interval I (−0.03 – 0.14 ps) and the later time window II (0.14 – 0.43 ps). While the differential absorption at 1236 eV decreases from around −1 % in region I to about −2 % in region II, the reduction around 1237.4 eV is clearly less pronounced. Simulating these different dynamics while including only the $4f^8\ {}^7F_J$ states is not possible, because all $7F_J$ states introduce a stronger reduction of the XAS at 1237.4 eV than at 1236 eV. Including the $4f^7$ and $4f^9$ states at a ratio of 3:1, the differential X-ray absorption for both time windows can be simulated quite well. This is demonstrated by the purple lines in Fig. 4.16. The admixture of the excited states for the best fit in region I and II is displayed in Tab. 4.3.

In the RIXS spectra at 147.2 eV no indication for 5d-4f electron transfer processes could be found. However, they might just have been missed, because the RIXS cross-section for specific multiplets strongly depends on the excitation energy.

Although for the estimated 5d electron temperature, only a small amount of 5d electrons and holes can be expected to allow for 5d-4f electron transfer, the strong overlap between 5d and 4f states could make such kind of excitations very efficient, resulting in considerable contribution of $4f\,^8S_{5/2}$ and $4f\,^6H_{15/2}$ states, as indicated by the simulations.

Excitation into the $4f^7\,^8S_{7/2}$ state leads to a gadolinium-like configuration with a half-filled 4f shell. This configuration has a reduced J and a L of 0. Hence the respective orbital is symmetric and the MCA is reduced by three orders of magnitude with respect to the terbium ground state [9]. Reaching the $^6H_{15/2}$ state forms a dysprosium-like configuration with an increased J, but a slightly reduced MCA [10]. Both electron transfer states change the coupling of 4f electrons to the lattice and hence should influence the demagnetization process.

4.3.6 Summary

It was shown that the spectral change as well as the temporal evolution of the Tb M_5 edge XAS can be described by simulation based on a three-temperature model, separating the lattice, the valence electron as well as the 4f electron temperature. The 4f temperature is represented by a Boltzmann-distributed occupation of the ^7F_J multiplets. Assuming the coupling strength between the 5d and 4f electronic system to be dependent on the amount of 5d electrons, able to introduce 4f excitations via 5d-4f electron-electron scattering, yields a good description of the experimental data.

Remaining mismatches between simulation and experimental spectra

Table 4.3: Admixture of states corresponding to the best simulation for the integrated differential X-ray absorption displayed in Fig. 4.16.

	4f T	$\sum 4f^8\,^7F_{J<6}$	$4f^7$	$4f^9$
area I	(1614 ± 53) K	(14 ± 1) %	(3.5 ± 0.5) %	(1.2 ± 0.2) %
area II	(2032 ± 47) K	(21.9 ± 0.8) %	(7.6 ± 0.5) %	(2.5 ± 0.2) %

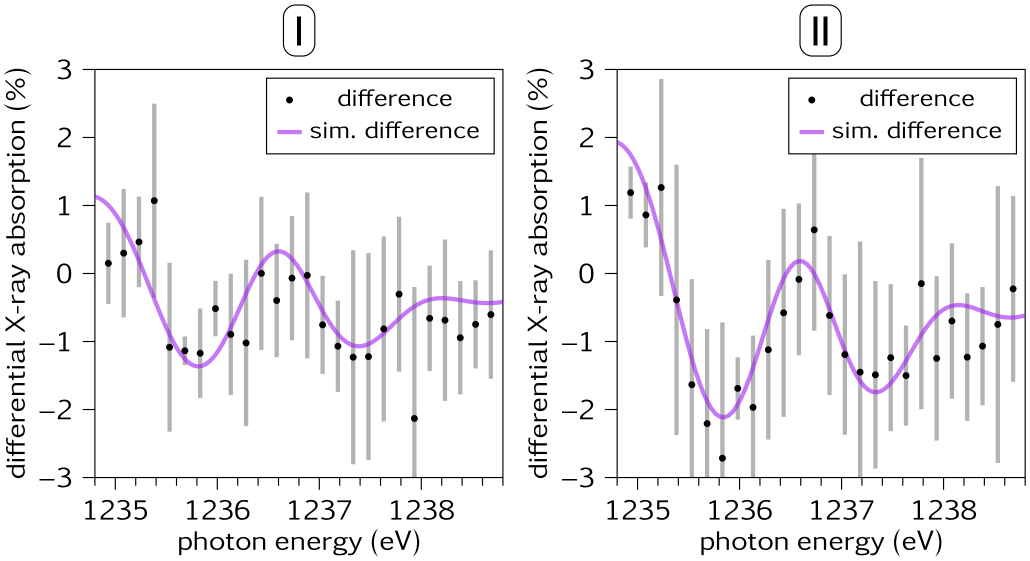

Figure 4.16: Energy-dependent differential X-ray absorption averaged over the time intervals I (−0.03 – 0.14 ps) and II (0.14 – 0.43 ps) indicated in the map shown in Fig. 4.13. While the XAS at around 1236 and 1237.3 eV is reduced by about 1 % in the first window (I), the development differs in the second time window (II). The purple lines display simulation for both areas including electron transfer states.

were speculated to stem from additional electron transfer contributions. Including those improves the simulation significantly, but also introduces additional fitting parameters, reducing robustness of the result.
Further studies on the temporal evolution of the energy-dependent pump effect will help to improve the understanding on the energetically higher multiplet excitations, including possible charge-transfer processes.

4.4 Ultrafast changes of the $M_{5,4}$ absorption branching ratio in terbium

An additional indication for electronic excitations out of the 4*f* ground state multiplet arises from changes of the overall M_5 and M_4 edge intensity, as observed for terbium in XAS experiments at EuXFEL as shown in Fig. 4.17. The colored area below the graph is proportional to the spectral weight of the resonance. Dividing the integral over the M_5 edge by the sum of the integrals over the M_4 and M_5 edges gives a value proportional to the branching ratio induced by spin-orbit splitting. Upon pumping the

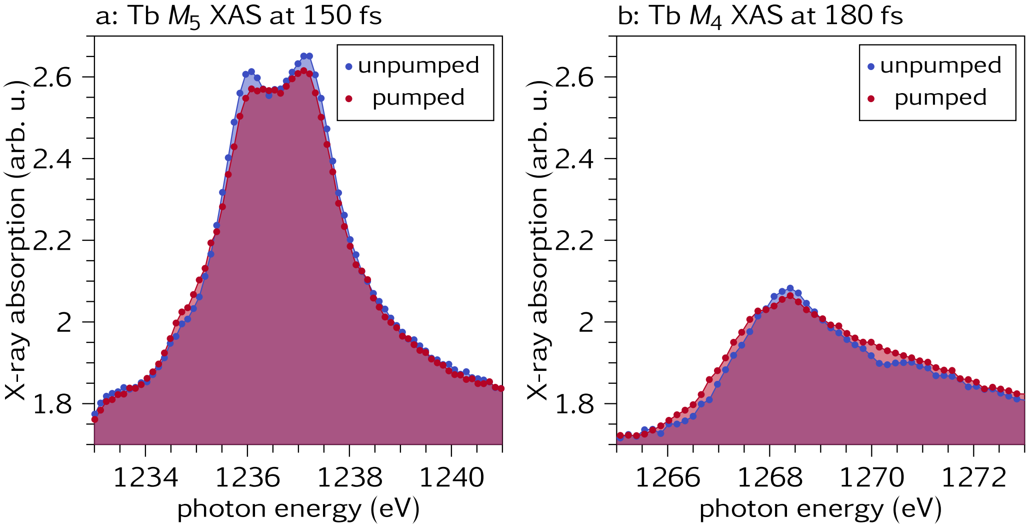

Figure 4.17: Pump-induced change at the terbium M_5 edge recorded at 150 fs delay (a) and the terbium M_4 edge recorded at 180 fs delay (b). While the integral over the M_5 edge (indicated by the colored area) decreases after pumping, the integral over the M_4 edge increases. This indicates a transfer of spectral weight from the M_5 to the M_4 resonance.

sample, the integral over the M_5 edge decreases, while the integral over the M_4 edge increases, which corresponds to a reduction of the branching ratio $\frac{M_5}{M_5+M_4}$.

Considering the 3rd rule of Thole and van der Laan [5], this effect can be interpreted and utilized to detect $4f$ multiplet excitations. In case of a shell being more than half filled, optical transitions from spin-orbit split initial states, such as for $L_{3,2}$ and $M_{5,4}$ edges in transition and rare-earth metals, exhibit the largest branching ratio for $J = L + S$. The branching ratio gradually decreases with J. This means, that for terbium with a more than half filled $4f$ shell the branching ratio is largest for the ${}^7F_6$ ground state. A decrease in the branching ratio upon pumping indicates a reduction of atomic J, as expected from a change in the electronic configuration.

For a thorough investigation of optically induced changes of the $M_{5,4}$ absorption branching ratio, an additional experiment was performed at the FemtoSlicing facility of BESSY II in Berlin. In this XAS study a terbium thin film sample (see Chapter 3.3.3) was examined at room temperature. Ultrafast changes at the M_5 and M_4 edge were probed upon excitation with 800 nm laser pulses at a fluence of $(6 \pm 1)\,\mathrm{mJ/cm^2}$.

4.4.1 Data acquisition

During the XAS experiment at the FemtoSlicing facility spectra around the terbium $M_{5,4}$ edge were measured over several days. The absorption spectra were recorded for the unexcited sample as well as for different delays between the 800 nm-pump and the X-ray-probe pulses.

The FemtoSlicing facility provides stable experimental conditions regarding the photon energy, pulse length and beam pointing. Further, the intrinsic synchronization of pump and probe pulse avoids temporal jitter. In measurements over several days, though, drifts in photon energy and temporal pump-probe overlap can occur. In order to correct energy shifts of the X-ray pulses, the pronounced terbium M_5 resonance at around 1236 eV was measured every two hours and its position was fitted via a Gaußian profile.

To correct for timing drifts, the ultrafast change of absorption at the M_5 edge was used. About once every two hours the temporal profile of this drop was measured and fitted with a double exponential function to determine the temporal drift correction.

The measured XAS signal in the experiment can be described by $I(E) = (I_0 - \Delta I_{background}(E)) * \exp(-\mu(E) * d)$. Here, I_0 is the incoming intensity while $\Delta I_{background}$ denotes the energy-dependent change of the intensity, induced by the non-terbium parts of the sample. $\mu(E)$ is the absorption coefficient and d denotes the sample thickness. In a first step the background signal outside the absorption edges was fitted. The model used for the fit is described in Chapter A.7. The result of the fit is shown in Fig. 4.18. Figure 4.18 a depicts the measured transmitted intensity $I(E)$ as blue dots. The background fit is shown in red and the regions used for fitting are colored gray. Dividing $I(E)$ by the result of the background fit leads to $I(E)/(I_0 - \Delta I_{background}(E)) = \exp(-\mu(E) * d)$ as is shown in Fig. 4.18 b.

In a next step the negative natural logarithm is taken, to extract the extinction: $A(E) = -\ln(I(E)/(I_0 - \Delta I_{background}(E))) = \mu(E) * d$

Building the following quotient including the background-corrected extinction $A(E)$

$$\frac{\int\limits_{E=M_5} A(E)}{\int\limits_{E=M_5} A(E) + \int\limits_{E=M_4} A(E)} = \frac{\int\limits_{E=M_5} \mu(E) * d}{\int\limits_{E=M_5} \mu(E) * d + \int\limits_{E=M_4} \mu(E) * d} = \frac{\int\limits_{E=M_5} \mu(E)}{\int\limits_{E=M_5} \mu(E) + \int\limits_{E=M_4} \mu(E)}$$

cancels out the sample thickness d and results in the definition of the $M_{5,4}$ absorption branching ratio.

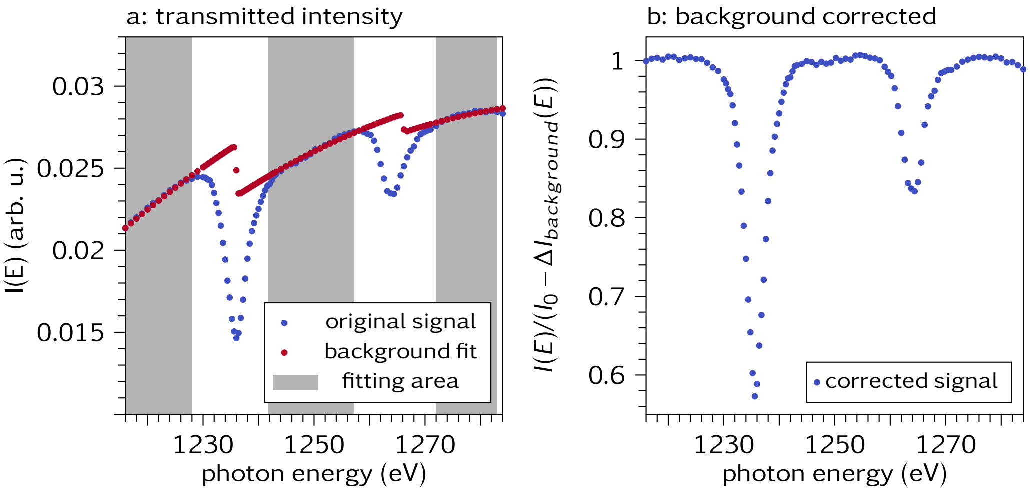

Figure 4.18: a: The blue dots depict the measured transmitted intensity at the terbium M_5 and M_4 edge for the unpumped sample. The background fit for correction is shown in red. For the fit only the gray colored regions were used.
b: Background-corrected signal $I(E)/(I_0 - \Delta I_{background}(E))$.

As the absorption coefficient $\mu(E)$ can be calculated by atomistic calculation (see Chapter 2.5), the $M_{5,4}$ absorption branching ratio can also be determined from these theoretical values. This holds true not just for the ground state $^7F_6$ but also for higher multiplet terms and their admixtures. The goal of the following evaluation is to extract the amount of admixed higher ^7F_J multiplet states to the $^7F_6$ ground state by comparing the experimentally measured branching ratio with the theoretically calculated one. However, as the absolute value of the experimental branching ratio does not fit the corresponding theoretical prediction and further is not constant for different spectra of the unpumped sample, it proved a lot more feasible to compare the relative change of the $M_{5,4}$ absorption branching ratios at different delays after optical pumping. Indeed, the detection scheme at the slicing facility, recording each data point in alternation for the pumped and unpumped sample, is specifically optimized to compare relative changes in the signal. Thus, by normalizing the branching ratio of the spectra for the pumped case by the corresponding one of the unpumped sample a robust estimate of the admixture of higher ^7F_J multiplets to the pure $^7F_6$ state can be given.

4.4.2 Experimental data

Figure 4.19 a shows exemplary the background-corrected absorption $A(E)$ for the unpumped (blue dots) and pumped (red dots) sample at a pump-probe delay of 0.4 ps. Around the M_5 edge the absorption decreases upon pumping, while at the M_4 edge the absorption increases. For better visualization, Fig. 4.19 b displays the absolute pump effect obtained by subtracting the absorption spectrum for the pumped by the one for the unpumped sample. A clear dip can be observed at the M_5 edge, while a peak arises at the M_4 edge.

By integrating over the colored regions around the M_5 and M_4 edge in Fig. 4.19 a, respectively, their spectral weight can be calculated and used to obtain the $M_{5,4}$ absorption branching ratio. Figure 4.19 c shows the ratio determined this way for different pump-probe delays. As the $M_{5,4}$ absorption branching ratio is not constant for the unpumped spectra, the absolute values can not be compared directly. This might stem from variations in the background correction or intensity fluctuations during the experiment. Due to the alternating measurement mode of pumped and unpumped signal at the FemtoSpex slicing facility, the probed signal without prior pump-pulse excitation can be perfectly used to correct for such fluctuations. By normalizing to the unpumped branching ratio for each delay, the relative change of the $M_{5,4}$ absorption branching ratio can be determined and is shown in Fig. 4.19 d. The branching ratio drops very fast by about $(2.0 \pm 0.2)\%$ in the first few hundred femtoseconds after excitation. According to the 3rd rule of Thole and van der Laan [5] such a reduction in branching ratio corresponds to a reduction in J, which is exactly what is expected for a transition from the $^7F_6$ ground state to an excited $^7F_{J<6}$ state.

Additionally, time traces were recorded to better follow the temporal evolution of the pump effect. Figure 4.20 b shows the changes in absorption for different energies around the M_5 (blueish colors) and M_4 (greenish colors) edges marked in Fig. 4.20 a to occur within the first few hundred femtoseconds after excitation and to recover over the following 4 ps. These timescales match the temporal response observed at the EuXFEL (compare with Fig. 4.1 b). The energies shown by vertical lines in Fig. 4.20 a were chosen to highlight, that due to the energy resolution of about 2 eV the observed temporal profiles at all energies around the M_5 or M_4 edge are the same with only slight intensity variation due to averaging over large parts of the absorption edge by the energy resolution.

The temporal evolution of the branching ratio matches that of the 4f mul-

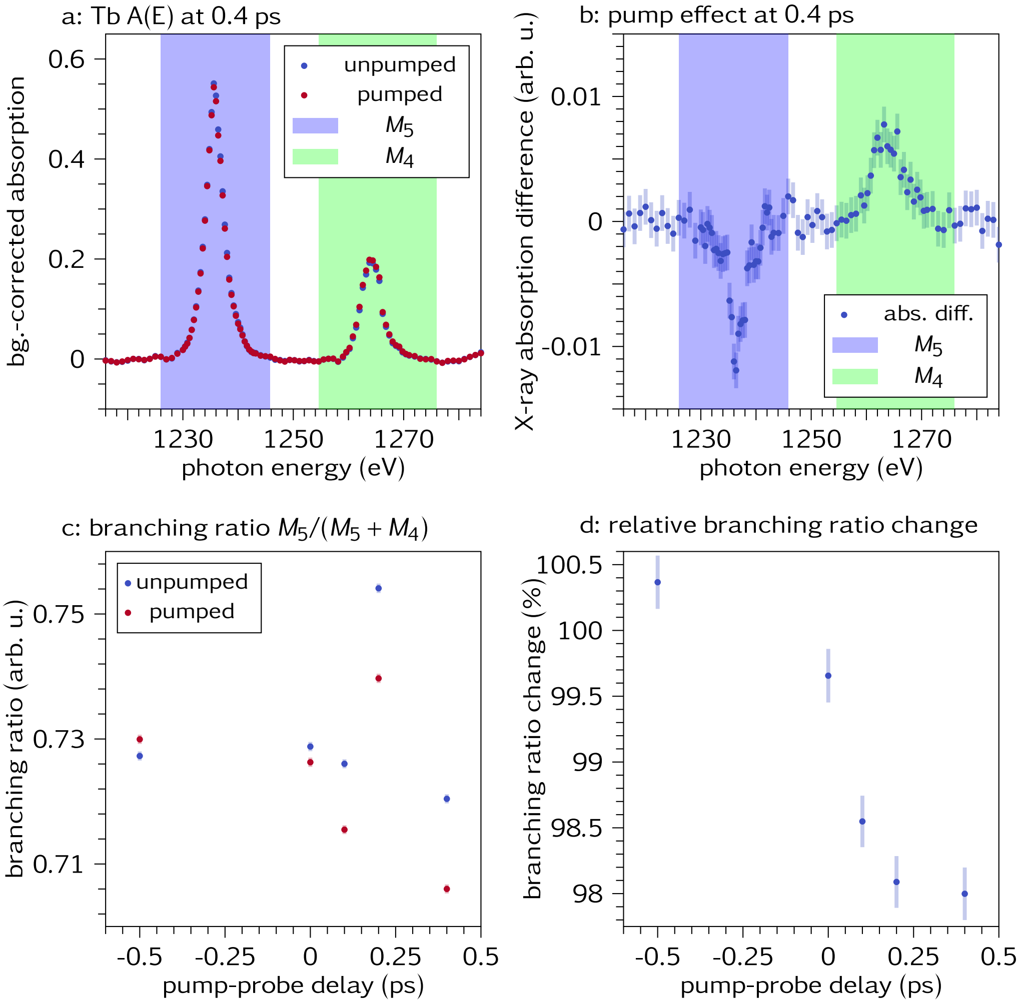

Figure 4.19: a: Background-corrected absorption spectrum $A(E)$ recorded at 0.4 ps pump-probe delay. The red (blue) dots depict the pumped (unpumped) spectrum. The colored areas mark the integration range for the M_4 (green) and M_5 (light blue) edge. At the M_5 edge the X-ray absorption has decreased upon pumping, while at the M_4 edge it has increased.
b: Pump effect as the absolute difference between the signal for the pumped and unpumped sample from a.
c: $M_{5,4}$ absorption branching ratio for pumped (red) and unpumped (blue) sample over time delay.
d: Relative change of the branching ratio, which drops upon excitation by about (2.0 ± 0.2) % in the first few hundred femtoseconds.

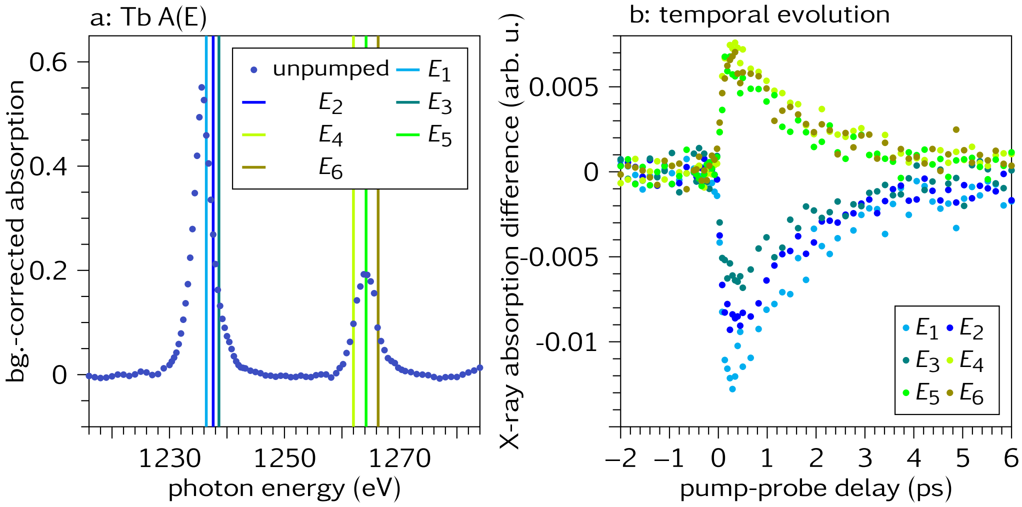

Figure 4.20: a: Background-corrected absorption spectrum with colored lines marking the energies (E_1 = 1236.4 eV, E_2 = 1237.6 eV, E_3 = 1238.6 eV, E_4 = 1262 eV, E_5 = 1264.2 eV, E_6 = 1266.3 eV), of which time traces were taken.
b: Temporal evolution of the X-ray absorption difference after pump-pulse excitation at different energies around the M_5 and M_4 edge (marked in a). The pump effect occurs in the first few hundred femtoseconds after excitation and recovers within the following 4 ps, corresponding to the same time profile as observed at EuXFEL (compare with Fig. 4.1 b).

tiplet excitations observed in time-resolved X-ray absorption and RIXS. This proofs that the 3rd rule of Thole and van der Laan is also valid in non-equilibrium.

4.4.3 Pure $^7F_5$ excitation

In the following, the contribution of the $^7F_{J<6}$ excitations will be qualitatively analyzed by evaluation of the branching ratio in spectra obtained by atomistic calculations.
As a first step only the $^7F_5$ state is considered, as it will have the highest contribution. Figure 4.21 a and b show calculated spectra for the terbium $^7F_6$ and $^7F_5$ state. After integrating over the colored areas to obtain the spectral weight of the M_5 and M_4 edges, the branching ratio is calculated. The $^7F_6$ state exhibits a $M_{5,4}$ absorption branching ratio of 0.759, while for the $^7F_5$ state a value of 0.687 is determined. This decrease in branching ratio is in accordance with the 3$^{\text{rd}}$ rule of Thole and van der Laan [5]. Accordingly also for admixtures of the $^7F_5$ to the $^7F_6$ ground state a decrease

of the $M_{5,4}$ absorption branching ratio is found in the spectra.

For comparison with the experimental data shown in Fig. 4.19 d, the relative change in $M_{5,4}$ absorption branching ratio is calculated for different admixtures of the $^7F_5$ state to the $^7F_6$ ground state. The result is shown in Fig. 4.21 c. The branching ratio decreases linearly and reaches a maximum deviation of about 10 % for the pure $^7F_5$ state. This relation can be used to translate the relative change of the branching ratio observed in the experiment to a contribution of the $^7F_5$ multiplet.

Figure 4.21 d shows the deduced $^7F_5$ contribution over pump-probe delay, which reaches a maximum value of (21 ± 2) %.

4.4.4 Occupation of higher ^7F_J multiplets

As discussed in Chapter 4.3, 5*d*-4*f* scattering could lead to even higher excited multiplets than the $^7F_5$ state. Direct interaction of 5*d* and 4*f* electrons by inelastic scattering causes 4*f* electronic excitation. On ultrafast timescales deexcitation of the 4*f* electronic system can only be effectuated by another 5*d*-4*f* electron-electron scattering event. Thermalization between 4*f* and 5*d* electrons would be the consequence and accordingly a temperature could be assigned to a Boltzmann-occupied 4*f* electronic system.

The Boltzmann distribution determines the relative contribution of the different ^7F_J multiplets at a given temperature (Fig. 4.11 c). From corresponding superposition of atomistic spectra for the pure ^7F_J multiplets, the branching ratio for different 4*f* temperatures can be deduced. Since the experiment was performed at room temperature, the obtained values for the temperature-dependent branching ratio were normalized to the ratio at 300 K (Fig. 4.22 a). By using this relation, the experimentally measured $M_{5,4}$ absorption branching ratio change can be translated into a temperature. Figure 4.22 b shows the evolution of the 4*f* temperature over pump-probe delay. The temperature rises to (1920 ± 110) K at its maximum, which is far above the lattice temperature of the system in the respective pump-probe delay range.

The relative occupation of ^7F_J multiplets for a 4*f* electronic temperature of (1920 ± 110) K is shown in Tab. 4.4. About (20 ± 2) % of all atoms in the probed volume are in an excited state $^7F_{J<6}$.

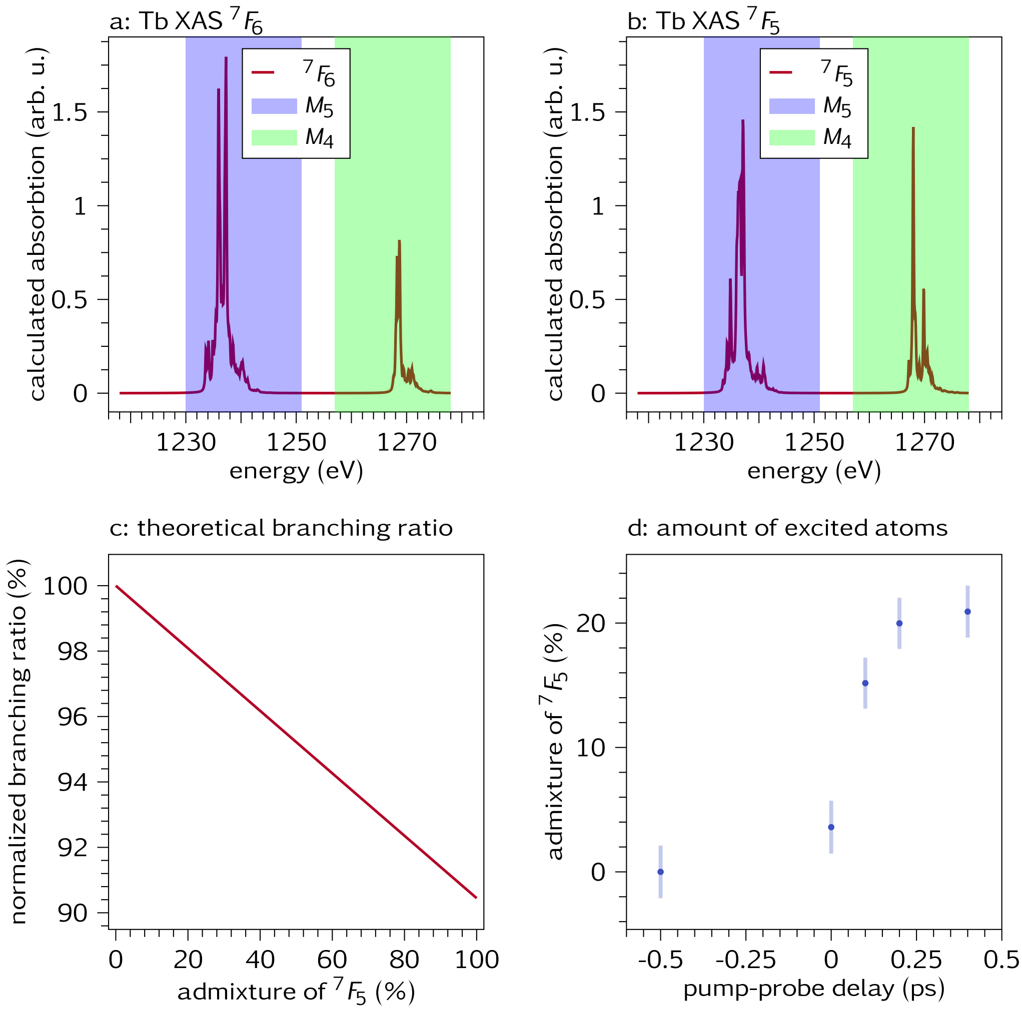

a: Tb XAS $^7F_6$

b: Tb XAS $^7F_5$

c: theoretical branching ratio

d: amount of excited atoms

Figure 4.21: a and b show spectra for the $^7F_6$ and $^7F_5$ atomic configuration obtained by atomistic calculations.
c: $M_{5,4}$ absorption branching ratio normalized to the branching ratio of the $^7F_6$ ground state for increasing admixture of the $^7F_5$ state to the $^7F_6$ ground state.
d: Amount of excited atoms in the $^7F_5$ state over pump-probe delay. After 0.4 ps (21 ± 2) % of all probed atoms are excited.

Table 4.4: Admixture of states for a 4f temperature of (1920 ± 110) K.

T	$^7F_6$	$^7F_5$	$^7F_4$	$^7F_3$	$^7F_2$	$^7F_1$	$^7F_0$	$\sum {}^7F_{J<6}$
1810	82.0 %	11.5 %	4.1 %	1.4 %	0.6 %	0.2 %	0.1 %	18.0 %
1920	80.1 %	12.5 %	4.7 %	1.7 %	0.7 %	0.3 %	0.1 %	19.9 %
2030	78.1 %	13.3 %	5.2 %	1.9 %	0.9 %	0.4 %	0.1 %	21.9 %

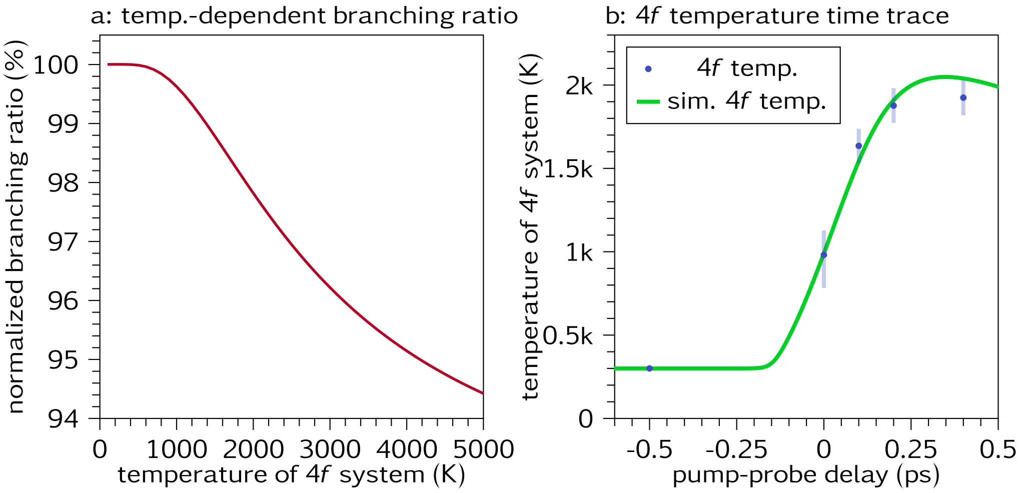

Figure 4.22: a: Normalized branching ratio for a Boltzmann-distributed occupation of ^7F_J multiplets over temperature. The branching ratio is normalized to the branching ratio at 300 K.
b: 4*f* temperature time trace (blue dots) extracted from the experimental $M_{5,4}$ absorption branching ratio. The 4*f* system reaches a temperature of about (1920 ± 110) K in the first few hundred femtoseconds after excitation. The green line depicts the 4*f* temperature simulated via a three-temperature model in Chapter 4.4.5 for a total absorbed energy density of 1.6 kJ cm^{-3}.

4.4.5 Comparison to the three-temperature model

The XAS experiment at the FemtoSlicing facility involved 800 nm-pump-laser pulses with a fluence of $(6 \pm 1)\,\mathrm{mJ\,cm^{-2}}$. The total absorbed energy in the terbium layer was calculated using IMD (see Chapter 4.3.2) for a stack of 2 nm Y | (12 ± 1) nm Tb | 40 nm Y | 100 nm Al and an incident angle of 42° with respect to the sample normal.
With the determined total absorbed energy density in the terbium layer $E_{abs,Tb} = (1.0 \pm 0.3)\,\mathrm{kJ\,cm^{-3}}$ and the coupling parameters determined in Chapter 4.3.4 the temperatures of the $5d$ and $4f$ electronic system as well as the lattice temperature can be estimated in a three-temperature model. The $4f$ temperature based on the three-temperature model reaches a maximum of 1386 K at 0.3 ps for a total absorbed energy density of $1.0\,\mathrm{kJ\,cm^{-3}}$. Within the 1σ uncertainty it can reach 1629 K at 0.31 ps for a total absorbed energy density of $1.3\,\mathrm{kJ\,cm^{-3}}$, while an uncertainty of 2σ allows for 2048 K at 0.35 ps for a total absorbed energy density of $1.6\,\mathrm{kJ\,cm^{-3}}$. Thus, the maximum of the $4f$ temperature of $(1920 \pm 110)\,\mathrm{K}$ evaluated via the $M_{5,4}$ absorption branching ratio is in the 2σ uncertainty range for the absorbed fluence. Discrepancy between the temperature reached in the three-temperature model and evaluated via the $M_{5,4}$ absorption branching ratio probably stems from errors in the determination of the fluence as well as from assuming an idealized sample.
Figure 4.23 presents the calculated transient changes of the respective temperatures for the time-resolved XAS experiment.

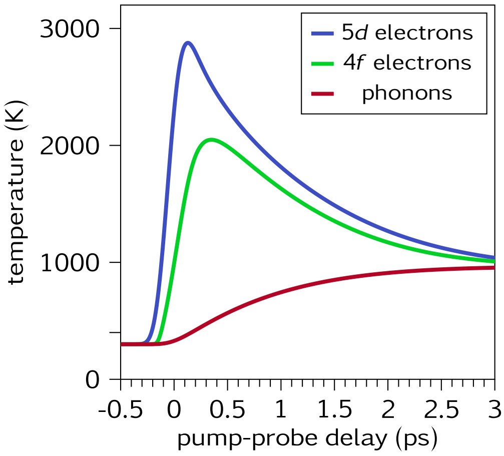

Figure 4.23: Three-temperature model for the XAS experiment at the FemtoSlicing facility. The $4f$ temperature reaches a maximum value of 2048 K at 0.35 ps for a total absorbed energy density of $1.6\,\mathrm{kJ\,cm^{-3}}$.

4.4.6 Summary

The XAS experiment at the FemtoSlicing facility shows that the terbium $M_{5,4}$ absorption branching ratio is reduced after excitation of the sample with 800 nm laser pulses. In view of the 3rd rule of Thole and van der Laan [5] this further proofs the excitation of the 4*f* electronic system out of the ground state multiplet with a change of the total angular momentum J. It was demonstrated that alterations in branching ratio can be analyzed to extract the amount of excited atoms and their relative multiplet occupation, assuming Boltzmann-occupied 4*f* states.

The evaluation revealed that the 4*f* system reaches a temperature of (1920 ± 110) K in the first few hundred femtoseconds, which corresponds to about (20 ± 2) % of all atoms in the probed volume being excited. Similar values can also be simulated by the three-temperature model developed in Chapter 4.3.4.

The evaluation of the branching ratio turns out to be an excellent tool to investigate the dynamics of the 4*f* electronic excitation and temperature in rare-earth metals even for sources with limited energy resolution. Due to the integration over the whole absorption edge, it is not necessary to record the subtle changes in spectral shape but only the overall intensity of the absorption edge.

Chapter 5

Conclusion

This thesis reports on $4f$ electronic excitations, setting in after optical pumping of the rare-earth metal Tb. Via spectral changes, observed in time-resolved M_5 edge XAS and $N_{5,4}$ edge RIXS experiments, such excitations could be identified for the first time and proven to be induced by direct interaction of $5d$ and $4f$ electrons.

The first results presented focus on the time-resolved Tb M_5 edge XAS experiment, performed at the SCS instrument of EuXFEL. By simulating the pump-induced alterations in the XAS spectra with atomistic calculations, the $4f$ multiplet excitation could be attributed to mainly involve $^7F_6 \rightarrow ^7F_5$ transitions. The distinct temporal profile of the $4f$ excitations, following the directly laser-heated $5d$ electrons, revealed inelastic $5d$-$4f$ electron-electron scattering as excitation mechanism. Transferring energy and angular momentum between the $5d$ and $4f$ electronic systems efficiently drives excitations out of the $^7F_6$ ground state.

The Tb $N_{5,4}$ RIXS experiment performed at the PG1 beamline of FLASH at DESY complementarily proved the inelastic $5d$-$4f$ scattering to dominantly provoke transitions into the $^7F_5$ multiplet. As the $4f$ excitations become visible as distinct energy shifts of the inelastic lines in the RIXS spectrum, the method allows to unequivocally identify transient occupation of energetically higher $4f$ multiplets. The time-resolved RIXS spectra gave indications for additional occupation of higher ^7F_J multiplets.

Based on these findings, a three-temperature model including separated temperatures for the $4f$ and the $5d$ valence electrons as well as for the lattice was developed. The coupling parameters, addressing the $5d$-$4f$ interaction and the $4f$-lattice coupling, were adjusted to describe the spectral changes observed at the M_5 edge XAS of Tb metal at EuXFEL. The $5d$-$4f$ coupling parameter was found to be dependent on the amount of $5d$ electrons that can transfer sufficient energy to provoke excitations out of the $^7F_6$ ground state. In view of the minor but residual deviations between experiment and simulated XAS spectra, the possibility of 5d-4f electron transfer excitations was discussed. Their inclusion in the simulation lifted remaining discrepancies but also required a larger number of fit parameters.

Finally, a novel experimental approach was introduced, connecting 4f multiplet excitations and resulting changes of the 4f electronic temperature with pump-induced alterations of the $M_{5,4}$ absorption branching ratio. The performed time-resolved XAS experiment at the FemtoSlicing facility of BESSY II indicated this method to be especially interesting for sources with limited energy resolution, because the fine structure of the absorption signal does not need to be resolved.

The discussed experiments revealed up to 22 % of the probed atoms to be excited into an energetically higher 4f multiplet state, indicating 5d-4f electron-electron scattering to significantly contribute to redistribution of energy and angular momentum on ultrafast timescales. In previous discussions on ultrafast magnetization dynamics in 4f rare-earth metals, this process was disregarded, yet might be playing an important role and contributing to a fundamental understanding of the underlying mechanism. Ultrafast thermalization between the 5d and 4f electronic systems may involve, together with the excitation of energetically higher 4f multiplets, a change in the occupation of the respective sublevels $m_j = -J, \ldots, +J$. This could effectively disalign the atomic angular momentum J and hence contribute to ultrafast demagnetization. In this context the disparate demagnetization timescales observed in Gd and Tb [2] might stem not only from different MCA, but also from the 4f excitations, which are provoked in Tb, but are absent in Gd, after IR-laser pumping.

In this thesis 5d-4f electron-electron scattering is proposed to provide a handle to control MCA on ultrashort timescales. Resonant excitation of these scattering processes might allow to specifically alter the 4f electronic structure and hence for a distinct control over physical properties, such as MCA. This can be of increased interest for magnetic data storage, because a high MCA, as exhibited by the rare-earth metal Tb, stabilizes magnetically stored information against decay and prolongs data storage life time. In turn, strong MCA complicates writing of information. A possible approach to efficiently control magnetization in high MCA systems might be a transient reduction of MCA, lowering the involved energy consumption for magnetic switching.

In order to explore the influence of the inelastic 5d-4f scattering and 4f multiplet excitations on ultrafast magnetization dynamics in rare-earth metals, a new beamline for transmission experiments with improved energy resolution is being setup at the FemtoSlicing facility at BESSY II. Together with the ultrashort circularly polarized X-ray pulses, the beamline will offer the capabilities to study dynamics in the electronic and magnetic system simultaneously in one experiment.

Additionally a specialized experimental chamber for time-resolved RIXS and XAS measurements at the $N_{5,4}$ edges of rare-earth metals will be setup at the free-electron laser facility FLASH at DESY. This chamber will include the possibility to pump and probe with near-IR, THz and XUV pulses while enabling precise control over the magnetic condition of the sample with a 3D-vector magnet. Combining THz pump with XUV probe pulses at the $N_{5,4}$ edge of rare-earth metals will allow studying the influence of resonantly pumped transitions in the $4f$ electronic system on the ultrafast magnetization dynamics.

The upcoming experimental capabilities at FLASH and BESSY II will permit to directly link transient changes in the $4f$ magnetic and electronic structure. This will help to gain a fundamental understanding on the spin and orbital dynamics involved as well as on angular momentum flow between the different microscopic subsystems in $4f$ metals.

Bibliography

[1] J. Barker, U. Atxitia, T. A. Ostler, O. Hovorka, O. Chubykalo-Fesenko, and R. W. Chantrell. Two-magnon bound state causes ultrafast thermally induced magnetisation switching. *Sci Rep*, 3:3262, 2013. `https://doi.org/10.1038/srep03262`.

[2] B. Frietsch, A. Donges, R. Carley, M. Teichmann, J. Bowlan, K. Döbrich, K. Carva, D. Legut, P. M. Oppeneer, U. Nowak, and M. Weinelt. The role of ultrafast magnon generation in the magnetization dynamics of rare-earth metals. *Science Advances*, 6(39):eabb1601, 2020. `https://www.science.org/doi/abs/10.1126/sciadv.abb1601`.

[3] U. Bovensiepen. Coherent and incoherent excitations of the Gd(0001) surface on ultrafast timescales. *Journal of Physics: Condensed Matter*, 19(8):083201, 2007. `https://dx.doi.org/10.1088/0953-8984/19/8/083201`.

[4] K. Bobowski, M. Gleich, N. Pontius, C. Schüßler-Langeheine, C. Trabant, M. Wietstruk, B. Frietsch, and M. Weinelt. Influence of the pump pulse wavelength on the ultrafast demagnetization of Gd(0001) thin films. *Journal of Physics: Condensed Matter*, 29(23):234003, 2017. `https://dx.doi.org/10.1088/1361-648X/aa6c92`.

[5] B. T. Thole and G. van der Laan. Branching ratio in x-ray absorption spectroscopy. *Phys. Rev. B*, 38:3158–3171, 1988. `https://link.aps.org/doi/10.1103/PhysRevB.38.3158`.

[6] C. D. Stanciu, F. Hansteen, A. V. Kimel, A. Kirilyuk, A. Tsukamoto, A. Itoh, and Th. Rasing. All-Optical Magnetic Recording with Circularly Polarized Light. *Phys. Rev. Lett.*, 99:047601, 2007. `https://link.aps.org/doi/10.1103/PhysRevLett.99.047601`.

[7] J. Stöhr and H. C. Siegmann. *Magnetism: From Fundamentals to Nanoscale Dynamics*. Springer Berlin, Heidelberg, 2006. `https://doi.org/10.1007/978-3-540-30283-4`.

[8] B. Harmon. The electronic structure of rare-earths. Band structures of rare earth metals. *Journal de Physique Colloques*, 40(C5):C5–65–C5–70, 1979. `https://hal.science/jpa-00218943`.

[9] S. Abdelouahed and M. Alouani. Magnetic anisotropy in Gd, GdN, and $GdFe_2$ tuned by the energy of gadolinium $4f$ states. *Phys. Rev. B*, 79:054406, 2009. `https://link.aps.org/doi/10.1103/PhysRevB.79.054406`.

[10] J. J. Rhyne and A. E. Clark. Magnetic Anisotropy of Terbium and Dysprosium. *Journal of Applied Physics*, 38(3):1379–1380, 1967. `https://doi.org/10.1063/1.1709631`.

[11] A. Melnikov, H. Prima-Garcia, M. Lisowski, T. Gießel, R. Weber, R. Schmidt, C. Gahl, N. M. Bulgakova, U. Bovensiepen, and M. Weinelt. Nonequilibrium Magnetization Dynamics of Gadolinium Studied by Magnetic Linear Dichroism in Time-Resolved $4f$ Core-Level Photoemission. *Phys. Rev. Lett.*, 100:107202, 2008. `https://link.aps.org/doi/10.1103/PhysRevLett.100.107202`.

[12] A. Kirilyuk, A. V. Kimel, and Th. Rasing. Ultrafast optical manipulation of magnetic order. *Rev. Mod. Phys.*, 82:2731–2784, 2010. `https://link.aps.org/doi/10.1103/RevModPhys.82.2731`.

[13] I. Radu, K. Vahaplar, C. Stamm, T. Kachel, N. Pontius, H. A. Dürr, T. A. Ostler, J. Barker, R. F. L. Evans, R. W. Chantrell, A. Tsukamoto, A. Itoh, A. Kirilyuk, Th. Rasing, and A. V. Kimel. Transient ferromagnetic-like state mediating ultrafast reversal of antiferromagnetically coupled spins. *Nature*, 472:205–208, 2011. `https://doi.org/10.1038/nature09901`.

[14] C. E. Graves, A. H. Reid, T. Wang, B. Wu, S. de Jong, K. Vahaplar, I. Radu, D. P. Bernstein, M. Messerschmidt, L. Müller, R. Coffee, M. Bionta, S. W. Epp, R. Hartmann, N. Kimmel, G. Hauser, A. Hartmann, P. Holl, H. Gorke, J. H. Mentink, A. Tsukamoto, A. Fognini, J. J. Turner, W. F. Schlotter, D. Rolles, H. Soltau, L. Strüder, Y. Acremann, A. V. Kimel, A. Kirilyuk, Th. Rasing, J. Stöhr, A. O. Scherz, and H. A. Dürr. Nanoscale spin reversal by non-local angular momentum transfer following ultrafast laser excitation in ferrimagnetic GdFeCo. *Nature Mater*, 12:293–298, 2013. `https://doi.org/10.1038/nmat3597`.

[15] N. Bergeard, V. López-Flores, V. Halté, M. Hehn, C. Stamm, N. Pontius, E. Beaurepaire, and C. Boeglin. Ultrafast angular momentum transfer

in multisublattice ferrimagnets. *Nat Commun*, 5:3466, 2014. `https://doi.org/10.1038/ncomms4466`.

[16] M. Hennecke, I. Radu, R. Abrudan, T. Kachel, K. Holldack, R. Mitzner, A. Tsukamoto, and S. Eisebitt. Angular Momentum Flow During Ultrafast Demagnetization of a Ferrimagnet. *Phys. Rev. Lett.*, 122:157202, 2019. `https://link.aps.org/doi/10.1103/PhysRevLett.122.157202`.

[17] M. Beens, M. L. M. Lalieu, A. J. M. Deenen, R. A. Duine, and B. Koopmans. Comparing all-optical switching in synthetic-ferrimagnetic multilayers and alloys. *Phys. Rev. B*, 100:220409, 2019. `https://link.aps.org/doi/10.1103/PhysRevB.100.220409`.

[18] J. Hintermayr and B. Koopmans. Explaining all-optical switching in ferrimagnets with heavy rare-earth elements by varying the spin-flip scattering probability of Gd in Co_xGd_{100-x} alloys and Co/Gd bilayers. *Journal of Magnetism and Magnetic Materials*, 603:172260, 2024. `https://www.sciencedirect.com/science/article/pii/S0304885324005511`.

[19] T. Tschentscher, C. Bressler, J. Grünert, A. Madsen, A. P. Mancuso, M. Meyer, A. Scherz, H. Sinn, and U. Zastrau. Photon Beam Transport and Scientific Instruments at the European XFEL. *Applied Sciences*, 7(6), 2017. `https://www.mdpi.com/2076-3417/7/6/592`.

[20] S. Dziarzhytski, M. Biednov, B. Dicke, A. Wang, P. S. Miedema, R. Y. Engel, J. O. Schunck, H. Redlin, H. Weigelt, F. Siewert, C. Behrens, M. Sinha, A. Schulte, B. Grimm-Lebsanft, S. G. Chiuzbăian, W. Wurth, M. Beye, M. Rübhausen, and G. Brenner. The TRIXS end-station for femtosecond time-resolved resonant inelastic x-ray scattering experiments at the soft x-ray free-electron laser FLASH. *Structural Dynamics*, 7(5):054301, 2020. `https://doi.org/10.1063/4.0000029`.

[21] S. Khan, K. Holldack, T. Kachel, R. Mitzner, and T. Quast. Femtosecond Undulator Radiation from Sliced Electron Bunches. *Phys. Rev. Lett.*, 97:074801, 2006. `https://link.aps.org/doi/10.1103/PhysRevLett.97.074801`.

[22] K. Holldack, J. Bahrdt, A. Balzer, U. Bovensiepen, M. Brzhezinskaya, A. Erko, A. Eschenlohr, R. Follath, A. Firsov, W. Frentrup, L. Le Guyader, T. Kachel, P. Kuske, R. Mitzner, R. Müller, N. Pontius, T. Quast, I. Radu, J.-S. Schmidt, C. Schüßler-Langeheine, M. Sperling, C. Stamm, C. Trabant, and A. Föhlisch. FemtoSpeX: a versatile optical pump–soft

X-ray probe facility with 100 fs X-ray pulses of variable polarization. *Journal of Synchrotron Radiation*, 21(5):1090–1104, 2014. `https://doi.org/10.1107/S1600577514012247`.

[23] N. Pontius, K. Holldack, C. Schüßler-Langeheine, T. Kachel, and R. Mitzner. Helmholtz-Zentrum Berlin für Materialien und Energie. The FemtoSpeX facility at BESSY II. *Journal of large-scale research facilities*, 2(A46), 2016. `https://doi.org/10.17815/jlsrf-2-71`.

[24] Helmholtz Zentrum Berlin. FEMTOSPEX-DynaMax, (access on 29.07.2024). `https://www.helmholtz-berlin.de/pubbin/igama_output?modus=einzel&sprache=de&gid=2229&typoid=`.

[25] J. Stöhr. *NEXAFS Spectroscopy*. Springer Berlin, Heidelberg, 1992. `https://doi.org/10.1007/978-3-662-02853-7`.

[26] V. A. Streltsov, C. T. Chantler, R. Ekanayake, and H. Melia. *X-ray absorption*. Laboratory and Computational Physics 3, The university of Melbourne, 2017. `https://www.ph.unimelb.edu.au/~part3/ONLINE/LABNOTES/XAS_grav.pdf`.

[27] J. Evans. *X-Ray Absorption Spectroscopy for the Chemical and Materials Sciences*. John Wiley & Sons Ltd, 2018. `https://doi.org/10.1002/9781118676165`.

[28] A. Kotani and S. Shin. Resonant inelastic x-ray scattering spectra for electrons in solids. *Rev. Mod. Phys.*, 73:203–246, 2001. `https://link.aps.org/doi/10.1103/RevModPhys.73.203`.

[29] L. J. P. Ament, M. van Veenendaal, T. P. Devereaux, J. P. Hill, and J. van den Brink. Resonant inelastic x-ray scattering studies of elementary excitations. *Rev. Mod. Phys.*, 83:705–767, 2011. `https://link.aps.org/doi/10.1103/RevModPhys.83.705`.

[30] M. Beye, Ph. Wernet, C. Schüßler-Langeheine, and A. Föhlisch. Time resolved resonant inelastic X-ray scattering: A supreme tool to understand dynamics in solids and molecules. *Journal of Electron Spectroscopy and Related Phenomena*, 188:172–182, 2013. `https://www.sciencedirect.com/science/article/pii/S0368204813000789`.

[31] P. Bruno. *Physical Origins and Theoretical Models of Magnetic Anisotropy*. 1993. `https://www.researchgate.net/publication/258011866_Physical_Origins_and_Theoretical_Models_of_Magnetic_Anisotropy`.

[32] E. Beaurepaire, J.-C. Merle, A. Daunois, and J.-Y. Bigot. Ultrafast Spin Dynamics in Ferromagnetic Nickel. *Phys. Rev. Lett.*, 76:4250–4253, 1996. `https://link.aps.org/doi/10.1103/PhysRevLett.76.4250`.

[33] A. El-Ghazaly, J. Gorchon, R. B. Wilson, A. Pattabi, and J. Bokor. Progress towards ultrafast spintronics applications. *Journal of Magnetism and Magnetic Materials*, 502:166478, 2020. `https://www.sciencedirect.com/science/article/pii/S0304885319326721`.

[34] R. J. Elliott. Theory of the Effect of Spin-Orbit Coupling on Magnetic Resonance in Some Semiconductors. *Phys. Rev.*, 96:266–279, 1954. `https://link.aps.org/doi/10.1103/PhysRev.96.266`.

[35] Y. Yafet. *g Factors and Spin-Lattice Relaxation of Conduction Electrons*, volume 14 of *Solid State Physics*. Academic Press, 1963. `https://www.sciencedirect.com/science/article/pii/S0081194708602593`.

[36] A. Kiss, L. Szolnoki, and F. Simon. The Elliott-Yafet theory of spin relaxation generalized for large spin-orbit coupling. *Sci Rep*, 6:22706, 2016. `https://doi.org/10.1038/srep22706`.

[37] M. Battiato, K. Carva, and P. M. Oppeneer. Superdiffusive Spin Transport as a Mechanism of Ultrafast Demagnetization. *Phys. Rev. Lett.*, 105:027203, 2010. `https://link.aps.org/doi/10.1103/PhysRevLett.105.027203`.

[38] S. Mathias, C. La-O-Vorakiat, P. Grychtol, P. Granitzka, E. Turgut, J. M. Shaw, R. Adam, H. T. Nembach, M. E. Siemens, S. Eich, C. M. Schneider, T. J. Silva, M. Aeschlimann, M. M. Murnane, and H. C. Kapteyn. Probing the timescale of the exchange interaction in a ferromagnetic alloy. *Proceedings of the National Academy of Sciences*, 109(13):4792–4797, 2012. `https://www.pnas.org/doi/abs/10.1073/pnas.1201371109`.

[39] A. Eschenlohr, M. Battiato, P. Maldonado, N. Pontius, T. Kachel, K. Holldack, R. Mitzner, A. Föhlisch, P. M. Oppeneer, and C. Stamm. Ultrafast spin transport as key to femtosecond demagnetization. *Nature Mater.*, 12:332–336, 2013. `https://doi.org/10.1038/nmat3546`.

[40] L. Cheng, Z. Li, D. Zhao, and E. E. M. Chia. Studying spin-charge conversion using terahertz pulses. *APL Materials*, 9(7):070902, 2021. `https://doi.org/10.1063/5.0051217`.

[41] G. Bierhance, A. Markou, O. Gueckstock, R. Rouzegar, Y. Behovits, A. L. Chekhov, M. Wolf, T. S. Seifert, C. Felser, and T. Kampfrath. Spin-voltage-driven efficient terahertz spin currents from the magnetic Weyl semimetals Co_2MnGa and Co_2MnAl. *Applied Physics Letters*, 120(8):082401, 2022. `https://doi.org/10.1063/5.0080308`.

[42] R. Rouzegar, L. Brandt, L. Nádvorník, D. A. Reiss, A. L. Chekhov, O. Gueckstock, C. In, M. Wolf, T. S. Seifert, P. W. Brouwer, G. Woltersdorf, and T. Kampfrath. Laser-induced terahertz spin transport in magnetic nanostructures arises from the same force as ultrafast demagnetization. *Phys. Rev. B*, 106:144427, 2022. `https://link.aps.org/doi/10.1103/PhysRevB.106.144427`.

[43] R. Gupta, F. Cosco, R. S. Malik, X. Chen, S. Saha, A. Ghosh, T. Pohlmann, J. R. L. Mardegan, S. Francoual, R. Stefanuik, J. Söderström, B. Sanyal, O. Karis, P. Svedlindh, P. M. Oppeneer, and R. Knut. Element-resolved evidence of superdiffusive spin current arising from ultrafast demagnetization process. *Phys. Rev. B*, 108:064427, 2023. `https://link.aps.org/doi/10.1103/PhysRevB.108.064427`.

[44] D. L. Huber. Spin-Magnon Relaxation in Rare-Earth Iron Garnets. *Phys. Rev.*, 136:A500–A507, 1964. `https://link.aps.org/doi/10.1103/PhysRev.136.A500`.

[45] S. Eich, M. Plötzing, M. Rollinger, S. Emmerich, R. Adam, C. Chen, H. C. Kapteyn, M. M. Murnane, L. Plucinski, D. Steil, B. Stadtmüller, M. Cinchetti, M. Aeschlimann, C. M. Schneider, and S. Mathias. Band structure evolution during the ultrafast ferromagnetic-paramagnetic phase transition in cobalt. *Science Advances*, 3(3):e1602094, 2017. `https://www.science.org/doi/abs/10.1126/sciadv.1602094`.

[46] T. S. Seifert, S. Jaiswal, J. Barker, S. T. Weber, I. Razdolski, J. Cramer, O. Gueckstock, S. F. Maehrlein, L. Nadvornik, S. Watanabe, C. Ciccarelli, A. Melnikov, G. Jakob, M. Münzenberg, S. T. B. Goennenwein, G. Wolterdorf, B. Rethfeld, P. W. Brouwer, M. Wolf, M. Kläui, and T. Kampfrath. Femtosecond formation dynamics of the spin Seebeck effect revealed by terahertz spectroscopy. *Nat. Commun.*, 9:2899, 2018. `https://doi.org/10.1038/s41467-018-05135-2`.

[47] P. Jiménez-Cavero, O. Gueckstock, L. Nádvorník, I. Lucas, T. S. Seifert, M. Wolf, R. Rouzegar, P. W. Brouwer, S. Becker, G. Jakob, M. Kläui, C. Guo, C. Wan, X. Han, Z. Jin, H. Zhao, D. Wu, L. Morellón, and T. Kampfrath. Transition of laser-induced terahertz spin currents

from torque- to conduction-electron-mediated transport. *Phys. Rev. B*, 105:184408, 2022. `https://link.aps.org/doi/10.1103/PhysRevB.105.184408`.

[48] S. R. Tauchert, M. Volkov, D. Ehberger, D. Kazenwadel, M. Evers, H. Lange, A. Donges, A. Book, W. Kreuzpaintner, U. Nowak, and P. Baum. Polarized phonons carry angular momentum in ultrafast demagnetization. *Nature*, 602:73–77, 2022. `https://doi.org/10.1038/s41586-021-04306-4`.

[49] H. Hayashi, D. Jo, D. Go, T. Gao, S. Haku, Y. Mokrousov, H.-W. Lee, and K. Ando. Observation of long-range orbital transport and giant orbital torque. *Commun Phys*, 6:32, 2023. `https://doi.org/10.1038/s42005-023-01139-7`.

[50] T. S. Seifert, D. Go, H. Hayashi, R. Rouzegar, F. Freimuth, K. Ando, Y. Mokrousov, and T. Kampfrath. Time-domain observation of ballistic orbital-angular-momentum currents with giant relaxation length in tungsten. *Nat. Nanotechnol.*, 18:1132–1138, 2023. `https://doi.org/10.1038/s41565-023-01470-8`.

[51] M. A. Ruderman and C. Kittel. Indirect Exchange Coupling of Nuclear Magnetic Moments by Conduction Electrons. *Phys. Rev.*, 96:99–102, 1954. `https://link.aps.org/doi/10.1103/PhysRev.96.99`.

[52] T. Kasuya. A Theory of Metallic Ferro- and Antiferromagnetism on Zener's Model. *Progress of Theoretical Physics*, 16(1):45–57, 1956. `https://doi.org/10.1143/PTP.16.45`.

[53] K. Yosida. Magnetic Properties of Cu-Mn Alloys. *Phys. Rev.*, 106:893–898, 1957. `https://link.aps.org/doi/10.1103/PhysRev.106.893`.

[54] A. T. Hindmarch and B. J. Hickey. Direct Experimental Evidence for the Ruderman-Kittel-Kasuya-Yosida Interaction in Rare-Earth Metals. *Phys. Rev. Lett.*, 91:116601, 2003. `https://link.aps.org/doi/10.1103/PhysRevLett.91.116601`.

[55] J. Jensen and A. Mackintosh. *Rare Earth Magnetism: Structures and Excitations*. Clarendon Press, 1991. `https://www.fys.ku.dk/~jjensen/REM.htm`.

[56] J. M. D. Coey. *Magnetism and magnetic materials*. Cambridge University Press, 2010. `www.cambridge.org/9780521816144`.

[57] J. Stöhr and H. König. Determination of Spin- and Orbital-Moment Anisotropies in Transition Metals by Angle-Dependent X-Ray Magnetic Circular Dichroism. *Phys. Rev. Lett.*, 75:3748–3751, 1995. `https://link.aps.org/doi/10.1103/PhysRevLett.75.3748`.

[58] B. T. Thole, P. Carra, F. Sette, and G. van der Laan. X-ray circular dichroism as a probe of orbital magnetization. *Phys. Rev. Lett.*, 68:1943–1946, 1992. `https://link.aps.org/doi/10.1103/PhysRevLett.68.1943`.

[59] P. Carra, B. T. Thole, M. Altarelli, and X. Wang. X-ray circular dichroism and local magnetic fields. *Phys. Rev. Lett.*, 70:694–697, 1993. `https://link.aps.org/doi/10.1103/PhysRevLett.70.694`.

[60] C. Boeglin, E. Beaurepaire, V. Halté, V. López-Flores, C. Stamm, N. Pontius, H. A. Dürr, and J.-Y. Bigot. Distinguishing the ultrafast dynamics of spin and orbital moments in solids. *Nature*, 465:458–461, 2010. `https://doi.org/10.1038/nature09070`.

[61] F. Willems, C. von Korff Schmising, C. Strüber, D. Schick, D. W. Engel, J. K. Dewhurst, P. Elliot, S. Sharma, and S. Eisebitt. Optical inter-site spin transfer probed by energy and spin-resolved transient absorption spectroscopy. *Nat Commun*, 11:871, 2020. `https://doi.org/10.1038/s41467-020-14691-5`.

[62] C. Möller, H. Probst, G. S. M. Jansen, M. Schumacher, M. Brede, J. K. Dewhurst, M. Reutzel, D. Steil, S. Sharma, and S. Mathias. Verification of ultrafast spin transfer effects in iron-nickel alloys. *Commun Phys*, 7:74, 2024. `https://doi.org/10.1038/s42005-024-01555-3`.

[63] A. A. Zholents and M. S. Zolotorev. Femtosecond X-Ray Pulses of Synchrotron Radiation. *Phys. Rev. Lett.*, 76:912–915, 1996. `https://link.aps.org/doi/10.1103/PhysRevLett.76.912`.

[64] S. Serkez, G. Geloni, S. Tomin, G. Feng, E. V. Gryzlova, A. N. Grum-Grzhimailo, and M. Meyer. Overview of options for generating high-brightness attosecond x-ray pulses at free-electron lasers and applications at the European XFEL. *Journal of Optics*, 20(2):024005, 2018. `https://dx.doi.org/10.1088/2040-8986/aa9f4f`.

[65] N. Hartmann, G. Hartmann, R. Heider, M. S. Wagner, M. Ilchen, J. Buck, A. O. Lindahl, C. Benko, J. Grünert, J. Krzywinski, J. Liu, A. A. Lutman, A. Marinelli, T. Maxwell, A. A. Miahnahre, S. P. Moeller, M. Planas, J. Robinson, A. K. Kazansky, N. M. Kabachnik, J. Viefhaus,

T. Feurer, R. Kienberger, R. N. Coffee, and W. Helml. Attosecond time-energy structure of X-ray free-electron laser pulses. *Nature Photonics*, 12:215–220, 2018. `https://doi.org/10.1038/s41566-018-0107-6`.

[66] Z. Huang and K.-J. Kim. Review of x-ray free-electron laser theory. *Phys. Rev. ST Accel. Beams*, 10:034801, 2007. `https://link.aps.org/doi/10.1103/PhysRevSTAB.10.034801`.

[67] S. V. Milton, E. Gluskin, N. D. Arnold, C. Benson, W. Berg, S. G. Biedron, M. Borland, Y.-C. Chae, R. J. Dejus, P. K. Den Hartog, B. Deriy, M. Erdmann, Y. I. Eidelman, M. W. Hahne, Z. Huang, K.-J. Kim, J. W. Lewellen, Y. Li, A. H. Lumpkin, O. Makarov, E. R. Moog, A. Nassiri, V. Sajaev, R. Soliday, B. J. Tieman, E. M. Trakhtenberg, G. Travish, I. B. Vasserman, N. A. Vinokurov, X. J. Wang, G. Wiemerslage, and B. X. Yang. Exponential Gain and Saturation of a Self-Amplified Spontaneous Emission Free-Electron Laser. *Science*, 292(5524):2037–2041, 2001. `https://www.science.org/doi/abs/10.1126/science.1059955`.

[68] F. de Groot and A. Kotani. *Core level spectroscopy of solids*. CRC Press, Boca Raton, 2008. `https://doi.org/10.1201/9781420008425`.

[69] F. de Groot. Multiplet effects in X-ray spectroscopy. *Coordination Chemistry Reviews*, 249(1):31–63, 2005. `https://www.sciencedirect.com/science/article/pii/S0010854504000670`.

[70] M. W. Haverkort, M. Zwierzycki, and O. K. Andersen. Multiplet ligand-field theory using Wannier orbitals. *Phys. Rev. B*, 85:165113, 2012. `https://link.aps.org/doi/10.1103/PhysRevB.85.165113`.

[71] M. W. Haverkort, G. Sangiovanni, P. Hansmann, A. Toschi, Y. Lu, and S. Macke. Bands, resonances, edge singularities and excitons in core level spectroscopy investigated within the dynamical mean-field theory. *Europhysics Letters*, 108(5):57004, 2014. `https://dx.doi.org/10.1209/0295-5075/108/57004`.

[72] M. W. Haverkort. Quanty for core level spectroscopy - excitons, resonances and band excitations in time and frequency domain. *Journal of Physics: Conference Series*, 712(1):012001, 2016. `https://dx.doi.org/10.1088/1742-6596/712/1/012001`.

[73] B. T. Thole, R. D. Cowan, G. A. Sawatzky, J. Fink, and J. C. Fuggle. New probe for the ground-state electronic structure of narrow-band

and impurity systems. *Phys. Rev. B*, 31:6856–6858, 1985. `https://link.aps.org/doi/10.1103/PhysRevB.31.6856`.

[74] R. D. Cowan. *The Theory of Atomic Structure and Spectra*. University of California Press, 1981. `https://www.ucpress.edu/books/the-theory-of-atomic-structure-and-spectra/hardcover`.

[75] A. C. Thompson, D. T. Attwood, E. M. Gullikson, M. R. Howells, K.-J. Kim, J. Kirz, J. B. Kortright, A. L. Robinson, J. H. Underwood, I. Lindau, P. Pianetta, H. Winick, G. P. Williams, and J. H. Scofield. *Center for X-Ray Optics and Advanced Light Source: X-ray Data Booklet*. Lawrence Berkley National Laboratory, 2001. `https://xdb.lbl.gov/`.

[76] T. Kachel, F. Eggenstein, and R. Follath. A soft X-ray plane-grating monochromator optimized for elliptical dipole radiation from modern sources. *Journal of Synchrotron Radiation*, 22(5):1301–1305, 2015. `https://doi.org/10.1107/S1600577515010826`.

[77] T. Kachel. Helmholtz-Zentrum Berlin für Materialien und Energie. The PM3 beamline at BESSY II. *Journal of large-scale research facilities*, 2:A48, 2016. `http://dx.doi.org/10.17815/jlsrf-2-73`.

[78] Helmholtz Zentrum Berlin. UE56-1_ZPM – Artist view on X-ray pulse generation by Femtoslicing, (access on 29.07.2024). `https://www.helmholtz-berlin.de/pubbin/igama_output?modus=einzel&sprache=de&gid=1644&typoid=`.

[79] W. T. Carnall, P. R. Fields, and K. Rajnak. Electronic Energy Levels of the Trivalent Lanthanide Aquo Ions. III. Tb3+. *The Journal of Chemical Physics*, 49(10):4447–4449, 1968. `https://doi.org/10.1063/1.1669895`.

[80] M. Seidel, F. Pressacco, O. Akcaalan, T. Binhammer, J. Darvill, N. Ekanayake, M. Frede, U. Grosse-Wortmann, M. Heber, C. M. Heyl, D. Kutnyakhov, C. Li, C. Mohr, J. Müller, O. Puncken, H. Redlin, N. Schirmel, S. Schulz, A. Swiderski, H. Tavakol, H. Tünnermann, C. Vidoli, L. Wenthaus, N. Wind, L. Winkelmann, B. Manschwetus, and I. Hartl. Ultrafast MHz-Rate Burst-Mode Pump-Probe Laser for the FLASH FEL Facility Based on Nonlinear Compression of ps-Level Pulses from an Yb-Amplifier Chain. *Laser & Photonics Reviews*, 16(3):2100268, 2022. `https://doi.org/10.1002/lpor.202100268`.

[81] N. Thielemann-Kühn, T. Amrhein, W. Bronsch, S. Jana, N. Pontius, R. Y. Engel, P. S. Miedema, D. Legut, K. Carva, U. Atxitia, B. E. van Kuiken, M. Teichmann, R. E. Carley, L. Mercadier, A. Yaroslavtsev, G. Mercurio, L. Le Guyader, N. Agarwal, R. Gort, A. Scherz, S. Dziarzhytski, G. Brenner, F. Pressacco, R.-P. Wang, J. O. Schunck, M. Sinha, M. Beye, G. S. Chiuzbăian, P. M. Oppeneer, M. Weinelt, and C. Schüßler-Langeheine. Optical control of 4*f* orbital state in rare-earth metals. *Science Advances*, 10(16):eadk9522, 2024. `https://www.science.org/doi/abs/10.1126/sciadv.adk9522`.

[82] P. S. Peijzel, P. Vermeulen, W. J. M. Schrama, A. Meijerink, M. F. Reid, and G. W. Burdick. High-resolution measurements of the vacuum ultraviolet energy levels of trivalent gadolinium by excited state excitation. *Phys. Rev. B*, 71:125126, 2005. `https://link.aps.org/doi/10.1103/PhysRevB.71.125126`.

[83] S. Adachi. *The Handbook on Optical Constants of Metals*. WORLD SCIENTIFIC, 2012. `https://www.worldscientific.com/doi/abs/10.1142/8479`.

[84] D. L. Windt. IMD - Software for modeling the optical properties of multilayer films. *Computers in Physics*, 12, 1998. `http://www.rxollc.com/windt/papers/1998_CIP_12_360.pdf`.

[85] M. Sánchez del Río and R. J. Dejus. XOP: a multiplatform graphical user interface for synchrotron radiation spectral and optics calculations. In *Materials, Manufacturing, and Measurement for Synchrotron Radiation Mirrors*, volume 3152, pages 148 – 157. International Society for Optics and Photonics, SPIE, 1997. `https://doi.org/10.1117/12.295554`.

[86] M. Sánchez del Río and R. J. Dejus. XOP v2.4: recent developments of the x-ray optics software toolkit. In *Advances in Computational Methods for X-Ray Optics II*, volume 8141, page 814115. International Society for Optics and Photonics, SPIE, 2011. `https://doi.org/10.1117/12.893911`.

[87] M. I. Kaganov, I. M. Lifshitz, and L. V. Tanatarov. Relaxation between Electrons and Crystalline Lattice. *JETP*, 4:173, 1957. `http://www.jetp.ras.ru/cgi-bin/e/index/e/4/2/p173?a=list`.

[88] S. I. Anisimov, B. L. Kapeliovich, and T. L. Perel′man. Electron emission from metal surfaces exposed to ultrashort laser pulses. *JETP*, 39:375–

377, 1974. http://www.jetp.ras.ru/cgi-bin/dn/e_039_02_0375.pdf.

[89] J.K. Chen, D.Y. Tzou, and J.E. Beraun. A semiclassical two-temperature model for ultrafast laser heating. *International Journal of Heat and Mass Transfer*, 49(1):307–316, 2006. https://www.sciencedirect.com/science/article/pii/S001793100500445X.

[90] B. Hüttner. Thermodynamics and transport properties in the transient regime. *Journal of Physics: Condensed Matter*, 11(35):6757, 1999. https://dx.doi.org/10.1088/0953-8984/11/35/313.

[91] R. W. Hill, J. Cosier, D. A. Hukin, P. Wells, and P. C. Lanchester. The specific heat of terbium below 4 K. *Physics Letters A*, 49(2):101–102, 1974. https://www.sciencedirect.com/science/article/pii/0375960174906896.

[92] A. Einstein. Die Plancksche Theorie der Strahlung und die Theorie der spezifischen Wärme. *Annalen der Physik*, 327(1):180–190, 1907. https://onlinelibrary.wiley.com/doi/abs/10.1002/andp.19063270110.

[93] L. D. Jennings, R. M. Stanton, and F. H. Spedding. Heat Capacity of Terbium from 15 to 350°K. *The Journal of Chemical Physics*, 27(4):909–913, 1957. https://doi.org/10.1063/1.1743878.

[94] S. Arajs and R. V. Colvin. Thermal Conductivity and Electrical Resistivity of Terbium Between 5 and 300°K. *Phys. Rev.*, 136:A439–A441, 1964. https://link.aps.org/doi/10.1103/PhysRev.136.A439.

[95] J. K. Lang, Y. Baer, and P. A. Cox. Study of the 4f and valence band density of states in rare-earth metals. II. Experiment and results. *Journal of Physics F: Metal Physics*, 11(1):121, 1981. https://dx.doi.org/10.1088/0305-4608/11/1/015.

[96] U. Atxitia. Private communication, 2024.

[97] Wolfram Alpha LLC. Wolfram|Alpha, (access on 06.05.2024). https://www.wolframalpha.com/input?i=integral+1%2F%28e%5E%28x%2FT%29%2B1%29+times+%281-1%2F%28e%5E%28%28x-G%29%2FT%29%2B1%29%29+dx.

List of Figures

List of Tables

Acknowledgements

Among the many people, who influenced me positively during my research, there are a few I want to mention specifically.

First of all, I want to thank my supervisor Prof. Dr. Martin Weinelt. I vastly appreciate all the support granted to me. Our discussions taught me a lot and guided me through the whole process of researching and writing this thesis.

Next, my thanks go to my second supervisor Prof. Dr. Wolfgang Kuch. He invited me to his group seminar for several talks including very fruitful exchange of ideas.

During the research for this thesis I had the pleasure to work with many kind and incredibly capable colleagues.

Foremost, I want to mention Dr. Nele Thielemann-Kühn. Countless hours invested into joint projects were sweetened by delightful conversation and effective teamwork. I am profoundly thankful for all her support and patience.

I also want to give a special mention to my mentor Dr. Niko Pontius and Dr. Christian Schüßler-Langeheine. Both always had an open ear for my questions and besides many hours spend together at beamtimes, I also enjoyed all the lunch breaks we shared.

For many insightful discussions and all the theory support provided I thank Dr. Ru-Pan Wang.

My thanks extend to all fellow members of the Weinelt workgroup. It is a delight, to be part of such an amazing group of scientist, sharing problems and solutions in science as well as in daily life. Special thanks go to Dr. Dominic Lawrenz, Dr. Wibke Bronsch and Jan Böhnke for showing me around at the start of my work as well as for simply being amazing colleagues and friends.

Also beside work, I had the incredible luck to receive unbound support from my friends. They helped me keep balance, stay mentally sane and push through all obstacles. I thank Alexander Müller, Paul Nottmeyer, Dr. Fabian Lukas, Leonard Laube, Manuel Gräber and Dr. Dorothee Rosenzweig to name just a few of them.

Last but not least I want to wholeheartedly thank my family. I feel happy having you around.

Declaration of authorship

Name: Amrhein
First name: Tim

I declare to the Freie Universität Berlin that I have completed the submitted dissertation independently and without the use of sources and aids other than those indicated. The present thesis is free of plagiarism. I have marked as such all statements that are taken literally or in content from other writings. This dissertation has not been submitted in the same or similar form in any previous doctoral procedure.

I agree to have my thesis examined by a plagiarism examination software.

Date: August 22, 2025

Signature:

Publications related to this thesis and other projects

Parts of this work have been published in:
N. Thielemann-Kühn, **T. Amrhein**, W. Bronsch, S. Jana, N. Pontius, R. Y. Engel, P. S. Miedema, D. Legut, K. Carva, U. Atxitia, B. E. van Kuiken, M. Teichmann, R. E. Carley, L. Mercadier, A. Yaroslavtsev, G. Mercurio, L. Le Guyader, N. Agarwal, R. Gort, A. Scherz, S. Dziarzhytski, G. Brenner, F. Pressacco, R.-P. Wang, J. O. Schunck, M. Sinha, M. Beye, G. S. Chiuzbăian, P. M. Oppeneer, M. Weinelt, and C. Schüßler-Langeheine.
Optical control of $4f$ orbital state in rare-earth metals.
Science Advances, 10(16):eadk9522, 2024.
`https://doi.org/10.1126/sciadv.adk9522`.
Distributed under a Creative Commons Attribution NonCommercial License 4.0 (CC BY-NC). `https://creativecommons.org/licenses/by-nc/4.0/`

T. Amrhein, B. Salantur, R. Püttner, N. Pontius, K. Holldack, R.-P. Wang, C. Schüßler-Langeheine, M. Weinelt, and N. Thielemann-Kühn.
Non-Equilibrium Multiplet Excitations probed by the $M_{5,4}$ Branching Ratio in $3d \rightarrow 4f$ X-ray Absorption Spectroscopy.
submitted, arXiv:2504.19630 [cond-mat.mtrl-sci].

Other projects performed during the dissertation period include:
Set up and commissioning of the DynaMaX sample growth/preparation unit, consisting of a multi-source MBE chamber and a multi-source sputter growth chamber, connected to the PM3 beamline at BESSY II.

Design and acquisition of an experimental end-station for the FL11 beamline at FLASH at DESY in the scope of the BMBF project SPINFLASH. In this chamber THz, IR and soft X-ray radiation can be used for scattering experiments. A fast ramping and rotatable 2D vector magnet enables precise control over the magnetic field induced on the sample.

In the BMBF project 'Magnetic Dynamics with Maximum X-ray sensitivity at BESSY II' (MaDMaXs) a 2D-space- and time-resolving detector for the detection of X-rays was developed and tested in cooperation with Dr. A. Tremsin. This detector is based on the Timepix 3 chip in combination with a multichannelplate. By gating the multichannelplate with 100 ns high voltage pulses, transmission of photons occurs only for a few ns, protecting the Timepix 3 chip from saturation and allowing for single photon detection. This detector is planned to be employed at the new FemtoSlicing-HR beamline at BESSY II.

In collaboration with O. Gueckstock Gd|Pt thin-films were grown and the spin-transport of said samples was characterized by analyzing emitted THz radiation.
O. Gueckstock, T. Amrhein, B. Andres, P. Jiménez-Cavero, C. Gahl, T. S. Seifert, R. Rouzegar, I. Radu, I. Lucas, M. Wietstruk, L. Morellón, M. Weinelt, T. Kampfrath, and N. Thielemann-Kühn.
Magnon-mediated terahertz spin transport in metallic Gd|Pt stacks.
submitted, arXiv:2503.22483 [cond-mat.mes-hall].

The free electron laser FLASH was upgraded with a variable polarization afterburner undulator at FLASH2 in September 2023. This upgrade enables experiments with circularly polarized X-rays at FLASH. In a joined experiment these circularly polarized X-ray were used to perform XMCD measurements at the *L*-edges of Co, Fe and Ni.
S. Marotzke, D. Gupta, R.-P. Wang, M. Pavelka, S. Dziarzhytski, C. von Korff Schmising, S. Jana, N. Thielemann-Kühn, T. Amrhein, M. Weinelt, I. Vaskivskyi, R. Knut, D. Engel, M. Braune, M. Ilchen, S. Savio, T. Otto, K. Tiedtke, V. Scheppe, J. Rönsch.Schulenberg, E. Schneidmiller, C. Schüßler-Langeheine, H. A. Dürr, M. Beye, G. Brenner, and N. Pontius
First experiments with ultrashort, circularly polarized soft X-ray pulses at FLASH2
Struct. Dyn. 12, 034301, 2025. https://doi.org/10.1063/4.0000298
and
M. Pavelka, S. Marotzke, R.-P. Wang, M. Elhanoty, G. Brenner, S. Dziarzhytski, S. Jana, W. D. Engel, C. von Korff Schmissing, D. Gupta, I. Vaskivskyi, T. Amrhein, N. Thielemann-Kühn, M. Weinelt, R. Knut, J. Rönsch-Schulenberg, E. Schneidmiller, C. Schüßler-Langeheine, M. Beye, N. Pontius, O. Grånäs, H. Dürr
Femtosecond charge and spin dynamics in $Co_{50}Pt_{50}$ alloys
Struct. Dyn. 12, 024303, 2025. https://doi.org/10.1063/4.0000297

As follow-up to the presented tr-RIXS measurements on Tb, another beamtime at the TRIXS endstation at FLASH was performed to measure the time-resolved electronic response at the Dy $N_{5,4}$ edge. During this beamtime, a transient antistokes feature was measured upon pumping the sample, that corresponds to an energy gain characteristic for the excitation of the first excited multiplet in Dy. The data evaluation is currently ongoing.

In an experiment at the VERITAS beamline at MAXIV the RIXS cross-section at the Tb M_5 edge from a metallic Tb sample was investigated. In addition to measurements in the paramagnetic phase of Tb, helicity dependent spectra of ferromagnetic Tb were recorded. The magnetic contrast depends strongly on excitation and photon emission energies. The evaluation and simulation of the non-trivial circular dichroism is subject of ongoing atomistic calculations.
The bachelor thesis of N. Landos focuses on this experiment.

Supervised students during the dissertation period:
C. Krohn, Optically induced magnetization dynamics in Gadolinium studied with X-Rays, bachelor thesis, 2022.

N. Landos, Probing $4f$ Ferromagnetic Terbium with Helicity Dependent RIXS, bachelor thesis, May 2025.

B. Salantur, Non-Equilibrium $4f$ Multiplet Excitations probed with Branching Ratio Spectroscopy, master thesis, June 2025.

Appendix A

Additional information

A.1 Hatree-Fock Slater-Condon values

The Hatree-Fock values for Slater-Condon parameters given in Tab. A.1 are before Slater reduction.

A.2 Function for double exponential fit

The temporal evolution of the pump effect for 1236 eV in XAS for terbium was fitted with the following model using the lmfit routine in Python.

```
def doubleDecayConvRec(x, t0, tau1, tau2, A, C, sigma, offs):
  term1 = expConvGauss(x-t0,tau1,A,sigma)
  term2 = expConvGauss(x-t0,tau2,-C,sigma)
  term3 = ABCHConvGauss(x-t0,A,C,sigma)
  return (term1 + term2 + term3 + offs)
```

with

```
def expConvGauss(x,tau,A,sigma):
  term1 = np.exp(-x/tau)*np.exp(sigma**2/(2*tau**2))*
    (special.erf((sigma**2-x*tau)/(np.sqrt(2)*sigma*tau))-1)
  return -A/2*(term1)
```

and

Table A.1: Hatree-Fock Slater-Condon values (all values in eV).

direct $4f$-$4f$ ($f_\mathrm{i}(ff)$) interaction			
	Tb $4f^7$	Tb $4f^8$	Tb $4f^9$
$f_2(ff)$	15.829	14.915	13.892
$f_4(ff)$	9.981	9.360	8.670
$f_6(ff)$	7.195	6.734	6.225
$4f$ spin-orbit coupling	0.237	0.221	0.205

direct $3d$-$4f$ ($f_\mathrm{i}(df)$) interaction			
	Tb $3d^9 4f^8$	Tb $3d^9 4f^9$	Tb $3d^9 4f^{10}$
$f_2(ff)$	16.461	15.586	14.620
$f_4(ff)$	10.390	9.794	9.141
$f_6(ff)$	7.493	7.050	6.567
$4f$ spin-orbit coupling	0.268	0.251	0.234
$3d$ spin-orbit coupling	13.363	13.368	13.372
$f_2(df)$	10.631	10.055	9.468
$f_4(df)$	5.013	4.709	4.406
$g_1(df)$	7.730	7.240	6.755
$g_3(df)$	4.535	4.245	3.959
$g_5(df)$	3.133	2.933	2.735

direct $4d$-$4f$ ($f_\mathrm{i}(df)$) interaction			
	Tb $4d^9 4f^8$	Tb $4d^9 4f^9$	Tb $4d^9 4f^{10}$
$f_2(ff)$	14.098	15.065	15.940
$f_4(ff)$	8.807	9.460	10.055
$f_6(ff)$	6.326	6.808	7.249
$4f$ spin-orbit coupling	0.208	0.249	0.241
$4d$ spin-orbit coupling	2.366	2.386	2.413
$f_2(df)$	16.144	16.838	17.460
$f_4(df)$	10.277	10.765	11.205
$g_1(df)$	19.012	19.842	20.588
$g_3(df)$	11.903	12.474	12.984
$g_5(df)$	8.407	8.825	9.202

```
def ABCHConvGauss(x,A,C,sigma):
   term1 = -A/2*special.erf(x/(np.sqrt(2)*sigma))
   term2 = +C/2*special.erf(x/(np.sqrt(2)*sigma))
   return term1+term2+1-A/2+C/2
```

In this model $t0$ fits the start of the exponential decay. $tau1$ is the time constant of the exponential drop with intensity A. $tau2$ is the recovery time constant with an amplitude C. $sigma$ is a parameter for temporal broadening. It was calculated from the temporal resolution $(0.065/(2 * \sqrt{(2 * \ln(2))})$ and kept constant. $offs$ is a parameter to align the base level of the fit and the data.
All the parameters used in the displayed fit are shown in Tab. A.2.

A.3 Python implementation of the two-temperature model

The two-temperature model presented in this thesis was realized in Python. First a couple of imports and constants are needed:

```
   from numpy import *
   from matplotlib.pyplot import *
   gamma_el=2.25*10**2 #J m^-3 K^-2
   g_ep=2.25*10**17 #J s^-1 m^-3 K^-1
   T_0=300 #K
   kap_0=16 #J s^-1 m^-1 K^-1
   E_abs=3200 *10**6 #J m^-3
   tau = 85*10**-15 #s
   T_E=0.75*174 #K
   C_ph0=2.2*10**6 #J m^-3 K^-1
   alpha=1/(40*10**-9) #m^-1
   d=10*10**-9 #m
```

Table A.2: Fit parameters used for fitting the temporal evolution of the pump effect in terbium XAS at 1236 eV. Bold printed parameters were kept constant.

t_0	(0.17 ± 0.02) ps	A	0.035 ± 0.003	C	0.05 ± 0.02
$tau1$	(0.07 ± 0.03) ps	$tau2$	(3.0 ± 1.6) ps		
sigma	**0.027 602 96 ps**	$offs$	−0.998 ± 0.001		

In this model a sample will be simulated as a list of temperatures. Each temperature corresponds to a different spot in the sample, spaced equidistant according to the z resolution. The temporal evolution of the temperatures is calculated step by step.

```
#sample structure
zSteps=110
stepsize=d/(10) #z resolution
T_5d=[make_Ts(zSteps,300)] #list of list of temperatures, every
    entry is for one combination of space and time
T_ph=[make_Ts(zSteps,300)]
#time structure
timeline=[]
tStepCount= 110001 #time resolution
tStart=-1000 #fs
tStop=10000 #fs
timesteps=linspace(tStart,tStop,num=tStepCount)*10**-15
timestep=(tStop-tStart)/tStepCount*10**-15
#calculation of temperature evolution depending on the previous
    temperature
for n,t in enumerate(timesteps): #loop over time
  delta_T_5d=make_Ts(zSteps,0)
  delta_T_ph=make_Ts(zSteps,0)
  for z, val in enumerate(delta_T_5d): #loop over space
    delta_T_5d[z]=(-g_ep*(T_5d[n][z]-T_ph[n][z])
      +z_part(z,stepsize,T_5d[n],T_ph[n])
      +P_Laser(t,z*stepsize))/(C_5d(T_5d[n][z])) #K/s
    delta_T_ph[z]=g_ep*(T_5d[n][z]-T_ph[n][z])/C_ph(T_ph[n][z])
        #K/s
  T_5d.append([x+i*timestep for (x,i) in
      zip(T_5d[n],delta_T_5d)]) #K
  T_ph.append([x+i*timestep for (x,i) in
      zip(T_ph[n],delta_T_ph)]) #K
  timeline.append(t*10**12) #ps
```

In this implementation some functions are used to describe the different parameters. Those function are given in the following:

```
#laser power
def P_Laser(t,z): #J m^-3 s^-1
  return E_abs*np.exp(-(t**2)/(2*(tau**2)))
    /(np.sqrt(2*np.pi)*tau)*np.exp(-alpha*z)
```

```
#electron heat capacity
def C_5d(T_5d): #J m^-3 K^-1
  return gamma_el*T_5d
#phonon heat capacity
def C_ph(T_ph): #J m^-3 K^-1
  return (C_ph0*(T_E/T_ph)**2)
    *np.exp(T_E/T_ph)/((np.exp(T_E/T_ph)-1)**2)
#function to create a list of temperature values
def make_Ts(n,T):
  give_list=[]
  for i in range(n):
    give_list.append(T)
  return give_list
#heat transport
def z_part(z,stepsize,T_5d,T_ph): #J s^-1 m^-3
  if z==0: #surface layer
    out=2*kap_0*T_5d[0]/T_ph[0]
      *((T_5d[1]-T_5d[0])/(stepsize**2))
  elif z==len(T_5d)-1: #end of sample
    out=2*kap_0*T_5d[z]/T_ph[z]
      *((T_5d[z-1]-T_5d[z])/(stepsize**2))
  else: #in between
    out=kap_0*T_5d[z]/T_ph[z]
      *(T_5d[z+1]-2*T_5d[z]+T_5d[z-1])/(stepsize**2)
      +kap_0*(((T_ph[z]*(T_5d[z+1]-T_5d[z-1])/(2*stepsize))
      -(T_5d[z]*(T_ph[z+1]-T_ph[z-1])/(2*stepsize)))
      /(T_ph[z]**2))*((T_5d[z+1]-T_5d[z-1])/(2*stepsize))
  return out
```

The heat transport (zpart) is implemented following a private communication with U. Atxitia [96].

As in the experiment the terbium layer was measured in transmission, the measured signal is averaged over the whole layer. The corresponding temperature can be obtained when also averaging over the sample thickness in the simulation. To do so, the first 2 nm in the simulated sample are discarded to account for the yttrium capping layer and then the temperatures are averaged for the following 10 nm.

A.4 Calculation of percentage of excited electrons

The amount of $5d$ electrons that can transmit 280 meV to the $4f$ system can be calculated by the integral over the DOS multiplied by the probability of occupation. The probability of occupation is given in this case by a Fermi function $f(E)$ for the occupied states timed by a Fermi function $1-f(E-\Delta E)$ for holes 280 meV below.

$$n(T_{el}) = \int_{-\infty}^{\infty} D f(E, T_{el})(1 - f(E - \Delta E, T_{el}))\,\mathrm{d}E\,,$$

with $\Delta E = 0.28$ eV and the Fermi function

$$f(E,T) = \frac{1}{e^{\frac{E}{k_B T}} + 1}\,.$$

E describes the distance in energy to the Fermi energy E_F. For simplification the DOS D is assumed to be constant over the energy range, because the $5d$ form a broad band around the Fermi edge.
Using WolframAlpha [97] to solve the indefinite integral results in:

$$n(T_{el}) = [D k_B T_{el} \frac{\ln(e^{\frac{E}{k_B T_{el}}} + 1) - \ln(e^{\frac{E}{k_B T_{el}}} + e^{\frac{\Delta E}{k_B T_{el}}})}{e^{\frac{\Delta E}{k_B T_{el}}} - 1}]_{-\infty}^{\infty}$$

$$= D(\frac{k_B T_{el}}{e^{\frac{\Delta E}{k_B T_{el}}} - 1}(\ln(e^{\frac{\infty}{k_B T_{el}}}+1) - \ln(e^{\frac{\infty}{k_B T_{el}}} + e^{\frac{\Delta E}{k_B T_{el}}}) - \ln(e^{\frac{-\infty}{k_B T_{el}}}+1) + \ln(e^{\frac{-\infty}{k_B T_{el}}} + e^{\frac{\Delta E}{k_B T_{el}}}))$$

With the approximations

$$e^{\frac{\infty}{k_B T_{el}}} + 1 = e^{\frac{\infty}{k_B T_{el}}}\,,$$

$$e^{\frac{\infty}{k_B T_{el}}} + e^{\frac{\Delta E}{k_B T_{el}}} = e^{\frac{\infty}{k_B T_{el}}}$$

and

$$e^{\frac{-\infty}{k_B T_{el}}} + 1 = 1\,,$$

this simplifies to:

$$= D(\frac{k_B T_{el}}{e^{\frac{\Delta E}{k_B T_{el}}} - 1}(\ln(e^{\frac{\infty}{k_B T_{el}}}) - \ln(e^{\frac{\infty}{k_B T_{el}}}) - \ln(1) + \ln(e^{\frac{\Delta E}{k_B T_{el}}}))$$

$$= D(\frac{k_B T_{el}}{e^{\frac{\Delta E}{k_B T_{el}}} - 1} \frac{\Delta E}{k_B T_{el}}).$$

This results in the used function to describe the amount of 5*d* electrons, that can distribute an energy ΔE:

$$n(T_{el}) = D \frac{\Delta E}{e^{\frac{\Delta E}{k_B T_{el}}} - 1}.$$

A.5 Python-implemented calculation of 4*f* heat capacity

To calculate the 4*f* heat capacity, a short Python script was written.
First some imports as well as constants for the energy position and the degeneration of all involved 4*f* multiplets are needed.

```
from numpy import *
from matplotlib.pyplot import *
import scipy.constants as const

#Energies of states
e0_new=0.000000001*const.e
e1_new= 0.2800*const.e
e2_new =0.4086*const.e
e3_new =0.5375*const.e
e4_new =0.6202*const.e
e5_new =0.6804*const.e
e6_new =0.7083*const.e
e_exc_new=array([e0_new,e1_new,e2_new,e3_new,e4_new,e5_new,e6_new])
deg=(13,11,9,7,5,3,1)
```

Further some functions are needed.
The function 'Boltzmann' calculates the Boltzmann distribution for a given energy Et at a temperature T.
The function 'dE_Boltzmann' calculates the average total energy stored per atom for a temperature 'tem' by adding up the contribution of each multiplet and normalizing to the amount of occupied states. The contribution of a multiplet corresponds to the product between the energy position of the multiplet, the Boltzmann distribution for the energy position at a temperature 'tem' and the degeneration of the multiplet.

```
#Boltzmann distriution:
def Boltzmann(Et,T):
    return exp(-Et/(const.k*T))

#total energy in 4f system according to occupation at
    temperature tem
def dE_Boltzmann(tem):
    add0E=e_exc_new[0]*Boltzmann(e_exc_new[0],tem)*13
    add1E=e_exc_new[1]*Boltzmann(e_exc_new[1],tem)*11
    add2E=e_exc_new[2]*Boltzmann(e_exc_new[2],tem)*9
    add3E=e_exc_new[3]*Boltzmann(e_exc_new[3],tem)*7
    add4E=e_exc_new[4]*Boltzmann(e_exc_new[4],tem)*5
    add5E=e_exc_new[5]*Boltzmann(e_exc_new[5],tem)*3
    add6E=e_exc_new[6]*Boltzmann(e_exc_new[6],tem)*1

    add0=Boltzmann(e_exc_new[0],tem)*13
    add1=Boltzmann(e_exc_new[1],tem)*11
    add2=Boltzmann(e_exc_new[2],tem)*9
    add3=Boltzmann(e_exc_new[3],tem)*7
    add4=Boltzmann(e_exc_new[4],tem)*5
    add5=Boltzmann(e_exc_new[5],tem)*3
    add6=Boltzmann(e_exc_new[6],tem)*1
    norm_add=add0+add1+add2+add3+add4+add5+add6

    summe_addE=add0E+add1E+add2E+add3E+add4E+add5E+add6E

    return summe_addE/norm_add
```

The 4*f* heat capacity can be calculated as derivative of the total energy in regards to the temperature. In this implementation the 4*f* heat capacity was evaluated from 0 to 10 000 K in 1 K steps.

```
temp=linspace(0,10000,num=10001)
#specific heat
C4f=[]
for i in range(0,len(temp)-1):
    dT=temp[i+1]-temp[i]
    dE=dE_Boltzmann(temp[i+1])-dE_Boltzmann(temp[i])
    C4f.append(dE/dT*3.12*10**28) # 3.12*10**28 atoms/m^3 to
        convert to, J/(K*m^3)
```

A.6 Python implementation of the three-temperature model

The implementation of the three-temperature model was also done in Python and is very similar to the two-temperature model.
Additional constants are needed:

```
#4f-lattice coupling
g_ep4f=1.8*2.25*10**17 #J s^-1 m^-3 K^-1
#4f-5d coupling
g_4f5d_0=1.25*10**19 #J s^-1 m^-3 K^-1
#Boltzmann constant in eV/K
kB=8.617333262*10**-5 #eV K^-1
```

In this model the sample is a list of temperatures like in the two-temperature model and the temporal evolution is calculated stepwise as well. The difference to the two-temperature model is that an additional temperature got introduced and is coupled to the lattice via g_ep4f and to the valence electrons via g_4f5d.

```
zSteps=110
stepsize=d/(10)
T_5d=[make_Ts(zSteps,300)]
T_4f=[make_Ts(zSteps,300)]
T_ph=[make_Ts(zSteps,300)]
timeline=[]
tStepCount= 110001
tStart=-1000 #fs
tStop=10000 #fs
timesteps=linspace(tStart,tStop,num=tStepCount)*10**-15
timestep=(tStop-tStart)/tStepCount*10**-15
for n,t in enumerate(timesteps):
   delta_T_5d=make_Ts(zSteps,0)
   delta_T_4f=make_Ts(zSteps,0)
   delta_T_ph=make_Ts(zSteps,0)
   for z, val in enumerate(delta_T_5d):
      delta_T_5d[z]=(-g_ep*(T_5d[n][z]-T_ph[n][z])
         -(g_4f5d(T_5d[n][z])*(T_5d[n][z]-T_4f[n][z]))
         +z_part(z,stepsize,T_5d[n],T_ph[n])
         +P_Laser(t,z*stepsize))/(C_5d(T_5d[n][z])) #K/s
      delta_T_ph[z]=g_ep*(T_5d[n][z]-T_ph[n][z])/C_ph(T_ph[n][z])
         +g_ep4f*(T_4f[n][z]-T_ph[n][z])/(C_ph(T_ph[n][z])) #K/s
```

```
        delta_T_4f[z]=(g_4f5d(T_5d[n][z])*(T_5d[n][z]-T_4f[n][z])
          -g_ep4f*(T_4f[n][z]-T_ph[n][z]))/(C_4f(T_4f[n][z])) #K/s
    T_5d.append([x+i*timestep for (x,i) in
       zip(T_5d[n],delta_T_5d)]) #K
    T_4f.append([x+i*timestep for (x,i) in
       zip(T_4f[n],delta_T_4f)]) #K
    T_ph.append([x+i*timestep for (x,i) in
       zip(T_ph[n],delta_T_ph)]) #K
    timeline.append(t*10**12) #ps
```

Two additional functions are used in this model:

```
#scaling the 4f-5d coupling with amount of electrons
def g_4f5d(T_5d): #J s^-1 m^-3 K^-1
    return g_4f5d_0*4*0.28/(np.exp(0.28/(kB*T_5d))-1)
#4f heat capacity
def C_4f(T_4f): #J m^-3 K^-1
    return C4f[int(round(T_4f,0))]
```

g_4f5d scales a coupling constant g_4f5d_0 with the amount of electrons, able to distribute at least 280 meV (see Appendix A.4).
C_4f gives out the 4*f* heat capacity for a certain temperature. These values were calculated beforehand (see Appendix A.5).
As in the two-temperature model, the temperatures are average over the sample thickness.

A.7 Function for background fit

The background of the transmission spectra measured at the FemtoSlicing facility was fitted using the lmfit routine in Python and the following model.

```
def backgroundEJ
     (x,s_1,s_2,offX,offY,be_1,lt_1,sc_1,be_2,lt_2,sc_2):
    model=(offY-s_2*(x-offX)**2
        -s_1*(x-offX)-edge_jump(x,be_1,lt_1,sc_1)
        -edge_jump(x,be_2,lt_2,sc_2))
    return model
```

with

```
from PyAstronomy import pyasl
def edge_jump(x,be,lt,sc):
  E=linspace(-30,60,num=7001,endpoint=True)
  edgejump=pyasl.broadGaussFast(E, sc*heaviside(E-be,0), lt,
     edgeHandling=None, maxsig=None)# broadening
  Theo_EJ=[]
  for j in range(0,len(x)):
    Theo_EJ.append(interp(x[j],E,edgejump))
  return Theo_EJ
```

This model fits the background with a polynomial of second order combined with two edge jumps for the M_5 and M_4 edge, respectively. The edge jump is modeled by a Gaußian-broadened heavyside function. offY is the constant part of the polynomial, while s_1 is the amplitude of the linear part and s_2 the amplitude of the quadratic part. offX introduces an offset in energy. be_1 and be_2 are the energy positions of the two edge jumps, while sc_1 and sc_2 are the respective amplitudes. lt_1 and lt_2 define the broadening of the edge jumps. The broadening was kept fixed at lt_1=lt_2=0.2 as well as the edge jump energy positions to be_1=0 and be_2=30. The value of the edge jump energy position was set arbitrarily to the center of the M_5 and M_4 peak. The remaining parameters for the background fits for the different time steps are shown in Tab. A.3.
Only the area outside the absorption edges was considered for these fits.

Table A.3: Fit parameters used for fitting the background of the terbium XAS around the M_5 and M_4 edge for different time steps.

	s_1	s_2	offX	offY	sc_1	sc_2
−0.5 ps	$4 \cdot 10^{-9}$	$1.3 \cdot 10^{-6}$	81	0.036	0.001	0.003
0 ps	$5 \cdot 10^{-5}$	$1.7 \cdot 10^{-6}$	78	0.033	0.001	0.003
0.1 ps	$1.3 \cdot 10^{-5}$	$2.0 \cdot 10^{-6}$	53	0.029	0.001	0.003
0.2 ps	$7 \cdot 10^{-6}$	$2.3 \cdot 10^{-6}$	50	0.033	0.001	0.002
0.4 ps	$5 \cdot 10^{-10}$	$1.4 \cdot 10^{-6}$	70	0.032	0.002	0.002